AN IMPROVED STOCHASTIC HODGKIN-HUXLEY BASED MODEL OF A NODE OF RANVIER FOR COCHLEAR IMPLANT STIMULATION

AN IMPROVED STOCHASTIC HODGKIN-HUXLEY BASED MODEL OF A NODE OF RANVIER FOR COCHLEAR IMPLANT STIMULATION

By

MOHAMED H. NEGM, B.Sc.

A Thesis

Submitted to the School of Graduate Studies

in Partial Fulfilment of the Requirements

for the Degree

Masters of Applied Science

McMaster University

Masters of Applied Science (2008) McMaster University
(School of Biomedical Engineering) Hamilton, Ontario

TITLE: **An Improved Stochastic Hodgkin-Huxley Based Model of a Node of Ranvier for Cochlear Implant Stimulation**

AUTHOR: Mohamed H. Negm, B.Sc. (Cairo University)

SUPERVISOR: Dr. Ian C. Bruce, PhD

NUMBER OF PAGES: x, 98

for The Prophet Muhammad
⟨ peace and blessings be upon him⟩,
and for Habeeba

Abstract

Cochlear implants (CIs) are prosthetic devices used to partially restore hearing for profound and severely deaf individuals. CIs convert sounds into electrical pulses which stimulate the auditory nerve fibers. An accurate model of auditory nerve fibers (ANFs) would help in improving the functionality of CIs. Previous studies have shown that the original Hodgkin-Huxley (1952) model (with kinetics adjusted for mammalian body temperature) may be better at describing nodes of Ranvier in ANFs than models for other mammalian axon types. However, the Hodgkin-Huxley model is still unable to explain a number of phenomena observed in auditory nerve responses to CI stimulation, such as short-term and long-term adaptation, the time-course of relative refractoriness, and stimulus-dependent random fluctuations in membrane threshold. Recent physiological investigations of spiral ganglion cells have shown the presence of a number of ion channel types not considered in the previous modelling studies, including low-threshold potassium (I_{KLT}) channels and hyperpolarization-activated cation (I_h) channels.

In this thesis, inclusion of these ion channel types in a stochastic Hodgkin-Huxley model is investigated. Four versions of the model are formed and compared: that is, the standard Hodgkin-Huxley model, the standard model with I_h only added, the standard model with I_{KLT} only added, and finally, the standard model with both I_h and I_{KLT} added. Two group of responses are explored: i) single-pulse responses and ii) pules-train responses. For the single pulse responses, a charge-balanced biphasic stimulus pulse is used. The effect of varying the pulse-width and the interphase gap is investigated for both leading phase polarities. Results are compared to responses for single monophasic stimulus pulses in some cases. Pulse-train responses are investigated for charge-balanced depolarizing-phase leading biphasic pulses at rates of 200, 800, and 2000 pulse/s.

Results from single-pulse responses show an increase in spike threshold when one or both of these channel types are included. The addition of I_{KLT} increases random threshold fluctuations in the stochastic model, particularly for longer pulse widths. For pulse-train responses, rapid adaptation in spike rate may be resulting from I_{KLT} whereas I_h produces slower "short-term" adaptation. Thus, the simulation results suggest that including I_{KLT} and/or I_h in a Hodgkin-Huxley model improves the accuracy of the model in describing auditory nerve fiber responses during cochlear implant stimulation.

Acknowledgements

First and foremost I thank and praise the Almighty Allah (God) who gave me the ability, intelligence, help and support to finish this work. May Allah let this work be for the benefit of all mankind. Next, I would like to thank Dr. Ian Bruce, my supervisor, for his invaluable advice and support. He has always been helpful and patient, answering all of my many questions thoroughly and informatively. I also thank him for introducing me to his beautiful family. Through his guidance, I feel that I am better prepared and equipped to be a good researcher. Special thanks to the defence committee, Dr. Hubert deBruin and Dr. Deda Gillespie, for their invaluable advice and comments. I thank Drs Paul Manis and Jason Rothman for their advice in choosing parameters values. I also thank Dr. Graeme Clark for kindly allowing me to use his material in the thesis. I would also like to express my thanks to my professors and colleagues at McMaster University and Cairo Univeristy. I thank my parents and family who encourged me to pursue my graduate studies and have tolerated my absence for a long time. Last but not least, I thank my wonderful wife Yumna for putting up with me and supporting me.

Contents

List of Tables

List of Figures

Chapter 1

Introduction

Cochlear implants (CIs) are prosthetic devices used to partially restore hearing for severely and profoundly deaf individuals. CIs convert speech signals into electrical pulses that stimulate auditory nerve fibers (ANFs). In other words, they bypass the auditory peripheral structure (the pinna to the auditory nerve) and attempt to resemble the function of the hair cells in converting mechanical waves into electrical signals. The ANFs in turn encode the signal in the form of spikes (or action potentials) and transfer them to higher auditory processing centers in the brain. The AN is the only path for the signal in its journey from the CIs' stimulating electrodes to the central system, such that the auditory nerve may act as a "bottle-neck" in the signal path. Many details about the physiology underlying the auditory nerve are well-known, however some are still unclear and need more investigation. Stochastic ion channels are the functional units for action potential generation. These ion channels vary in their type and distribution density at the nodes of Ranvier along the axon. Consequently, it has been argued that part of the speech processing takes place in the auditory nerve (AN) as well as in the central auditory system. Thus, to get more insight about how the ANFs encode the signal, a good understanding of the ion-channels' functionality is needed. A computational model of these ion channels will presumably explain many phenomena observed during CI stimulation of the ANFs and help in developing improved cochlear implants.

1.1 Scope of Work

Data extracted from physiological experiments on animals are very important when studying the physiology of different biological systems such as the nervous system. However, these experiments are hard to set up, expensive and need a lot of regulations. Computational simulations utilize these data to implement models that mimic the real system. Although these models are useful in explaining many features of the modelled system, yet they are based sometimes on many assumptions, limited by the available experimental

data and the computational power, and are designed specifically to model a particular phenomenon. For instance, building a complete model for the whole nervous system, or even the auditory system alone, is a massive problem. One way to get around this problem is to divide the single system into discrete compartments and model each independently. The auditory nerve for instance is composed of bundles of nerve fibers; each fiber has a cell body and an axon; the active regions in an axon are the nodes of Ranvier which divides the axon into segments. Thus a model that describes a single node of Ranvier can act as the building block for a whole neuron model. ANFs and their observed physiological properties have been implemented into computational models. Yet, many of these models do not fully explain the physiological and psychophysical properties of the ANFs. This information is important in CIs research and in understanding the mechanism by which sound is conveyed.

The objective of this thesis is to model a whole node of Ranvier of an auditory nerve fiber and inject stimuli similar to those used in cochlear implants. Many models in the literature have been developed to interpret responses of ANFs to CI stimulation. In this study, the standard Hodgkin-Huxley model is modified to incorporate voltage-gated ion channels not included in previous AN models. These channels are believed to have an impact on the response of the membrane to electrical stimulation. Thus, a better understanding of the mechanism by which the AN encodes CI stimulation could be achieved. Simulation results are compared to both the available physiological data and results from previous models in the literature to evaluate the validity and accuracy of the proposed model.

1.2 Contribution of this Work

Adding stochastic voltage-gated ion channels, such as the low-threshold potassium (KLT) and the hyperpolarization-activated cation (HCN) channels, to the classical fast sodium and delayed rectifier potassium in a Hodgkin-Huxley based model for ANFs has not been fully explored in previous models. Recent experimental studies have shown the presence of these channels at different regions across the auditory pathways, such as the ventral cochlear nucleus, the spiral ganglion, and the auditory nerve (Chen, 1997; Rothman and Manis, 2003a; Rodrigues and Oertel, 2006). KLT and HCN each has an effect on the membrane response properties and action potential characteristics.

The single-pulse and the pulse-train responses of the model are evaluated. The model is able to account for the positive correlation between random threshold fluctuations and phase duration of the stimulus pulse when I_{KLT} is included (with or without I_h) which is consistent with data from cat ANFs (Bruce et al., 1999c). It has been shown that these random fluctuations are physiologically and psychophysically significant (Verveen, 1960; Bruce et al., 1999c; Ferguson et al., 2003).

Reduction in spike rate in response to pulse trains over a long period of time is observed during electrical and acoustical stimulation. However, previous models did not fully

explain the source of this phenomenon. The model described in this report has the ability to imitate rapid and short-term adaptation when adding I_{KLT} and I_h, respectively, which is consistent with data recorded from cat ANF stimulation (Zhang et al., 2007; Miller et al., 2008). Therefore this model could more accurately explain many phenomena associated with CI stimulation of the AN.

1.3 Thesis Layout

This thesis is composed of seven chapters (including this chapter). Following this chapter, chapter 2 gives a general background about the anatomy of the ear and physiology of hearing. A brief introduction about nerve physiology and voltage-gated ion channels is provided. The final subsection of the chapter explains in brief types of hearing impairment and the theory of operation of cochlear implants. Chapter 3 is a literature review that summarizes most of the related published literature and highlights problems that the present study is attempting to solve. Full descriptions of the model, equations, and stochastic algorithm used are given in chapter 4. Simulation results are divided between chapters 5 and 6, presenting the model single-pulse and pulse-train responses, respectively. Each of 5 and 6 ends with a discussion section in which the results are related to the published literature. Finally, chapter 7 concludes this study with the summary of findings. Suggested future work is also included.

1.4 Related Publications

The following publications have been conducted by the author during the progress of this thesis, in conjunction with the thesis supervisor, Dr. Ian C. Bruce.

Negm, M. H., and Bruce, I. C. (2008). "Effects of Ih and IKLT on the Response of the Auditory Nerve to Electrical Stimulation in a Stochastic Hodgkin-Huxley Model," in *Proceedings of 30th Annual International Conference of the IEEE EMBS*, IEEE, Vancouver, BC, Canada, pp. 5539-5542.

Negm, M. H., and Bruce, I. C. (2008). "Effects of Ih and IKLT in a stochastic Hodgkin-Huxley auditory nerve model," in *Abstracts of the 31st ARO Midwinter Research Meeting*, Phoenix, AZ.

Negm, M. H., and Bruce, I. C. (2007). "A computational model for stochastic ion channels in the auditory nerve," in *Abstracts of Workshop on Mathematical Neuroscience*, Centre de recherches mathématiques, Université de Montréal, Québec.

A journal paper is being prepared for submission.

Chapter 2

Background

2.1 Overview

Prosthetic devices are used to act as a replacement for malfunctioning organs or parts in the human body. In order to design such devices in a way that closely mimics the complex structures of the body, a deep understanding of the anatomical structures and clinical physiology of these organs is required. Cochlear implants (CIs) or bionic ears are examples of prosthetic devices. A CI is an electronic device implanted inside the cochlea of a severely deaf person to partially restore hearing. A full understanding of the anatomy and physiology of the auditory system is helpful in appreciating how CIs function and to develop improved CIs.

In this chapter, an introduction to the anatomy and physiology of the auditory system is given. The primary emphasis is on the auditory nerve and ion channels. The basic components and theory of operation of CIs are also discussed.

2.2 Anatomy and Physiology of the Auditory System

Perception of sound in mammals is a very complex process. Sound waves picked up by the ear are transferred via several complex and precise stages to the brain for higher processing levels. The organs involved in the sound perception process are known as the *auditory system*. The human auditory system is sensitive to sound frequencies between 20 Hz to 20,000 Hz at various intensity levels (from around 0 to 120 dB SPL).

2.2.1 Anatomy of the Auditory System

The auditory system can be divided into the peripheral and central auditory systems. The peripheral auditory system, Fig. 2.1, is further divided into three regions: (1) the external ear; (2) the middle ear; and (3) the inner ear, including the auditory nerve (AN). The

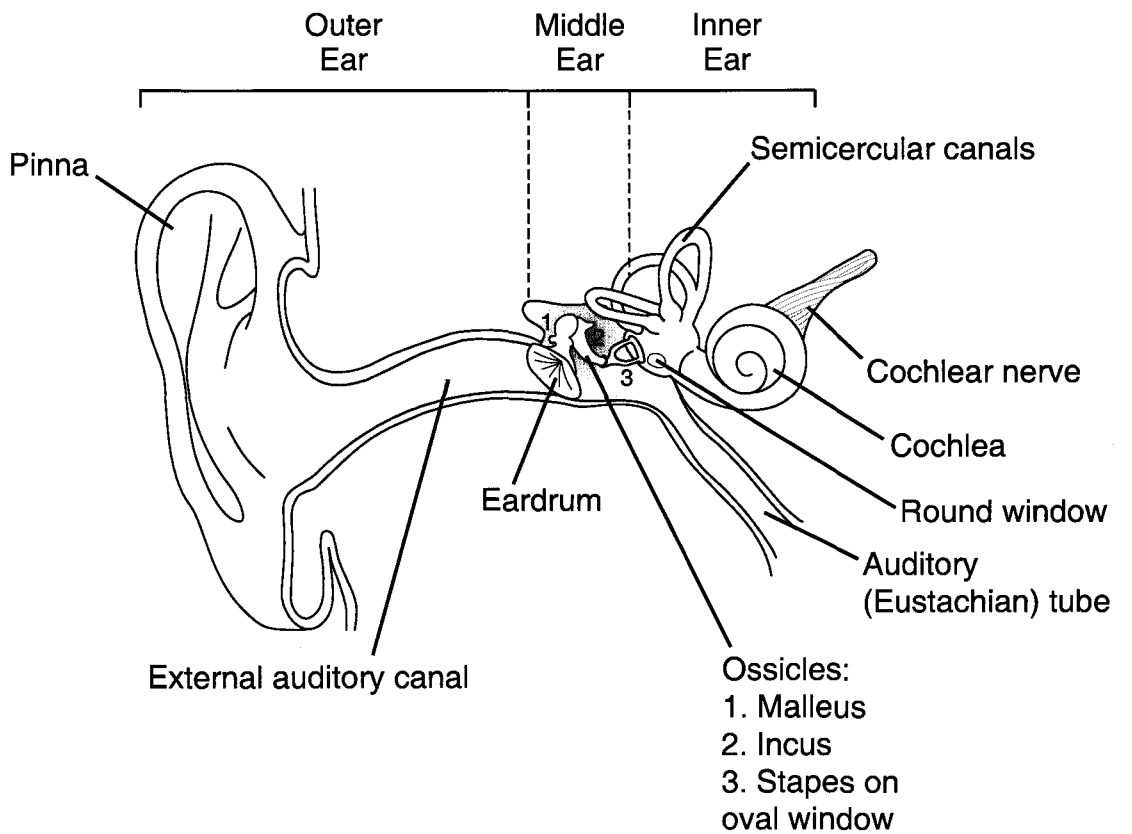

Figure 2.1: The human peripheral auditory system. (Modified from Clark (2003), and reprinted with kind permission from Dr. G. Clark and Springer Science+Business Media.)

central auditory pathways extend from the cochlear nucleus (CN) to the auditory cortex in the brain.

2.2.1.1 The External Ear

The external (outer) ear includes the auricle (*pinna*), external auditory canal, and eardrum (*tympanic membrane*). The pinna directs the sound waves into the *external auditory canal*. The special geometry of the pinna helps in sound localization. The eardrum, a thin semitransparent membrane, separates the external ear from the middle ear.

2.2.1.2 The Middle Ear

The middle ear extends from the tympanic membrane to the *oval* and *round* windows in the cochlea. It is located in an air-filled cavity in the temporal bone. The middle ear is connected to the nasopharynx through the auditory tube (Eustachian tube). The auditory

tube is responsible to keep the pressure inside the middle ear equal to atmospheric pressure. Sound waves are passed from the eardrum to the cochlea by three consecutive bones known as the *auditory ossicles*. They are named the malleus, incus, and stapes and are known to be the smallest bones in the body. The internal surface of the ear drum is attached to the handle of the malleus. The head of the malleus articulates with the incus which in turn articulates with the stapes. The footplate of the stapes rests on the membrane of the oval window in the cochlea.

2.2.1.3 The Inner Ear

The inner ear (*labyrinth*) is a complicated bony structure (bony labyrinth) which encloses the membranous labyrinth. The inner ear can be subdivided into the *semicircular canals*, the *vestibule*, and the *cochlea*. The semicircular canals and the vestibule contain receptors for equilibrium, whereas the cochlea contains receptors for hearing. The area between the bony labyrinth and the membranous labyrinth is filled with perilymph while the membranous labyrinth is filled with endolymph. The endolymph has a higher potassium ion concentration more than any other extracellular fluid. The inner ear is innervated by the vestibulocochlear nerve (cranial nerve VIII), which is divided into two portions, (1) the vestibular nerve, which supplies the semicircular canals and the vestibule; and (2) the cochlear nerve (auditory nerve), which supplies the cochlea.

The cochlea is a snail-shaped bony spiral canal. The central region is called the *modiolus*. The cochlea makes almost three turns around its central region. The cochlea is composed of three channels, i) *scala vestibuli*, which contains perilymph and ends at the oval window; ii) *scala tympani*, which also contains perilymph and ends at the round window; iii) the cochlear duct (*scala media*), which contains endolymph. The scala vestibuli is connected to the scala tympani through a small opening at the apex called the helicotrema. The scala vestibuli is separated from the cochlear duct by the vestibular membrane (or Reissner's membrane), while the basilar membrane separates the scala tympani and the cochlear duct. Fig. 2.2 shows a cross section of one turn of the cochlea.

The *organ of Corti* or the spiral organ lies on the basilar membrane (Fig. 2.3). Embedded in the organ of Corti are the *hair cells*. There are about 16,00 hair cells, which act as hearing receptors, divided into two groups, the inner hair cells (IHCs) and the outer hair cells (OHCs). The IHCs and OHCs synapse with the cochlear (auditory) nerve at their basal end. The OHCs are arranged in three rows and synapse with about 90% of the efferent neurons (motor neurons), whereas the IHC are arranged in one row and synapse with 90-95% of the afferent neurons (first-order sensory neurons) in the cochlear nerve (Tortora and Derrickson, 2003). A hair bundle of stereocilia at the apical end of each hair cell extends into the endolymph of the cochlear duct. Each hair bundle contains about 30-100 stereocilia of graded length. The *tectorial membrane* covers the hair cells and is in contact with tallest stereocilia.

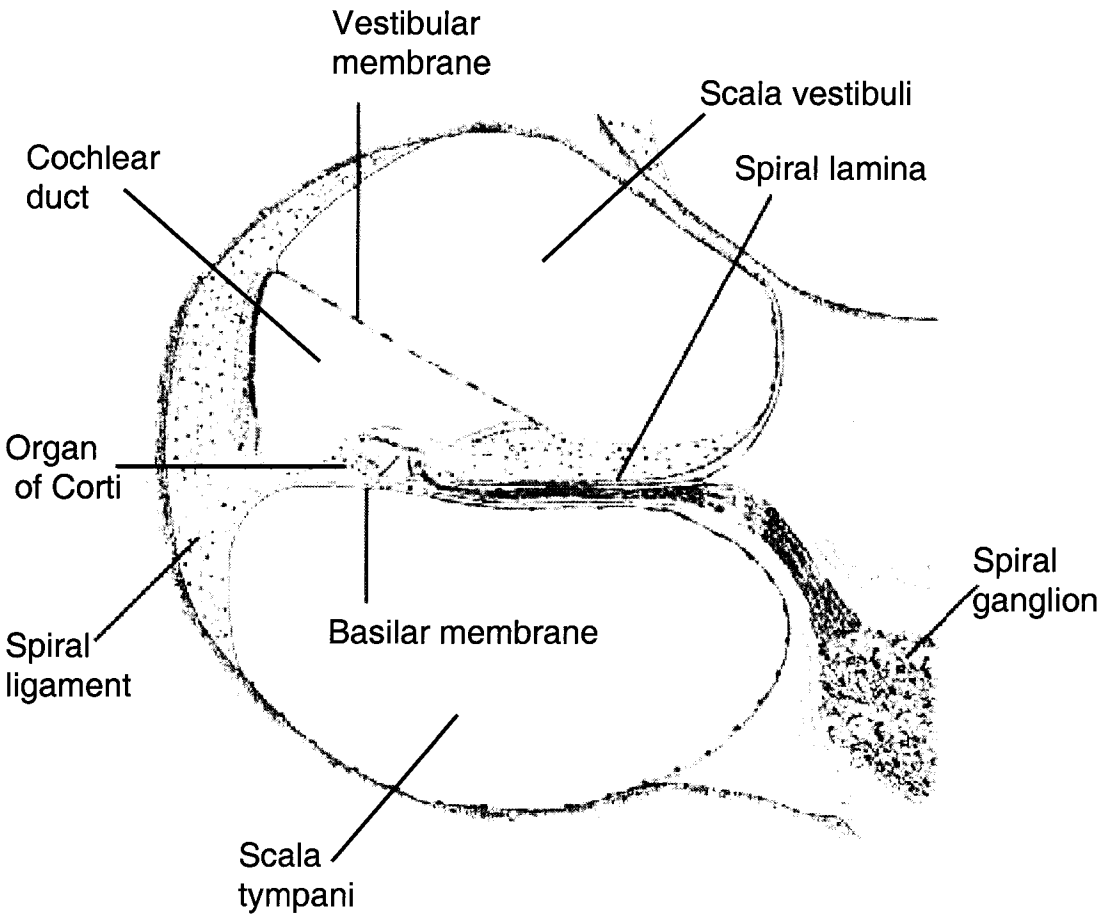

Figure 2.2: A cross section in the human cochlea. The section in through one turn of the cochlea (Modified from Clark (2003), and reprinted with kind permission from Dr. G. Clark and Springer Science+Business Media).

2.2.2 Physiology of the Auditory System

Sound waves enter the ear from the pinna and travel through the external auditory canal until they strike the eardrum, causing the eardrum to vibrate back and forth. The vibration of the eardrum causes the malleus in the middle ear to vibrate. Consequently, the incus and stapes vibrate successively. The vibration is then transmitted to the oval window through the footplate of the stapes. The perilymph of the scala vestibuli moves proportionally to the vibration of the oval window. The auditory ossicles match the impedance difference between the sound air pressure waves in the external ear and fluid pressure waves of the perilymph inside the cochlea by amplifying the vibration velocity at the oval window 20 times more than that at the eardrum.

The vigorous vibration of the oval window displaces the perilymphatic fluid inside the

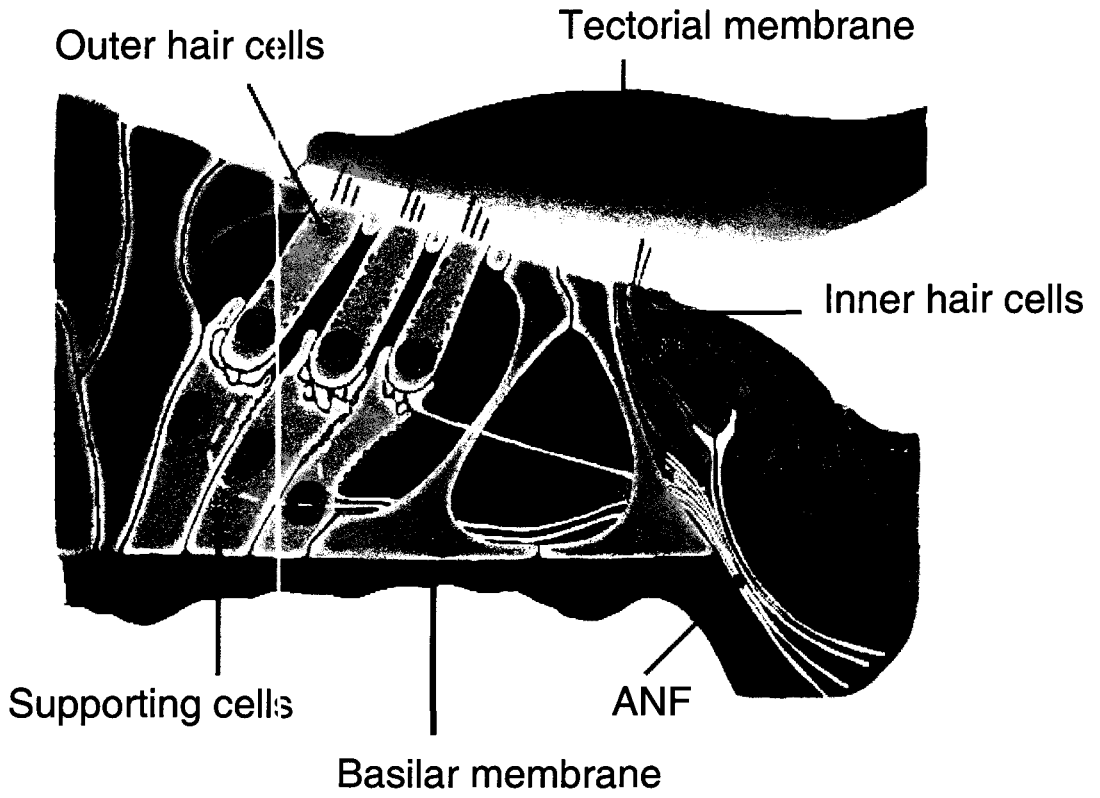

Figure 2.3: An enlargement of the organ of Corti. The section in through one turn of the cochlea. (Modified from Clark (2003), and reprinted with kind permission from Dr. G. Clark and Springer Science+Business Media.)

scala vestibuli towards the scala tympani, through the helicotrema, causing the round window to bulge outwards. Fluid pressure deflects the basilar membrane upwards and downwards. The endolymph displacement in cochlear duct follows that of the perilymph as the vibration is transferred by the basilar membrane. Vibrations in the basilar membrane stimulate hearing receptors at the organ of Corti by moving the hair cells' stereocilia against the tectorial membrane. As the basilar membrane moves upwards or downwards, the hair cells' stereocilia bend. At this point the mechanical vibrations are transformed into electrical signals. The direction of bending of the the stereocilia of the hair cells determines the type of membrane potential response. If it is towards the longest stereocilium, the movement is depolarizing and if it is in the opposite direction, then the movement is hyperpolarizing. Hair cells synapse with auditory nerve fibers at their bases, leading to the generation of impulses in the nerve. Cell bodies of ANFs are located in the spiral ganglion where their axons —about 30,000— form the cochlear nerves. Sound information is then conveyed to the central nervous system.

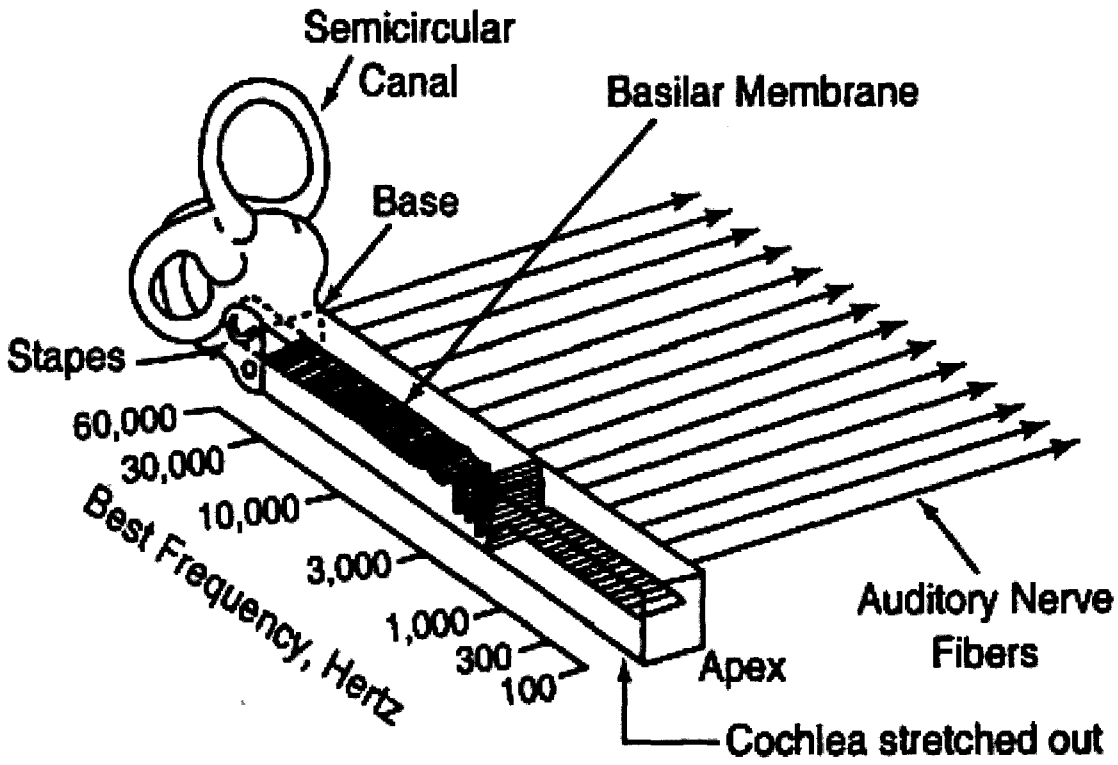

Figure 2.4: A Schematic showing the frequency tuning property in the cochlea. The basilar membrane at the basal end vibrates maximally in response to high frequencies while the apical end is best suited for low frequencies. Between the two extremities ranges of frequencies varies. (Modified from Sachs et al. (2002, fig.1.B,p.158) and reprinted with kind permission from Springer Science+Business Media.)

Sound wave frequency and intensity are encoded in the cochlea. Regions of the basilar membrane along the cochlea do not respond equally to various frequencies. Certain regions resonate more in response to a particular frequency. The basal region of the cochlea is stiffer and vibrates more to higher frequencies, whereas in the apical region the basilar membrane vibrations to low frequencies are maximal. In other words, the tonotopic characteristic of the basilar membrane acts somewhat like a Fourier analyzer or bank of bandpass filters, whereby waves are dissected into their frequency components. This is known as the *place* principle, as shown in Fig. 2.4. Another method used by the cochlea to encode low frequencies —typically below 5 kHz— is the *volley* principle. Therein, volleys of nerve impulses are phase locked at the sound frequency.

Intensity is determined by the magnitude of basilar membrane vibration. Louder sounds have higher intensities that cause the basilar membrane to vibrate intensely. The increase in the vibrations is translated into nerve impulses at higher discharge rates. Sound intensity is coded also by the population of firing nerves.

2.2.2.1 Central Auditory Pathways

The central auditory system transfers sound signals from the cochlear nerve up to the auditory cortex in the brain. It starts at the cochlear nuclei located at the upper part of the medulla. All ANFs of the cochlear nerves from each ear synapse in the cochlear nuclei. Most of the second-order neurons originating from each cochlear nucleus pass to the superior olivary nucleus in the contralateral side. Some of the neurons do not cross to the other side and pass to the superior olivary nucleus in the same side. Most of the fibers from the superior olivary nucleus pass directly to the inferior colliculus, while other fibers synapse first at the lateral lemniscus nucleus then pass to the inferior colliculus. All fibers from the inferior colliculus synapse at the medial geniculate nucleus. Finally, the auditory radiations pass the neural information to the auditory cortex located in the superior gyrus of the temporal lobe. The core nuclei of the auditory pathways maintain the tonotopic representation of frequencies from the cochlea and all the way to the cortex. Each stage in the auditory pathway is responsible for performing a certain function in the sound encoding. Fig. 2.5 demonstrates a simplified schematic of the central auditory pathways.

2.2.3 Auditory Nerve Fibers

Auditory nerve fibers (ANFs) are responsible for carrying auditory information from the cochlea to higher processing levels in the brain (Fig.2.6). ANFs synapse with hair cells inside the cochlea. Cell bodies are located in the spiral ganglia at different regions along the cochlea, where each region resonates to a specific band of frequencies. Axons extend outward from the cell bodies to form the cochlear nerve. The cochlear nerve then combines with the vestibular nerve to form the vestibulocochlear nerve. Axons of ANFs terminate at the cochlear nucleus.

2.2.3.1 The Neuron

The building unit of ANFs, and the nervous system in general, is the neuron. An example of a typical neuron is shown in Fig. 2.7. A neuron is composed of four main parts, (1) dendrites, which act as the input; (2) cell body (soma), which contains the cell nucleus; (3) the axon, which is the longest portion of the neuron; (4) axon terminals at which the axon splits into smaller branches that act as outputs.

Ionic composition and concentration in the extracellular and intracellular fluids maintain the electrical properties of cells. These principal ions are Na^+, K^+, Ca^{2+}, and Cl^-. The cell membrane consists of a lipid bilayer which prevents the movement of water molecules and water soluble substances between the extracellular and intracellular fluids, except for lipid-soluble substances. However, transport of other molecules and ions across the membrane takes place through protein molecules embedded in the membrane known as transport proteins. Two types of protein molecules exist, the channel proteins and the carrier proteins. The former allows the free movement of water and selected ions, while in the

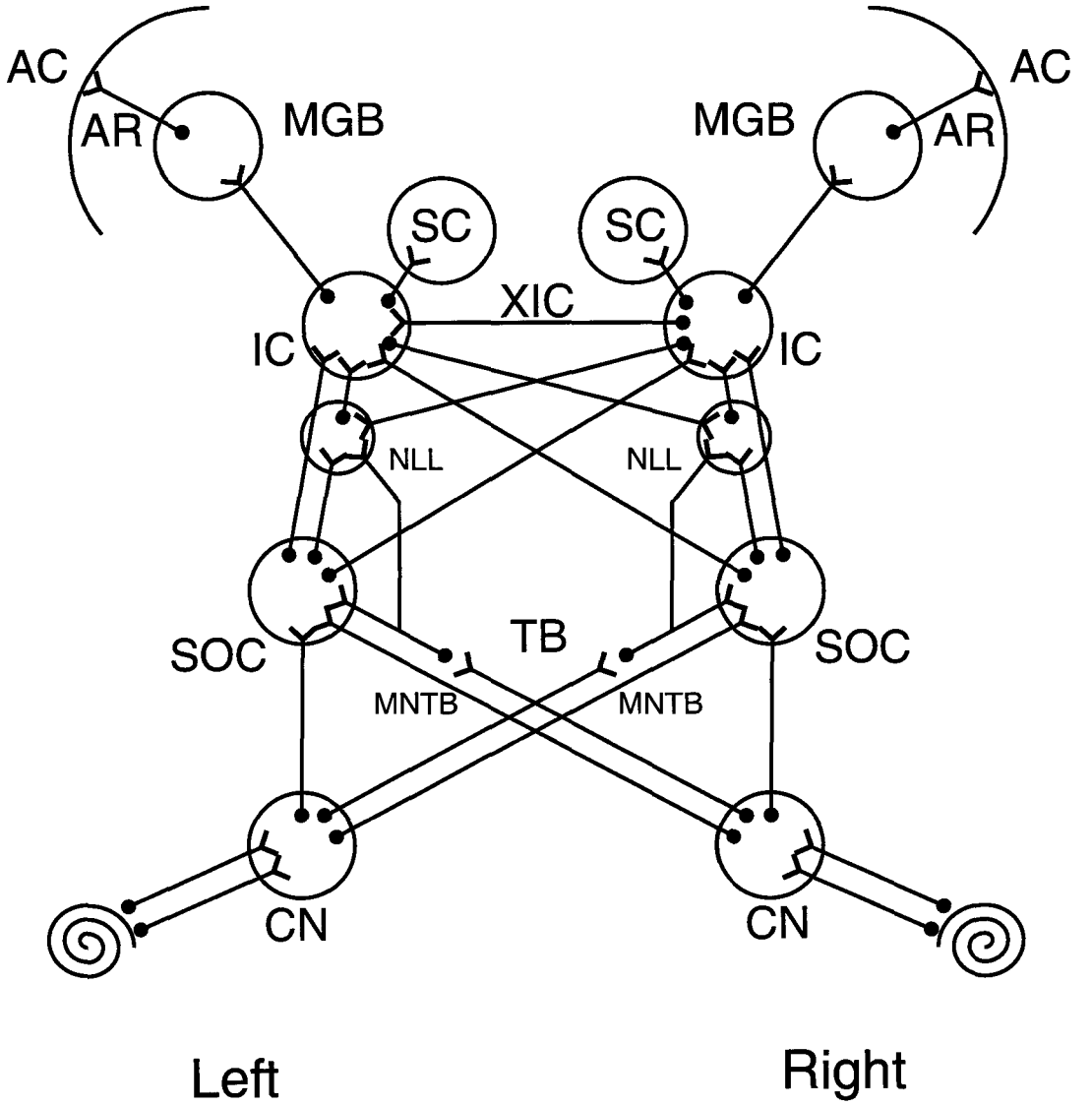

Figure 2.5: Schematic of the central auditory pathways showing major processing centers. Labels are as follows: CN, cochlear nucleus; MNTB, medial nucleus of the trapezoid body; TB, trapezoid body; SOC, superior olivary complex; NLL, nucleus of the lateral lemniscus; IC, inferior colliculus; XIC, the commissure of the inferior colliculus; SC, superior colliculus; MGB, medial geniculate body; AR, auditory radiation; AC, auditory cortex. (Reprinted with kind permission from Clark (2003, fig.2.17,p.85) and Springer Science+Business Media.)

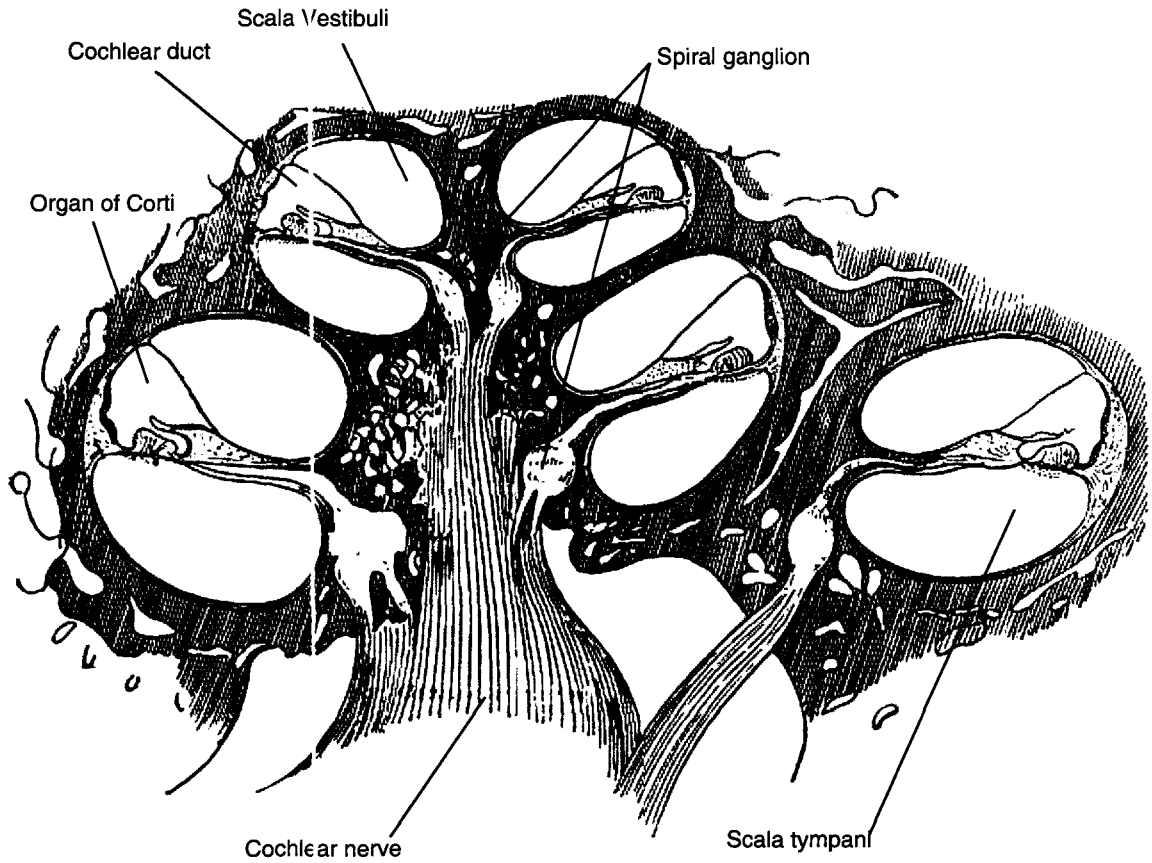

Figure 2.6: A longitudinal section of the cochlea. (Modified and adapted from Gray and NetLibrary (1974).)

latter the ion or molecule binds with the protein, that moves the transported substance to the other side of the membrane. The transport process across the cell membrane occurs in two forms, either passive transport (diffusion) or active transport. Active transport requires energy in order to force ions to move against their concentration gradients, such as the Na^+-K^+ pump. Diffusion on the other hand does not require energy, as ions and water follow their concentration gradients in their movement across the membrane. Diffusion is further divided into two subtypes, simple diffusion and facilitated diffusion. The latter makes use of carrier proteins to facilitate the movement of ions across the membrane but not against their concentration gradient in contrast with active transport.

Simple diffusion is also divided into direct transport of lipid-soluble substances as mentioned earlier, and diffusion through protein channels. These protein channels are characterized by being highly selective to a certain ion-type. The opening and closing of these channels occur when the protein subunits undergo a conformational change. Protein channels are either voltage-gated, where the channel conformational state is dependent on the

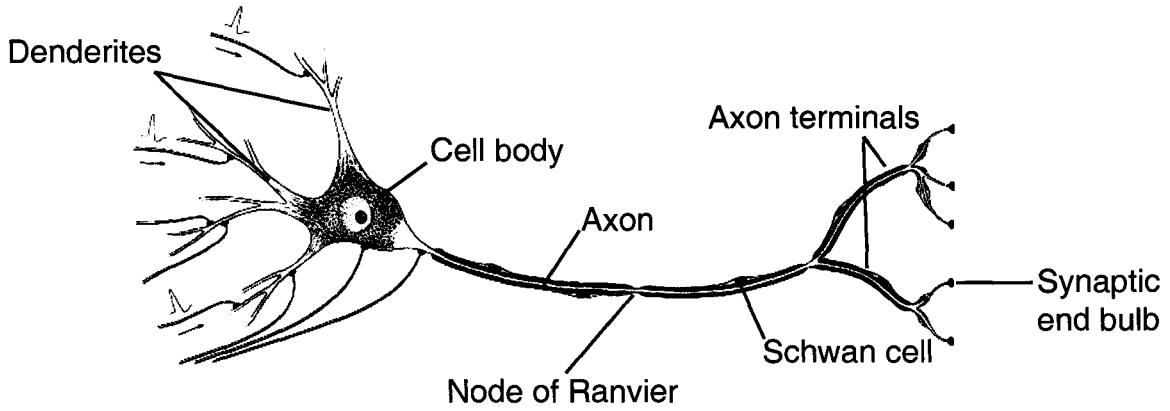

Figure 2.7: A typical neuron. (Modified from Clark (2003), and reprinted with kind permission from Dr. G. Clark and Springer Science+Business Media.)

electrical potential across the membrane, or ligand-gated where the conformational change occurs when a ligand is attached to the channel. Voltage-gated channels are the main interest of this study and will be discussed thoroughly in subsequent chapters.

The cell membrane of neurons is excitable (the same as for muscles), thus they have the ability to generate electrical impulses along their membrane. These electrical signals are known as action potentials (AP). An action potential initiated at the dendrites and/or the soma of the auditory nerve travels all the way along the axon until it reaches the axon terminals.

2.2.3.2 Membrane Potential of Neurons

At equilibrium, the membrane establishes a constant transmembrane potential, $V_m(t)$, at approximately -70 mV called the resting membrane potential, V_{rest}. No action potential is being generated at this point. The Na^+ concentration on the outside of the cell membrane is higher than inside, whereas the K^+ concentration is higher on the inside. Due to these concentration gradients of ions on both sides of the membrane, Na^+ ions diffuse through "leakage" channels from outside to inside and K^+ ions diffuse from the inside to the outside. However, the diffusion of K^+ is much higher than Na^+ which causes the membrane to be more negative inside, giving rise to the negative resting potential. Diffusion of ions into or out of the fiber is opposed by the potential difference built up by the ions accumulated on both sides of the membrane. Furthermore, active transport such as the Na^+-K^+ pump contributes to maintain the resting membrane potential.

Action potentials (Fig. 2.8) are changes in the membrane voltage during which the membrane potential turns positive then negative again in a very short time. The mechanism by which the AP is generated is mainly controlled by voltage-gated ion channels. Upon the arrival of a stimulus, voltage-gated sodium channels are quickly activated, allowing the

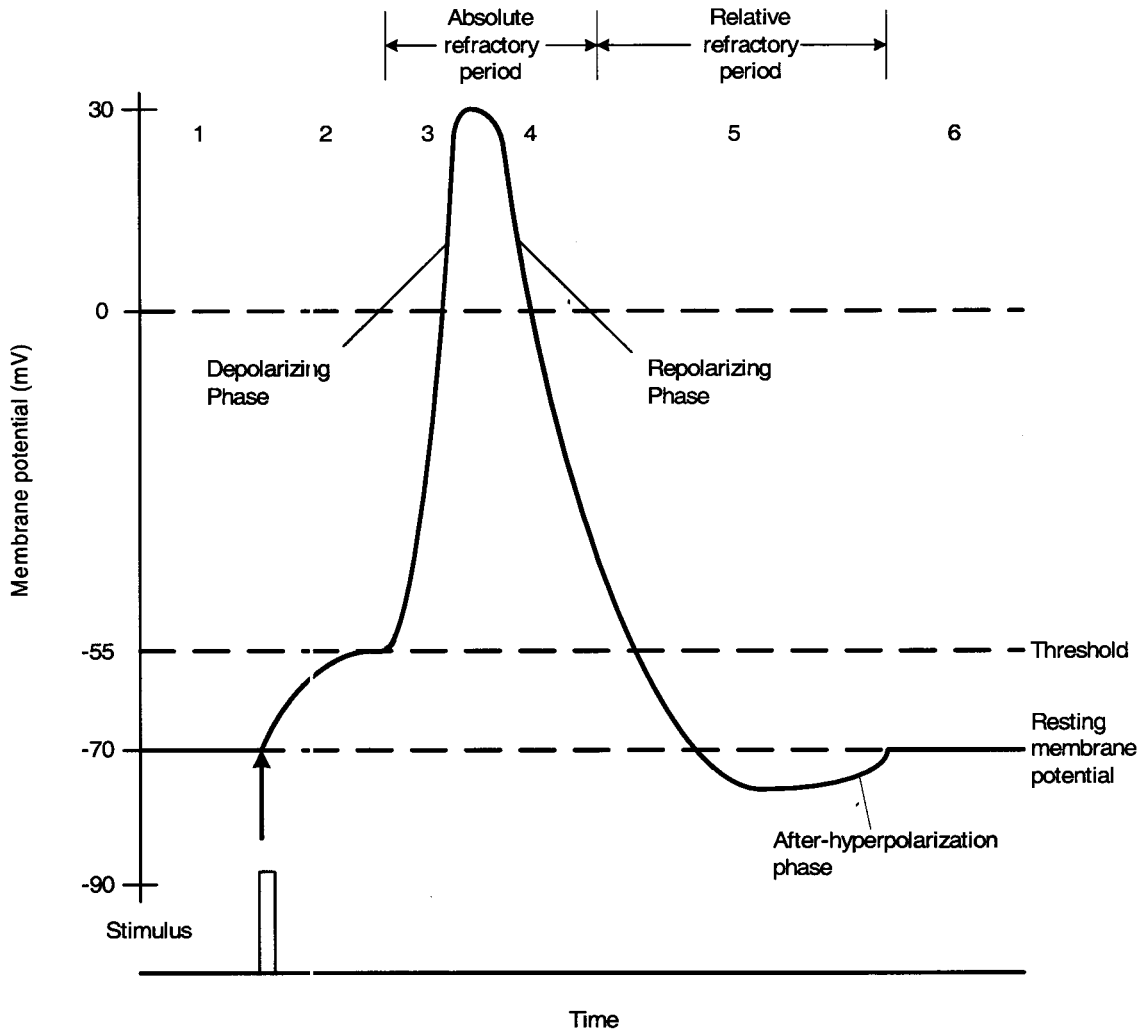

Figure 2.8: Action potential of a typical neuron. 1. Membrane is at rest, voltage-gated Na^+ and K^+ channels are closed; 2. depolarization occurs as a result of a stimulus; 3. membrane reaches threshold, voltage-gated Na^+ channels are active; 4. voltage-gated Na^+ channels close, voltage-gated K^+ channels open, and the membrane starts to repolarize; 5. some of voltage-gated Na^+ channels return to resting state, voltage-gated K^+ channels are still open and cause the membrane to hyperpolarize; 6. membrane returns to rest, all voltage-gated Na^+ and K^+ channels are closed. (Inspired from Tortora and Derrickson (2003), and reprinted with permission of John Wiley & Sons, Inc.)

5000-fold, creating the depolarizing phase of the action potential (Guyton, 2000). Shortly after this, the sodium channels are inactivated and the influx of Na^+ ions is stopped. Within the same instant the potassium-gated channels are activated permitting the flow of K^+ ions out of the nerve fiber. Therefore, the negativity of the inside of the cell is re-established again, known as the repolarization of the membrane. Voltage-gated potassium channels take more time to close than sodium channels. This causes K^+ ions to keep flowing out of the fiber even after the resting potential is reached. As a result the membrane becomes more negative (hyperpolarizes) briefly before it restores its resting state. It is not possible to elicit a new action potential when the membrane is still depolarized from the preceding action potential. This time period is called the *absolute refractory period.* During the absolute refractory period the sodium-gated channels are inactivated and no more Na^+ ions are allowed to pass in. Following the absolute refractory period is the *relative refractory period,* where stronger stimuli can excite the nerve. During this period, not all of the sodium channels have recovered from their inactivation state, and potassium channels are still open, permitting the outflow of positive K^+ ions, which oppose the inflow of Na^+ ions.

To trigger an action potential, the stimulus must exceed a certain threshold. Once this threshold is reached, the action potential propagates along the membrane in all directions away from the the site of stimulation. This is called the *all-or-nothing principle.* The mechanism by which an action potential propagates over the membrane starts when a point on the membrane is excited by a stimulus. Therefore, the membrane depolarizes and a local circuit is formed. Currents of the local circuit then flow to the adjacent resting membrane areas triggering them to depolarize and so on. The structure of the fiber governs the propagation of action potential along the axon. The axon is either unmyelinated or myelinated. An AP propagates in unmyelinated fibers continuously along the axonal membrane, where successive local circuits are formed along the membrane. In myelinated fibers, a myelin sheath of Schwann cell is wrapped around the axon several times. This sheath acts as an excellent insulator that decreases ion flow through the membrane by increasing membrane resistance and decreasing membrane capacitance. Between every two Schwann cells, there is a small unmyelinated area that allows the flow of ions, known as the *node of Ranvier.* An AP is generated in myelinated nerve fibers at nodes of Ranvier, at which a local circuit is formed between two consecutive nodes. This type of distant propagation is called *saltatory conduction.* One of the advantages of the myelination of fibers is that it allows the APs to propagate at higher velocity along the axon with minimum energy consumption. In this study we are more interested in myelinated nerve fibers, as the primary ANFs in humans are myelinated (Rattay et al., 2001b). Moreover, the model presented here is for a node of Ranvier.

Neurons communicate to other neurons via synapses. There are electrical and chemical synapses. In chemical synapses, there is no physical connection between two consecutive neurons. Instead, there exists a gap known as the synaptic cleft. The neuron preceding the cleft is called the presynaptic neuron, whereas the proceeding one is the postsynaptic

neuron. When an action potential arrives at the presynaptic axon terminal, calcium channels open to allow the influx of calcium ions. Consequently, synaptic vesicles containing neurotransmitter molecules fuse with the cell membrane and release their contents into the synaptic cleft region. Neurotransmitter molecules bind to neurotransmitter receptors on the surface of the postsynaptic neuron. The type of the post synaptic current depends on the type of ion channels gated by the postsynaptic receptor, which will be either (i) excitatory, that acts to depolarize the membrane and is called an excitatory post-synaptic current (EPSC); or (ii) inhibitory, that acts to hyperpolarize the membrane and is called an inhibitory post-synaptic current (IPSC) (Koch, 1999).

2.2.4 Ion Channels in Neuron Membrane

In the previous section, we discussed the mechanism by which an action potential is generated in nerve fibers and how ion channels are the main elements responsible for the rapid flow of ions across the membrane during an action potential. These channels are either voltage controlled or chemically controlled. Experiments involving voltage-clamp and pharmacological channel blockers have revealed that channels are highly selective to certain types of ions, such as Na^+, K^+, Cl^-, and Ca^{2+}. For instance, tetrodotoxin (TTX) blocks sodium channels and prevents the passage of I_{Na} current, leaving potassium channels untouched. Tetraethylammonium (TEA) blocks potassium channels and leaves the sodium channel functioning. The ion channels could be in one of two states, either active or inactive. An activated channel permits the flow of ions and creates an ionic current. The Nobel Prize winners, Neher and Sakmann, (1976) were able to record single-channel currents using their pioneered patch clamp techniques. Their studies have shown that single-channel currents are unitary current steps that appear abruptly when the channel suddenly is activated (open). They have found also that the gating kinetics controlling the opening and closing of the gates are stochastic, i.e. repetitive trials of the same stimulus do not produce the same response.

2.2.4.1 Voltage-gated Ion-Channels

The superfamily of voltage-gated ion channels is present in all excitable cells such as neurons and muscle cells. This group of ion channels includes voltage-gated Na^+, K^+, and Ca^+ channels. Channels open and close in response to changes in membrane potential. It was originally believed that channels of the same ion type respond equally regardless of the location and functionality of the cell containing the channel (Hille, 2001). However, pharmacological studies have shown diversity in a particular channel subtypes. For instance, there are about seven different kinds of voltage-gated K^+ channels in the axon of myelinated nerve fibers (Hille, 2001). This diversity is apparent also in Na^+ and Ca^+ channels. Moreover, channels are not evenly distributed along the axon. In myelinated nerve fibers, channel density at nodes of Ranvier are not equally distributed. Subtypes of a particular

ion channel respond differently, although they belong to the same ion channel family.

Experimental studies (Grigg et al., 2000; Manis and Marx, 1991; Perney and Kaczmarek, 1997; Perney et al., 1992) have shown the presence of more than one type of voltage-gated K^+ channels in the central auditory system, such as low-threshold, high-threshold, and transient K^+ channels. Another type of channel present in the auditory nerve neurons is *hyperpolarization-activated cation* channels, originally found in pace-making cells. Hyperpolarization-activated cation channels have permeability to both Na^+ and K^+ ions. If the membrane becomes excessively hyperpolarized, hyperpolarization-activated cation channels are activated and an action potential may be triggered.

Evidence of the presence of low-threshold potassium and hyperpolarization-activated cation voltage-gated channels at the nodes of Ranvier in axons of ANFs was described in several physiological studies (Mo and Davis, 1997a; Chen, 1997; Mo et al., 2002; Adamson et al., 2002). This diversity in ion-channel types has been shown to influence the shape, spike rate, refractoriness of the action potential. This may explain how action potentials contribute in the conveyance and encoding of the auditory signal. In this thesis, models for these two specific types of channels are examined.

2.3 Cochlear Implants

Cochlear implants (CIs), sometimes referred to as "bionic ears", are prosthetic electric devices used to partially restore hearing for individuals with severe or profound hearing loss.

2.3.1 Types of Hearing Loss

There are two types of hearing loss that result from hearing impairment of the ear: i) conductive hearing loss and ii) sensorineural hearing loss. Conductive hearing loss occurs in the external and middle ears (just before the cochlea) and may be due to a decrease in the ability of the ossicles to match the impedance between the external ear and the cochlea. This may result in a simple frequency-dependent attenuation (Pickles, 1982). Hearing aids are quite capable of effectively compensating for this type of hearing loss. Treatment of conductive hearing loss can also be by antibiotics or surgical intervention, depending on the causes of the loss.

On the other hand, sensorineural hearing loss occurs in the cochlea and/or auditory nerve. There are many causes that may produce sensorineural hearing loss, such as a tumor in the auditory nerve, acoustic trauma in the cochlea, drugs, infection of the cochlea, or aging. The degree of sensorineural hearing loss can range from mild to profound. Hair cells are the parts in the cochlea most likely to be affected in sensorineural hearing loss. Destruction of hair cells will result in the failure of the cochlea to convert sound into electrical signals that excite the cochlear nerve. Hearing aids may not help with destroyed hair

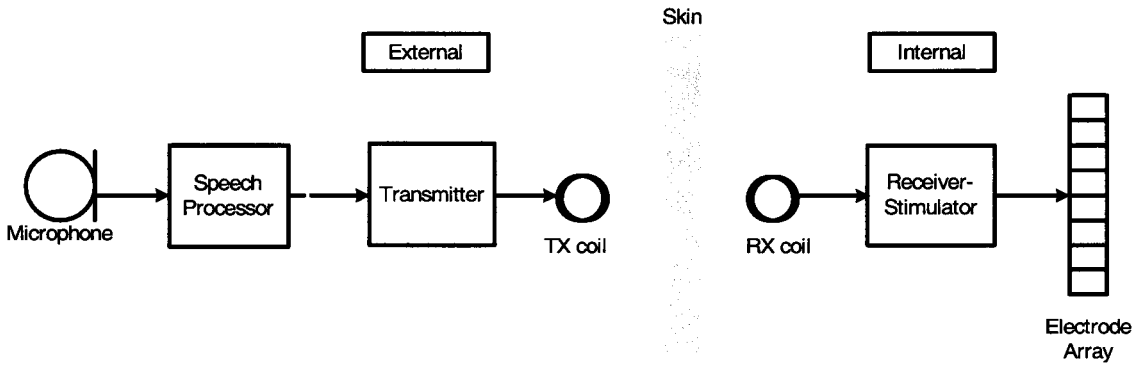

Figure 2.9: Block diagram showing the main components of a cochlear implant.

cells as they only amplify the intensity of sound entering the ear and depend on the natural parts of the hearing system in transferring the sound from the external ear to the auditory cortex. Restoration of hearing loss in this case can be achieved by means of a cochlear implant. Cochlear implants bypass the malfunctioning hair cells and electrically stimulate the surviving fibers of the auditory nerve directly. Although restoration of hearing using CIs is partial, yet patients with implanted CIs are able to respond to speech and environmental sounds, and many users can even understand conversations across the telephone using advanced CIs (Pickles, 1982; Clark, 2003).

2.3.2 Components of the Cochlear Implant

The components of a CI include those that are worn externally and those that are implanted, as illustrated in Fig. 2.9. The external portion consists of: i) a microphone, that transduces sound waves into electrical signals; ii) speech (sound) microprocessor, where analog signals are converted into digital signals, sound signals are analyzed into their frequency components and an *ad hoc* electrode stimulation code that fits the subject is generated; and iii) a RF (Radio Frequency) wireless transmitter, attached to the patient's scalp, in which the stimulation code is modulated with a carrier wave and sent via the transmitter. The internal portion is implanted inside the head and consists of: i) a receiver-stimulator, implanted in the mastoid bone, which receives and demodulates the signal sent by the external transmitter, and converts it into electrical current pulses corresponding to the sound signal; ii) an array of electrodes, inserted inside the cochlea, which stimulates the ANFs.

In the early development stages of CIs, ANFs were stimulated electrically using a single electrode. This type of electrode faced many technical problems. It was not capable of coding speech frequencies properly, speech at conversational levels were not understandable, and they did not make use of the tonotopic distribution of the spiral ganglion and surviving ANFs (Clark, 2003). Newer CIs use multiple-electrodes which make use of the neurophysiological tonotopic differentiation of ANFs. Experiments using multiple electrodes

have shown better results than their single electrode counterparts. Speech perception is significantly improved especially for postlinguistically deaf patients (Clark, 2003).

2.4 Summary

In this chapter, we explored the basic anatomy and physiology of the auditory system and how sound waves are converted into electrical nerve impulses by hair cells. Before the auditory signals reach the auditory cortex in the brain for perception, they pass through a series of encoding processes along the different stages of the auditory pathway. The cochlear nerve conveys auditory information from the cochlea to the central auditory pathways. The nerve consists of thousands of neurons. The membrane potential of neurons is governed by the concentration of ions in the intracellular and extracellular spaces. Ion channels, pores penetrating the cell membrane, control the flow of ions across the cell membrane. Voltage-gated ion channels are responsible for the generation of action potential in the neuron axon. When the membrane potential is moved more positive from its resting value, voltage-gated Na channels open, allowing rapid influx of Na^+ ions, and the membrane depolarizes. Thereafter, the membrane returns to its resting state by sodium channels inactivation and potassium channels activation. Single-channel recordings of ion channels has revealed that ion channel gating kinetics are stochastic in nature. Nonetheless, averaging several trials of single-channel current recordings produces current curves similar to the deterministic currents measured by Hodgkin and Huxley (1952). There is diversity in the types of ion channels within the same ion family. Each subfamily type poses different temporal response. Channel densities and distribution depend on their function and location.

Cochlear implants replace the function of destroyed hair cells and electrically stimulate ANFs to partially restore hearing of severely deaf patients. Stimuli are produced by an electrode array inserted inside the cochlea. Experiments have shown that better perception is achieved using a multiple-electrode assembly rather than a single-electrode.

Good understanding of the neurophysiology underlying the transmission of information in the auditory nerve would help produce better CI stimulation strategies.

Chapter 3

Motivation

3.1 Overview

In this chapter, the pertinent published literature is discussed. First, issues and challenges facing cochlear implant stimulation are explored. Second, ion channels and the role they may play in conveying the auditory signal in the auditory nerve are illustrated. Third, previous attempts to model the mammalian auditory nerve membrane and their limitations are explained. Finally, the objective of this thesis is highlighted.

3.2 Challenges Facing Cochlear Implant Stimulation

CIs stimulate ANFs by applying electrical current pulses via an electrode array inserted inside the cochlea. The mechanism by which the ANFs convey sound information in response to these stimuli is still not fully understood. The code of the sound signal is governed by the spatial and temporal response properties of the ANFs. Surprisingly, perception and recognition of sound have been successful for many CI users. However, this is not always the case for all CI users. A stimulation strategy may fit one patient and not fit the other. The implanted candidate undergoes extensive rehabilitation program postoperatively to improve his/her ability to hear environmental sounds, rhythms and patterns of speech, and to use lip reading. To help minimize such variability and improve the design of CI stimulation strategies, better understanding of the neurophysiological properties underlying the ANFs is required.

In this section, ANFs' temporal properties, such as relative noise, refractoriness, summation of responses of subthreshold stimuli, and adaptation to pulse-train stimulations, that are observed in physiological experiments involving CI stimulation are discussed.

3.2.1 Membrane Noise

Verveen and Derksen (1968) have investigated noise in membrane potential from myelinated nerve fibers of the sciatic nerve of the frog, *Rana temporaria*. Fig. 3.1 illustrates the presence of *fluctuations* in membrane voltage while the membrane is at rest ($-70\,\text{mV}$). These fluctuations showed a spectrum of $1/\text{f}$ and a Gaussian amplitude distribution. In an earlier study, Verveen (1962) showed that fluctuations in membrane potential are inversely proportional to node diameter. An average diameter of an axon at a node of Ranvier for a mammalian ANF ranges between $2-4\,\mu\text{m}$, and many nodes are even smaller (Bruce et al., 1999c). For instance, the diameter of the the ANF modelled in this study at the node of Ranvier is $\sim 1.5\,\mu\text{m}$ (Mino et al., 2004). Therefore, the noise activity in membrane potential becomes more significant when dealing with ANFs.

It has long been accepted that these membrane fluctuations are responsible for the *stochastic* behavior observed in action potential discharge. The stochastic behavior of the nerve membrane is evident in that ANFs do not discharge in response to every presentation of a single stimulating pulse. Furthermore, the probability for an AP to be produced is dependent on the stimulus intensity. In addition, randomness is also observed in the spike latency (Verveen, 1960; Bruce et al., 1999c). The probability that the stimulus current intensity, $I_{\text{inj}}(t)$, is greater than or equal to threshold, $I_{\text{TH}}(t)$, and noise , $I_{\text{noise}}(t)$, at time t is (Bruce et al., 2000a)

$$\begin{aligned} p(t) &= \Pr\{I_{\text{inj}}(t) \geq I_{\text{TH}}(t) + I_{\text{noise}}(t)\} \\ &= \Pr\{I_{\text{noise}}(t) \leq I_{\text{inj}}(t) - I_{\text{TH}}(t)\} \\ &= \int_{-\infty}^{I_{\text{inj}}(t)-I_{\text{TH}}(t)} f(x)\ \text{dx}, \end{aligned}$$

where $f(x)$ is the probability distribution of $I_{\text{noise}}(t)$ and is given by

$$f(x) = \frac{1}{\sqrt{2\pi}\sigma} \text{e}^{-x^2/2\sigma^2}.$$

The noise follows a Gaussian distribution with zero mean and standard deviation σ (Verveen and Derksen, 1968). Therefore, $p(t)$ can be rewritten as

$$p(t) = \frac{1}{2}\left(1 + \text{erf}\left(\frac{I_{\text{inj}}(t) - I_{\text{TH}}(t)}{\sqrt{2}\sigma}\right)\right), \tag{3.1}$$

where erf (error function) is the integrated-Gaussian function:

$$\text{erf}(x) \triangleq \frac{2}{\sqrt{\pi}} \int_0^x \text{e}^{-t^2}\ \text{d}t.$$

To quantify the variability in the discharge probability, Verveen (1960) defined two

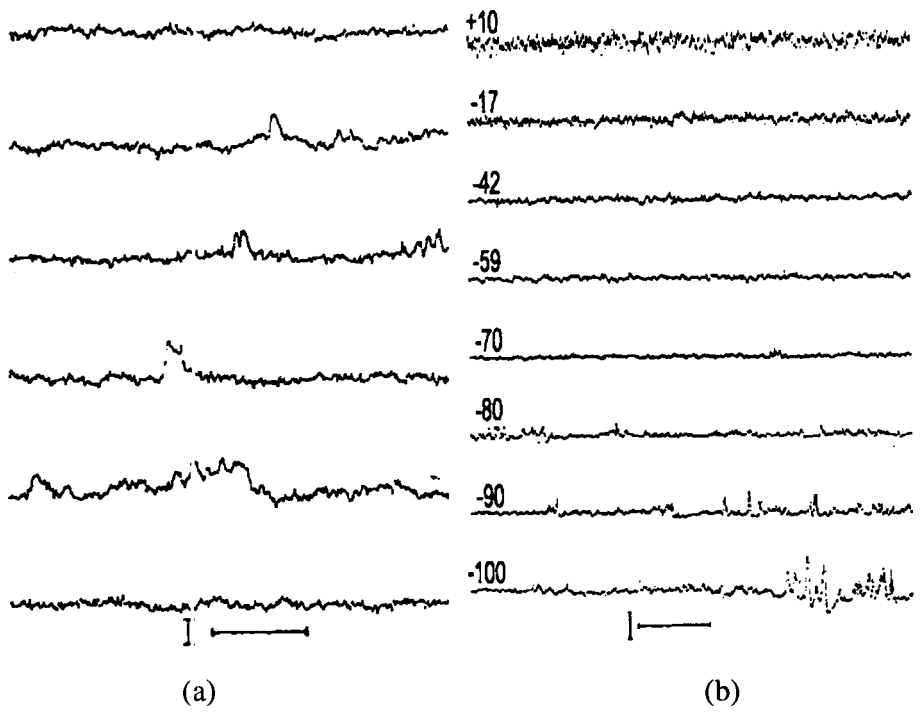

Figure 3.1: Fluctuations in nerve membrane potential recordings from (Verveen and Derksen, 1968) at the nodes of Ranvier. (a) Membrane potential at −90 mV. Horizontal scale: 10 ms; vertical scale: 1 mV. (Reprinted with permission from (Verveen and Derksen, 1968, Fig.20, p.913) ©1968 IEEE.) (b) Membrane potential traces at different holding potentials in mV. Horizontal scale: 10 ms; vertical scale: 5 mV. (Reprinted with permission from (Verveen and Derksen, 1968, Fig.19, p.913) ©1968 IEEE.)

variables: i) *threshold* (TH); and ii) *relative spread* (RS). The former is the stimulus current intensity required to excite the nerve with probability 0.5, while the latter is the coefficient of variation or the standard deviation normalized by the threshold, as shown in Fig. 3.2.

In a later study on cat AN fibers, Bruce et al. (1999c,a) reported the presence of stochastic activity in response to single- and train-current pulses. Their physiological data was successfully fitted by an integrated-Gaussian function, in contrast to the step-function predicted by a deterministic-threshold model. Moreover, they showed that RS increases with increasing the pulse width using biphasic stimulus pulses. They also noted that stochastic response of ANFs to electrical stimulation may be physiologically and psychologically significant (Bruce et al., 1999c,a,b).

Bruce et al. (1999c,a,b) have suggested that cochlear implants operating at intensities within the stochastic activity range of ANFs may improve CI functionality. That is, variance in discharge probabilities may have significant effects on the speech coding. Some CI research groups suggested stimulation strategies that induce noise in the nerve fibers,

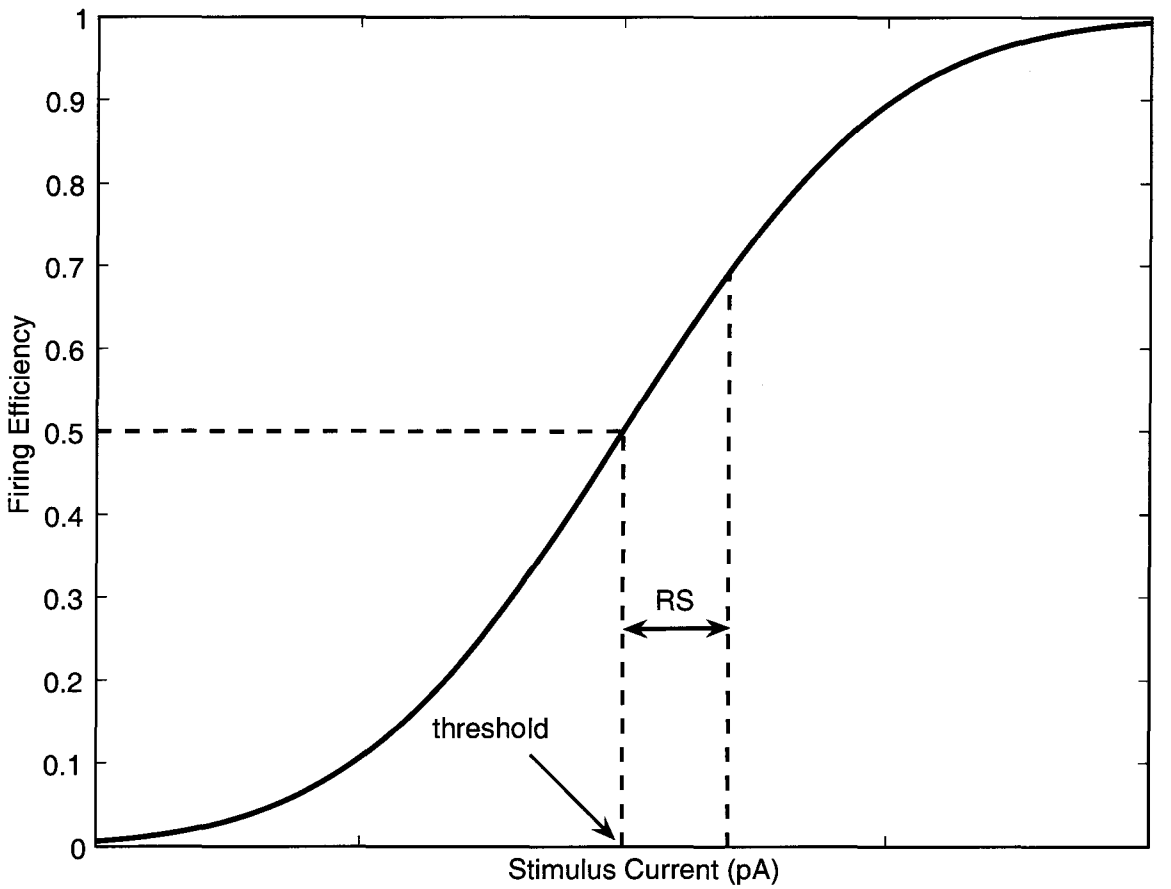

Figure 3.2: Definition of threshold and relative spread. *Threshold* is the stimulus current intensity at 0.5 firing probability. *Relative spread* in the ratio of standard deviation to threshold, $RS = \frac{\sigma}{Threshold}$.

to overcome problems associated with electrical stimulation (such as highly synchronized discharge patterns and refractory effects) as a way to improve speech perception of CIs users (Rubinstein et al., 1999; Litvak et al., 2001; Zhang et al., 2007; Miller et al., 2008).

3.2.2 Relative Refractoriness

Recall the definition of refractory periods in § 2.2.3.2: upon eliciting an action potential, there are two time periods that follow, i) the absolute refractory period (ARP), during which all the Na^+ channels are inactive and no another action potential can be generated irrespective of how high the stimulus intensity is; and ii) the relative refractory period (RRP), during which the Na^+ channels are partially returned to their resting state, and the K^+ channels are activated. An action potential can be generated by a higher amplitude stimulus pulse during

the RRP. Refractoriness is important in CI research. It has been argued that increasing the rate at which a CI stimulates the AN improves speech perception (Rubinstein et al., 1999; Miller et al., 2001a). Stimulation at these high rates more likely will hold the ANFs in a refractory state. Furthermore, physiological and modelling studies showed that stochastic activity in ANFs increases when they are in a condition of refractoriness (Miller et al., 2001a; Mino and Rubinstein, 2006), a result which may help to better understand encoding of speech signal in the AN and the improvement in speech perception associated with high stimulation rates for some CI users. Results from different physiological experiments also have shown variations in the values of ARP and the recovery time constants (Bruce et al., 1999c; Cartee et al., 2000; Miller et al., 2001a). Parameters such as firing efficiency, mean latency, jitter (standard deviation of latency), and relative spread provide useful information when investigating refractory properties. Incorporating refractory effects into ANF models indeed will improve the accuracy of computational models of the AN.

3.2.3 Spike Rate Adaptation

Among different cochlear implant and neurophysiology research groups, the definition of the term "adaptation" may vary. However, in this study, adaptation is defined as: reduction in spike rate in response to a pulse-train of "electrical" stimulations over time (Javel, 1996; Litvak et al., 2001; Mo et al., 2002; Zhang et al., 2007; Miller et al., 2008). Sometimes it is referred to as 'accommodation' (Sly et al., 2007). Specifying electrical stimulation here is needed as there are another type of adaptation, that is acoustic adaptation. During acoustic stimulation, reduction in the nerve spike rate has been noted. One possibility of acoustic adaptation effects is the depletion of neurotransmitters in the synaptic region of the inner hair cells (Javel, 1996; Mo et al., 2002; Nourski et al., 2006). Acoustic stimulation is beyond the scope of this study for the following reasons: i) in a deafened ear, the possibility of the presence of surviving hair cells is low; ii) the model presented in this study does not include any synaptic inputs; and iii) adaptation due to intrinsic properties of the membrane is evident in physiological studies that involves electrical stimulation (Litvak et al., 2001; Nourski et al., 2006; Zhang et al., 2007).

Although refractoriness and adaptation may have a combined effect in reducing the spike rate, distinction between the two terms is necessary. Refractory effects appear very rapidly after the onset of the stimulus and dominate along the whole stimulation period. As a result, the membrane spiking ability is locked at a minimum interspike interval (ISI) value governed by the ARP and RRP, i.e., depends only on the history of the previous spike. On the other hand, spike rate adaptation has a more cumulative effect, i.e. a reduction in spike rate appears after a considerable amount of time after onset.

It has been noted that the rate of adaptation is directly related to the stimulus rate, but can be reduced by increasing the stimulus level (Zhang et al., 2007; Miller et al., 2008). Axonal diameter may also have an influence on spike rate adaptation (Zhang et al., 2007), an observation which may be relevant to ANFs as they are characterized by having very small

diameters at the nodes of Ranvier. Adaptation is divided into: i) rapid adaptation, which appears directly after stimulus onset; ii) short-term adaptation, which extends over several milliseconds after stimulus onset; and iii) long-term adaptation, which has the time scale of hundreds of milliseconds (Javel, 1996; Zhang et al., 2007). Some other groups defined very-long-term adaptation effects, which extend over a few seconds and/or minutes (Javel, 1996).

The phenomenon of spike rate adaptation is observed during cochlear implant stimulation of the auditory nerve. This observation suggests that adaptation may have an influence on speech information coding. Results from physiological experiments have shown the presence of positive correlation between the spike rate adaptation and stimulus pulse rate (Zhang et al., 2007; Miller et al., 2008). Such results are important while designing CIs, especially as there is a growing trend towards using high rate stimuli. Furthermore, there is strong evidence that membrane adaptation originates more likely from the influence of different types of ion channels in the nerve membrane (Mo and Davis, 1997b; Mo et al., 2002; Rothman and Manis, 2003a; Adamson et al., 2002; Nourski et al., 2006).

It is of great demand to incorporate adaptation effects in computational models of the ANFs (Miller et al., 2008). Although much effort has been spent in modelling acoustic adaptation (Nourski et al., 2006), nonetheless, this is not the case for adaptation resulting from electrical stimulation. Having such a model will help in better understanding the mechanism of transformation of speech signal in the AN.

3.3 The Role of I_h and I_{KLT} Currents in Regulating the Action Potential

In § 2.2.4, it has been shown that there are different types of voltage-gated ion-channels present at the nodes of Ranvier of the ANFs. These ion channels configure the electrophysiological and temporal properties of the membrane, regulate patterns of excitability, and are non-uniformly distributed. Two types have been incorporated in most computational models, that is, fast Na^+ and delayed rectifier K^+ (Matsuoka et al., 2001; Mino et al., 2002, 2004). However, a limited number of studies have considered including other channels in their models (Huguenard and McCormick, 1992; Rothman and Manis, 2003b). In this report, two types of channels are selected to add to the model, for the reasons explained below. These channels are voltage-gated hyperpolarization-activated cation channels and voltage-gated low-threshold potassium channels, that permit the passage of I_h and I_{KLT} currents, respectively.

Bal and Oertel (2000), Adamson et al. (2002), and Mo et al. (2002) have shown that a low-threshold potassium current, I_{KLT}, is present in the spiral ganglion and the auditory nerve fibers. I_{KLT} differs from the delayed rectifier I_K in several respects: I_{KLT} i) activates at a lower membrane potential; ii) has an inactivation component; iii) has a non-zero

steady-state value; and iv) has a relatively slow inactivation component (Rothman and Manis, 2003b). I_{KLT} has several roles in regulating the action potential. First, it elevates the threshold level (Rothman and Manis, 2003c). Second, it adjusts the firing rate (Mo et al., 2002; Rothman and Manis, 2003c; Chen and Davis, 2006). Third, it reduces the membrane time constant (τ_m), therefore, the refractory time is reduced.

I_h is an inward rectifier current observed in different regions across the auditory system, such as the spiral ganglion (Mo and Davis, 1997a,b), ANFs (Chen, 1997), ventral cochlear nucleus (Golding et al., 1999; Rothman and Manis, 2003c; Rodrigues and Oertel, 2006; Bal and Oertel, 2000), and lateral lemniscus (Fu et al., 1997). I_h is characterized by being a mixed cation current (channels are permeable to both sodium and potassium ions), the reversal potential is more positive than the resting membrane potential, and it has slow activation/deactivation time constants (Mo and Davis, 1997a). I_h can be differentiated from the inward rectifier potassium current (I_{Kir}), because I_h is sensitive to Cs^+, whereas I_{Kir} is sensitive to Ba^{2+} (Chen 1997; Mo and Davis, 1997a; Bal and Oertel, 2000).

Rothman and Manis (2003c) and Bal and Oertel (2000) have shown that I_h is associated with I_{KLT} in the ventral cochlear nucleus neurons to modulate the I_{KLT}. I_h contributes also in determining the resting potential (Bal and Oertel, 2000), at which I_h is partially activated, and controls the spontaneous and evoked firing rates. In the spiral ganglion cells and ANFs, I_h causes an action potential to occur at the termination of a transient hyperpolarizing voltage (rebound firing), which may play a role in improving the firing rate following an inhibitory input (Mo and Davis, 1997a; Chen, 1997). Mo and Davis (1997a) have observed heterogeneity in I_h activation characteristics, i.e., reversal potential, half-maximal voltage ($V_{1/2}$), and slope factor (k), that are attributed to endogenous regulatory mechanisms which differ from one neuron to another in the spiral ganglion neurons. In addition, I_h may be responsible for the generation of spontaneous firing activity in the spiral ganglion and ANFs. These observations may have an implication on the signal coding in the auditory periphery.

3.4 Computational Models of the Nerve Membrane

3.4.1 Hodgkin and Huxley Deterministic Model

One of the key turning points in the history of neuroscience is the experiments carried out by Alan Hodgkin and Andrew Huxley (Hodgkin and Huxley, 1952). They measured the changes in membrane potential of the squid giant axon as a result of intracellular stimulus current injection. The squid axon was space clamped by inserting a highly conductive wire to maintain constant membrane potential along the entire axon (Hodgkin and Huxley, 1952). They modelled the generation of action potential as a function of the individual constituent currents and formed the equivalent electrical circuit model for the giant squid axon, shown in Fig. 3.3. Applying Kirchhoff's current law, the sum of ionic, leakage,

capacitance, and injected currents leads to a first-order differential equation. The membrane equation as postulated by Hodgkin and Huxley is

$$C_m \frac{dV}{dt} + I_{Na} + I_K + I_{leak} = I_{inj}. \tag{3.2}$$

The sodium current, I_{Na}, was modelled as

$$I_{Na} = \overline{G}_{Na} m^3 h (V - E_{Na}) \tag{3.3}$$

where $\overline{G}_{Na}$ is the maximum conductance and the sodium reversal potential is E_{Na}. Hodgkin and Huxley visualized the sodium channels as having three imaginary activating particles m and one inactivating particle h. m and h are dimensionless numbers, each between 0 and 1. m is the probability that the activating particle is in the open state while h is the probability of the inactivating particle to be in the *not* inactivating state (i.e. closed) (Koch, 1999), respectively. For a channel to conduct, all particles have to be in the permissive (open) state simultaneously. Each particle is assumed to transfer from on state to another—*open to closed* and *closed to open*, such that

$$m \underset{\alpha_m}{\overset{\beta_m}{\rightleftharpoons}} m-1 \quad \text{and} \quad h \underset{\alpha_h}{\overset{\beta_h}{\rightleftharpoons}} h-1. \tag{3.4}$$

The rate of change between states of these gating particles could be described by two first-order differential equations,

$$\frac{dm}{dt} = \alpha_m (V)(1-m) - \beta_m (V) m \tag{3.5}$$

and

$$\frac{dh}{dt} = \alpha_h (V)(1-h) - \beta_h (V) h, \tag{3.6}$$

where α_x and β_x are the transition rates of the states of gating particles from close to open and from open to close, respectively. They are functions of the membrane voltage and have the units of s^{-1}.

Similarly, the equation for the potassium current is

$$I_K = \overline{G}_K n^4 (V - E_K) \tag{3.7}$$

where $\overline{G}_K$ is the maximum conductance while E_K is the potassium reverse potential. In contrast to sodium, potassium has four activating particles n and no inactivating ones. Values for n are between 0 & 1 and are dimensionless. In order for the channel to conduct, the four particles have to be in the active state simultaneously. A single particle could hold one

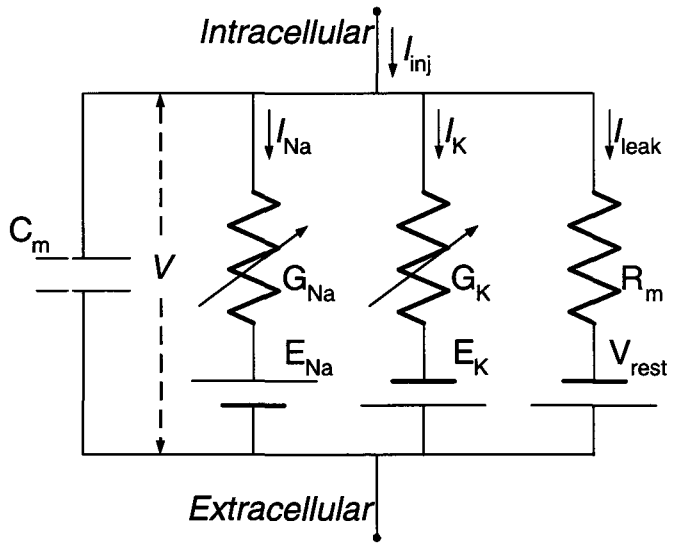

Figure 3.3: Equivalent circuit of Hodgkin and Huxley model for a patch of membrane of the squid giant axon. C_m is the membrane capacitance, G_{Na} & G_K are sodium & potassium conductances, and E_{Na} & E_K are sodium & potassium reverse potential. R_m is the membrane resistance and V_{rest} is the resting membrane potential. I_{inj} is the injected intracellular current.

of two states, closed or open, such that

$$n \underset{\alpha_n}{\overset{\beta_n}{\rightleftharpoons}} n-1. \tag{3.8}$$

The rate of change of a single particle is described by the first-order differential equation

$$\frac{dn}{dt} = \alpha_n(V)(1-n) - \beta_n(V)n, \tag{3.9}$$

where α_n and β_n are the transition rates of the states of gating particles from closed to open and from open to closed, respectively.

Hodgkin and Huxley's approach in analyzing the membrane action potential was both macroscopic and deterministic. Due to limitations of equipment at the time, they had to consider a large surface area of membrane. The ionic currents measured were the average of a large number of individual channel currents. The patch clamp techniques introduced by Neher and Sakmann (1976) enabled the recording of currents from a single channel. Studies have shown that as the number of channels per unit area increase, the recorded currents tend to show the classical macroscopic current curves of the Hodgkin-Huxley model (Hille, 2001).

3.4.2 Stochastic Models of Nerve fibers

Single-channel current recording, using "gigaseal" patch-clamp methods have revealed that channels open and close abruptly in a step-wise manner (Hille, 2001). Gating of channels is random, or *stochastic*.

A group of computational models which reflects the stochastic behavior of the ANFs have been developed such as in Strassberg and DeFelice (1993), Rubinstein (1995), Chow and White (1996), Fox (1997), Bruce et al. (1999c). Each of them tried to model ANFs in an efficient and robust way. Nevertheless, each has its advantages and drawbacks. Stochastic description of ANFs can be divided into two approaches: i) "biophysical"; and ii) "phenomenological". An example of the latter is the point process description, where the spikes of the neural fiber in response to electrical stimulation are mapped as discrete events occurring randomly in time (Koch, 1999). Although this approach is computationally efficient, it only describes the spiking phenomena without explaining the neural and stimulus parameters (Bruce et al., 1999c). The biophysical approach on the other hand is based on the Hodgkin and Huxley model. The advantage of the biophysical approach over the phenomenological is that the former dissects the membrane into discrete ion channels revealing the underlying physiological properties of the membrane. Biophysical models can be extended to describe a population of nerve fibers. The major problem associated with this type of models is that they are computationally intensive. Several methods have been suggested to simulate the stochastic gating kinetics of the biophysical model and can be divided into two categories: i) approximation algorithms; and ii) exact algorithms. Exact algorithms make use of Markov jumping process and can be subdivided into: (a) channel-state-tracking (CST); and (b) channel-number-tracking (CNT). Mino et al. (2002) made a comparison between four stochastic models: i) Fox (1997) (F) algorithm; ii) Strassberg and DeFelice (1993) (SD); iii) Rubinstein (1995) (R); and iv) Chow and White (1996) (CW), and one deterministic Hodgkin-Huxly model. They concluded that, although the approximation algorithm (F) is much faster computationally, compared to other stochastic models, it lacks accuracy. However, Bruce (2007) found that some inaccuracies in the F-model may be related to implementation methods used by Mino et al. (2002). The other three exact algorithms showed better accuracy at the expense of computational time. Chow and White (1996) model was 4-5 times faster than SD and R models (Mino et al., 2002). Even at longer time step intervals, CW showed better accuracy. The reduction in computation time in the CW-model could be attributed to the CNT algorithm they used, i.e. they track the number of channels in each state rather than tracking the state of each individual channel, like in CST.

3.5 The Purpose of This Study

In this thesis, the stochastic Hodgkin-Huxley model for the ANFs is modified to include low-threshold potassium and hyperpolarization-activated cation currents (I_{KLT} and

I_h, respectively). According to the aforementioned discussion, these two channels specifically are believed to be responsible for many phenomena observed in ANFs response when stimulated with cochlear implants. An exact channel-number-tracking (CNT) algorithm is elected to model the ion-channel gating kinetics. Emphasis will be placed on investigating the noise in membrane threshold and spike rate adaptation. In the subsequent chapters, full explanation of the model and the simulation results are presented.

Chapter 4

The Model

4.1 Overview

The proposed model is described here. An ANF node of Ranvier is modelled. The model consists of four voltage-gated ion channel currents: i) I_{Na}; ii) I_K; iii) I_{KLT}; and iv) I_h. A passive leakage current I_{lk} is also included. The model utilizes an algorithm to mimic the stochastic behavior in the channel gating. Model parameters, current equations, and the simulation algorithm are discussed below.

4.2 The Membrane Equation

Fibers of the auditory nerve are myelinated. Therefore, an action potential occurs only at nodes of Ranvier, where the density of the fast voltage-gated sodium channels (Na_v) is dominant (Hille, 2001; Rattay et al., 2001b). However, other channel types which participate in the formation of the action potential and transformation of the sound signals are present in addition to the fast sodium channels such as the delayed-rectifier voltage-gated potassium channels (Kv), low-threshold voltage-gated potassium channels (KLTv), fast transient voltage-gated potassium channels (KAv), and hyperpolarization-activated voltage-gated cation channels (HCNv). Most of the previous computational models of ANFs included only Na_v and Kv (Rubinstein, 1995; Bruce et al., 1999c; Miller et al., 1999a; Matsuoka et al., 2001; Litvak et al., 2001; Miller et al., 2001b; Mino et al., 2002, 2004; Mino and Rubinstein, 2006). In the previous chapter, it was described how models containing only these two types of channels do not accurately describe AN responses to cochlear implant stimulation.

In this study, a stochastic model of a whole patch of membrane of an AN node of Ranvier is presented, that includes hyperpolarization-activated cation channels and low-threshold potassium channels, in addition to the Na_v and Kv channels. Fig. 4.1 shows the equivalent circuit of a single node of Ranvier. The model is composed of five ionic currents,

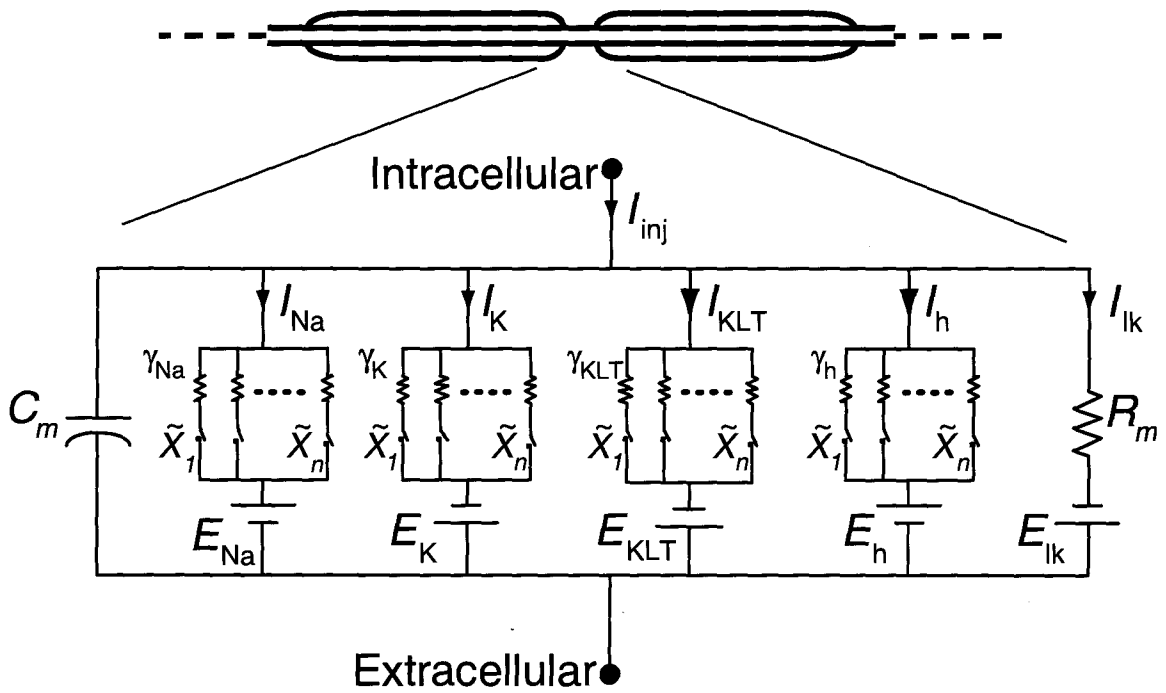

Figure 4.1: Model for a patch of membrane at a node of Ranvier: C_m, R_m, γ_x, E_x are the membrane capacitance, membrane resistance, single channel conductances, and reversal potentials, respectively. $\tilde{X}_n$ are the stochastic single-channel states (open or closed). E_{lk} is the leakage potential.

which are, $I_{Na}(t)$, $I_K(t)$, $I_{KLT}(t)$, $I_h(t)$, and $I_{lk}(t)$ controlled by Na_v, Kv, KLTv, HCNv, and leakage channels, respectively.

The complete membrane equation of Fig. 4.1 is given by the first-order differential equation

$$C_m \frac{dV(t)}{dt} + I_{Na}(t) + I_K(t) + I_{KLT}(t) + I_h(t) + I_{lk}(t) = I_{inj}(t), \tag{4.1}$$

where V is the relative membrane potential[1] in mV, C_m is the membrane capacitance (Table 4.1 on page 35), and I_{inj} is the stimulus current.

4.3 Modelling the I_{Na} and I_K Currents

Rubinstein (1995) and Mino et al. (2002) implemented a computational model for

[1]Relative membrane potential $V(t)$ is the difference between the membrane potential $V_m(t)$ and resting potential V_{rest} ($V(t) = V_m(t) - V_{rest}$). For the rest of this thesis the relative membrane potential (V) is used unless otherwise is specified.

Table 4.1: Summary of Parameters for the Membrane Model

Parameter	Symbol	Value	Unit	Reference
Membrane Capacitance	C_m	0.0714	pF	Bruce (2007)
Membrane Resistance	R_m	1953.49	MΩ	Bruce (2007)
Na Reversal Potential	E_{Na}	66	mV	Mino et al. (2002)
K Reversal Potential	E_{K}	−88	mV	Mino et al. (2002)
HCNv Reversal Potential	E_{h}	−43	mV	Rothman and Manis (2003b)
Resting Membrane Potential	V_{rest}	−78	mV	Mino et al. (2002)
Na Channel Conductance	γ_{Na}	25.69	pS	Mino et al. (2002)
Kv Channel Conductance	γ_{Kv}	50.0	pS	Mino et al. (2004)
KLTv Channel Conductance	γ_{KLT}	13.0	pS	Jason Rothman and Paul Manis, pers. comm.
HCNv Channel Conductance	γ_{h}	13.0	pS	see text
Max # of Na Channels	$N_{\mathrm{Na_v}}^{\mathrm{max}}$	1000		Mino et al. (2002)
Max # of Kv Channels	$N_{\mathrm{Kv}}^{\mathrm{max}}$	166		see text
Max # of KLTv Channels	$N_{\mathrm{KLT}}^{\mathrm{max}}$	166		see text
Max # of HCNv Channels	$N_{\mathrm{h}}^{\mathrm{max}}$	100		see text
KLTv Channels Thermal coefficient	$Q10_{\mathrm{KLT}}$	3.0		see text
HCNv Channels Thermal coefficient	$Q10_{\mathrm{h}}$	3.3		see text

sodium channels at a node of Ranvier of an ANF. The model was then extended to include potassium channels in Mino et al. (2004). Parameters of both models were originally based on an earlier study of Schwarz and Tomlinson (1987). Membrane kinetic parameters were maintained at mammalian body temperature, i.e., 37°C.

In this report, these two models are re-implemented and used as a base model (the standard Hodgkin-Huxley model at 37°C) to which the proposed model will be compared. However, some of the membrane parameters are different than those given in Mino et al. (2002), as there were some errors in their reported parameter values (Bruce, 2007).

In § 3.4.1, it was explained how Hodgkin and Huxley hypothesized that Na_v channels have three activating particles m and one inactivating particle h forming a total of eight distinct states, while Kv channels have four activating particles n of a total of five states. States are assumed to be independent, i.e., the transition rate from one state to another does not depend on the previous history of the system (Koch, 1999). Therefore, a good approach to model the states of stochastic ion channels is by using Markov jumping process (Koch, 1999; Mino et al., 2002). The equation describing transitions between states for the Na_v channels is

$$\begin{array}{ccccccc} m_0h_0 & \underset{\beta_m}{\overset{3\alpha_m}{\rightleftharpoons}} & m_1h_0 & \underset{2\beta_m}{\overset{2\alpha_m}{\rightleftharpoons}} & m_2h_0 & \underset{3\beta_m}{\overset{\alpha_m}{\rightleftharpoons}} & m_3h_0 \\ \alpha_h \downarrow\uparrow \beta_h & & \alpha_h \downarrow\uparrow \beta_h & & \alpha_h \downarrow\uparrow \beta_h & & \alpha_h \downarrow\uparrow \beta_h \\ m_0h_1 & \underset{\beta_m}{\overset{3\alpha_m}{\rightleftharpoons}} & m_1h_1 & \underset{2\beta_m}{\overset{2\alpha_m}{\rightleftharpoons}} & m_2h_1 & \underset{3\beta_m}{\overset{\alpha_m}{\rightleftharpoons}} & m_3h_1 \end{array} \tag{4.2}$$

where α_m is the transition rate for an m particle to change its state from closed to open (β_m is the transition rate for the opposite direction). Similarly, α_h is the transition rate for an h particle to make a transition from inactivated to deinactived (β_h is the transition rate for the opposite direction). For instance, at state m_1h_0, one of the three m particles is open (activated) and the other two are closed (deactivated) while the h is inactivated. In order for the channel to transfer to state m_2h_0, any of the two closed m particles can open at a transition rate of $2\alpha_m$, since m particles are independent of each other. If it is the case where the channel is moving to state m_0h_0, the only open m particle will close at rate constant β_m. Of the eight possible different states, there is only a single state at which the channel is conducting (i.e., open channel), that is m_3h_1 (all three m particles are open and h is deinactivated). The equations governing the transition rate constants α_m, β_m, α_h, and β_h for Na_v channels of ANFs at mammalian body temperature (Mino et al., 2002) are given by

$$\alpha_m(V) = \frac{1.872\,(V - 25.41)}{1 - \exp\left((25.41 - V)/6.06\right)}, \tag{4.3}$$

$$\beta_m(V) = \frac{3.973\,(21.001 - V)}{1 - \exp\left((V - 21.001)/9.41\right)}, \tag{4.4}$$

$$\alpha_h(V) = \frac{-0.549\,(27.74+V)}{1-\exp\left((V+27.74)/9.06\right)}, \tag{4.5}$$

$$\beta_h(V) = \frac{22.57}{1+\exp\left((56.0-V)/12.5\right)} \tag{4.6}$$

where α_m, β_m, α_h, and β_h are in ms^{-1}.

Similarly, the Markov state equation for Kv gating particles n is

$$n_0 \underset{\beta_n}{\overset{4\alpha_n}{\rightleftharpoons}} n_1 \underset{2\beta_n}{\overset{3\alpha_n}{\rightleftharpoons}} n_2 \underset{3\beta_n}{\overset{2\alpha_n}{\rightleftharpoons}} n_3 \underset{4\beta_n}{\overset{\alpha_n}{\rightleftharpoons}} n_4 \tag{4.7}$$

where α_n is the transition rate for a closed n particle to open and β_n is the transition rate for an n particle to make a transition from open to closed. A Kv channel is considered to be open (conducting) only when the gating particles are in state n_4. The transition rate constant equations are

$$\alpha_n(V) = \frac{0.129\,(V-35)}{1-\exp\left((35-V)/10\right)}, \tag{4.8}$$

$$\beta_n(V) = \frac{0.3236\,(35-V)}{1-\exp\left((V-35)/10\right)} \tag{4.9}$$

where α_n and β_n are in ms^{-1} (Mino et al., 2004).

Recalling (3.3) and (3.7), the current equations for $\mathrm{Na_v}$ and Kv can be rewritten as

$$I_{\mathrm{Na}}(t) = \gamma_{\mathrm{Na}} N_{m_3h_1}(t)\left[V(t) - (E_{\mathrm{Na}} - V_{rest})\right] \tag{4.10}$$

and

$$I_{\mathrm{K}}(t) = \gamma_{\mathrm{K}} N_{n_4}(t)\left[V(t) - (E_{\mathrm{K}} - V_{rest})\right] \tag{4.11}$$

where $N_{m_3h_1}(t)$ and $N_{n_4}(t)$ denote the number of sodium and potassium channels remaining in states m_3h_1 and n_4 at time t, respectively. γ_{Na} and γ_{K} are the single channel conductances for $\mathrm{Na_v}$ and Kv. E_{Na} and E_{K} are the reversal potentials. The estimated number of sodium channels at a node of Ranvier of a mammalian spiral ganglion cell is 1000, as defined in Matsuoka et al. (2001). The number of potassium channels is about one third of that of sodium. However, this number is divided equally between the delayed-rectifier and low-threshold potassium channels. Thus, each of Kv and KLT has 166 channels. A complete list of parameter values is given in Table 4.1 on page 35.

The steady-state of activation/inactivation gating particles $x_\infty(V)$ and time constant values $\tau_x(V)$ as a function of relative membrane voltage is illustrated in Fig. 4.2, where x stands for m, h, or n. The transition rate constants are related to steady-state and time

constant values by (Koch, 1999)

$$x_\infty = \frac{\alpha_x}{\alpha_x + \beta_x} \tag{4.12a}$$

and

$$\tau_x = \frac{1}{\alpha_x + \beta_x} \tag{4.12b}$$

4.4 Modelling the I_{KLT} Current

The model for I_{KLT} is derived from a previous study carried out by Rothman and Manis (2003b). Their study was aimed at investigating the roles of different potassium currents in the ventral cochlear nucleus (VCN) neurons. They carried out a group of voltage-clamp experiments and came up with a set of equations for I_{KA} (transient potassium current), I_{KHT} (high-threshold potassium), and I_{KLT}. Of these three currents, I_{KLT} is selected and included in the present model for the reasons discussed in § 3.3. Rothman and Manis (2003b) followed a Hodgkin-Huxley-like formalism in expressing the I_{KLT}, that is

$$I_{\mathrm{KLT}}(t) = \bar{g}_{\mathrm{KLT}} w^4 z (V_m(t) - E_{\mathrm{K}}) \tag{4.13}$$

where $\bar{g}_{\mathrm{KLT}}$ is the maximum conductance, while w and z are the activating and inactivating gating particles, respectively. Note that I_{KLT} was given in terms of membrane potential V_m rather than the resting membrane potential V. I_{KLT} has the same reversal potential as I_{K}, as they are both potassium channels—see Table 4.1 on page 35. The resting membrane potential in Rothman and Manis (2003b) was -63.6 mV and is denoted here as V_{rest}^{RM}. I_{KLT} has fourth-order activation kinetics w similar to the n^4 of I_{K} described by Hodgkin and Huxley (1952). I_{KLT} has also an incomplete slow inactivation particle z. Gating kinetics of I_{KLT} were expressed by Rothman and Manis (2003b) in terms of their steady-state values ($w_\infty(V_m)$ and $z_\infty(V_m)$) and time constants ($\tau_w(V_m)$ and $\tau_z(V_m)$) at 22°C, producing

$$w_\infty(V_m) = \frac{1}{(1 + \exp(-(V_m + 48)/6))^{1/4}} \tag{4.14}$$

$$z_\infty(V_m) = \frac{(1 - \xi)}{1 + \exp((V_m + 71)/10)} + \xi \tag{4.15}$$

$$\tau_w(V_m) = \frac{100}{6 \cdot \exp((V_m + 60)/6) + 16 \cdot \exp(-(V_m + 60)/45)} + 1.5 \tag{4.16}$$

$$\tau_z(V_m) = \frac{1000}{\exp((V_m + 60)/20) + \exp(-(V_m + 60)/8)} + 50 \tag{4.17}$$

where $\xi = 0.5$.

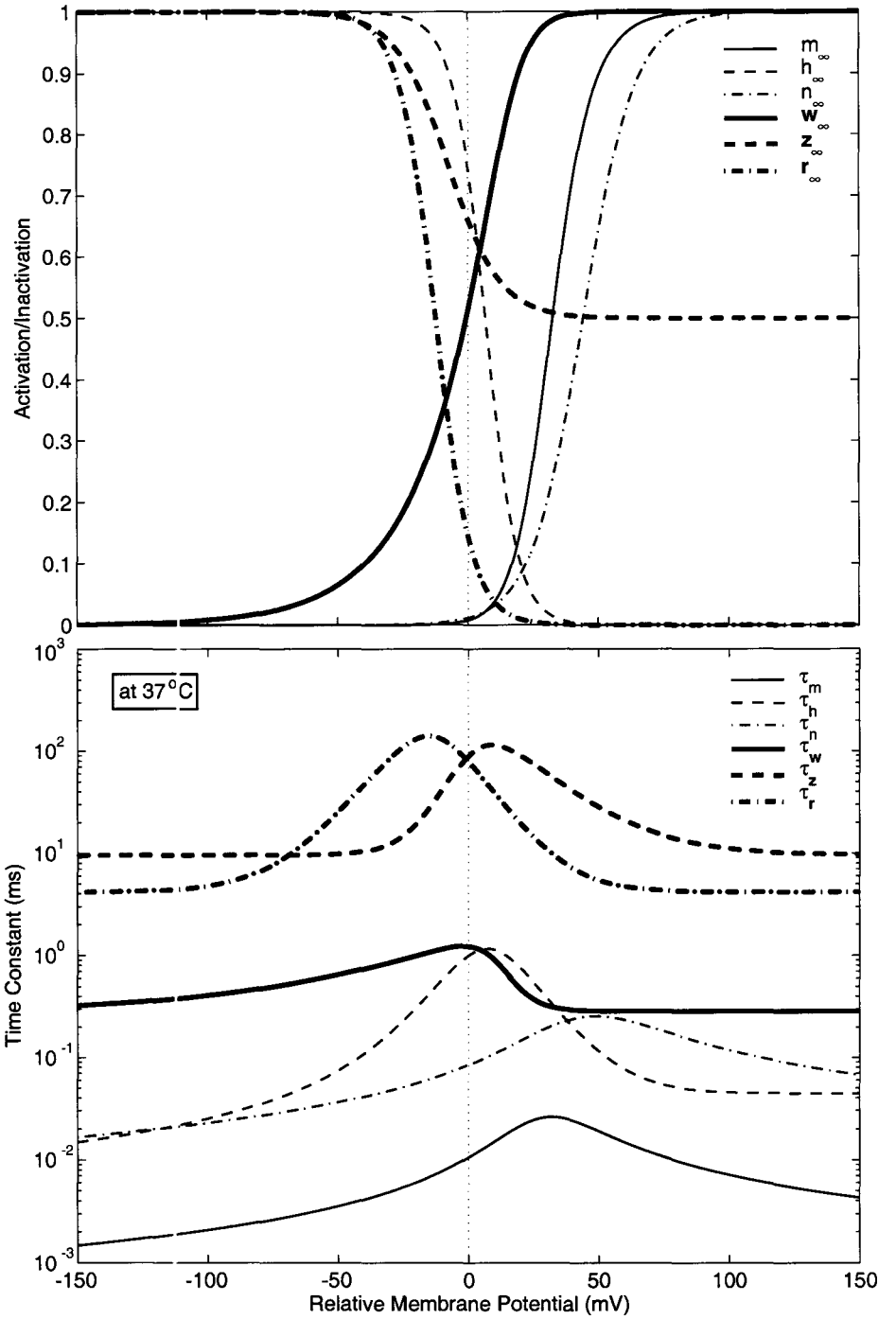

Figure 4.2: Relation of steady-state activation/inactivation and time constant of gating particles as a function of relative membrane voltage. Note that membrane voltage is in terms of relative membrane voltage, thus, the resting potential is at zero mV.

These equations are modified to match the membrane parameters of ANFs used in the present study. To adjust the operating temperature from 22°C to 37°C, the method described in Cartee (2000) is used. The time constants τ_w and τ_z are divided by the thermal coefficient constants, k_w and k_z, respectively,

$$k_x = Q10_x^{(T-T_0)/10.0} \tag{4.18}$$

where x denotes for w and z. The $Q10_x$ factor describes the increased speed of membrane kinetics when the temperature is increased by 10°C. T_0 is the original operating temperature and T is the desired temperature. The value of $Q10_w$ and $Q10_z$ is 3 (Rothman and Manis, 2003b) resulting in k_w and k_z of 5.19 (Fig. 4.3 shows the effect of the operating temperature on membrane kinetics). The difference in resting membrane potentials between this model and the one described in Rothman and Manis (2003c) is compensated by referring to relative membrane potential V rather than its absolute value V_m. Thus, V_m in (4.14), (4.15), (4.16), and (4.17) can be substituted with $V + V_{rest}^{\mathrm{RM}}$. Equations (4.14), (4.15), (4.16), and (4.17) can be rewritten in terms of relative membrane potential and the higher operating temperature (see Fig. 4.2) as follows

$$w_\infty(V) = \frac{1}{\left(1+\exp\left(-\left(V+V_{rest}^{\mathrm{RM}}+48\right)/6\right)\right)^{1/4}}, \tag{4.19}$$

$$z_\infty(V) = \frac{(1-\xi)}{1+\exp\left(\left(V+V_{rest}^{\mathrm{RM}}+71\right)/10\right)} + \xi, \tag{4.20}$$

$$\tau_w(V) = \left[\frac{100}{6\cdot\exp\left(\left(V+V_{rest}^{\mathrm{RM}}+60\right)/6\right)+16\cdot\exp\left(-\left(V+V_{rest}^{\mathrm{RM}}+60\right)/45\right)}+1.5\right]\Big/k_w, \tag{4.21}$$

$$\tau_z(V) = \left[\frac{1000}{\exp\left(\left(V+V_{rest}^{\mathrm{RM}}+60\right)/20\right)+\exp\left(-\left(V+V_{rest}^{\mathrm{RM}}+60\right)/8\right)}+50\right]\Big/k_z. \tag{4.22}$$

The model presented in Rothman and Manis (2003b) was deterministic and needs to be converted into a stochastic representation to include in the proposed model. Therefore, the same criteria used in § 4.3 for stochastic representation of Na_v and Kv channels is exploited. Low-threshold potassium channels can be in one of ten states (four w and one z

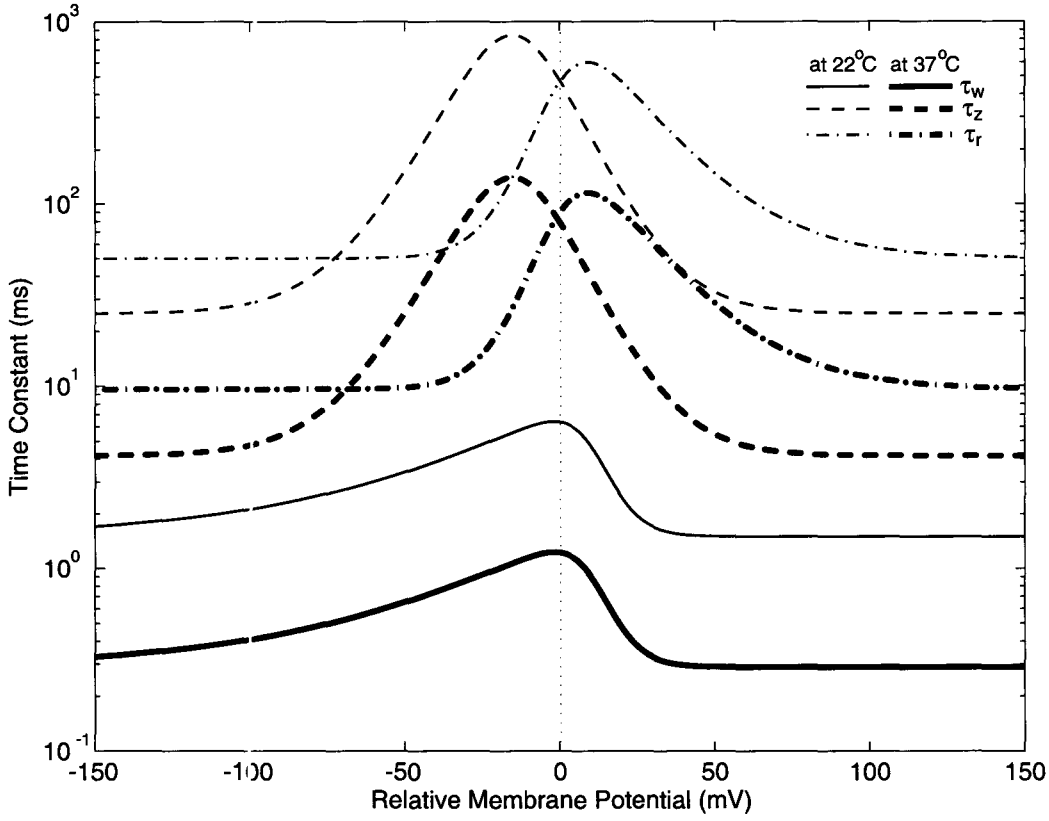

Figure 4.3: The effect of adjusting the operating temperature on membrane kinetics. The time constants of I_{KLT} and I_{h} are plotted as a function of relative membrane potential at operating temperatures of 22°C (thin lines) and 37°C (thick lines).

gating particles). Hence, the Markov state equation for I_{KLT} is

$$\begin{array}{ccccccccc} w_0z_0 & \underset{\beta_w}{\overset{4\alpha_w}{\rightleftharpoons}} & w_1z_0 & \underset{2\beta_w}{\overset{3\alpha_w}{\rightleftharpoons}} & w_2z_0 & \underset{3\beta_w}{\overset{2\alpha_w}{\rightleftharpoons}} & w_3z_0 & \underset{4\beta_w}{\overset{\alpha_w}{\rightleftharpoons}} & w_4z_0 \\ \alpha_z \downuparrows \beta_z & & \alpha_z \downuparrows \beta_z & & \alpha_z \downuparrows \beta_z & & \alpha_z \downuparrows \beta_z & & \alpha_z \downuparrows \beta_z \\ w_0z_1 & \underset{\beta_w}{\overset{4\alpha_w}{\rightleftharpoons}} & w_1z_1 & \underset{2\beta_w}{\overset{3\alpha_w}{\rightleftharpoons}} & w_2z_1 & \underset{3\beta_w}{\overset{2\alpha_w}{\rightleftharpoons}} & w_3z_1 & \underset{4\beta_w}{\overset{\alpha_w}{\rightleftharpoons}} & w_4z_1 \end{array}, \tag{4.23}$$

where α_w, β_w, α_z, and β_z are the transition rate constants. Transition rate constants are obtained from (4.19), (4.20), (4.21), and (4.22) by substituting in (4.12a) and (4.12b). The channel conducts only at state w_4z_1.

The current equation (4.13) can now be rewritten in a stochastic form as

$$I_{\mathrm{KLT}}(t) = \gamma_{\mathrm{KLT}} N_{w_4z_1}(t) \left[V(t) - (E_{\mathrm{K}} - V_{rest})\right] \tag{4.24}$$

where γ_{KLT} is the single channel conductance and $N_{w_4z_1}(t)$ is the number of KLT channels in state w_4z_1 at time t. Single channel conductance for I_{KLT} has not been determined precisely yet. However, the estimated value of γ_{KLT} used in this model was provided kindly from Drs. Paul Manis and Jason Rothman (personal communication). The number of channels at a single node is also undetermined. Consequently, the number of low-threshold potassium channels $N_{KLT}^{\max}$ is assumed to be 166 (about half the estimate number of potassium channels) as discussed earlier.

4.5 Modelling the I_{h} Current

I_{h} has been investigated by several neuroscience groups (Huguenard and McCormick, 1992; Chen, 1997; Mo and Davis, 1997a; Bal and Oertel, 2000; Rodrigues and Oertel, 2006), resulting in the derivation of several models. However, Mo and Davis (1997a) have shown that there is a range of variability in the parameter values of I_{h}, such as the half-maximal voltages ($V_{1/2}$) and the slope factor (k). The model for I_{h} described in Rothman and Manis (2003b) is utilized. Rothman and Manis (2003c) derived their model based on five voltage-clamp experiments (three related to auditory neurons and two to nonauditory neurons).

The equation for I_{h} given by (Rothman and Manis, 2003b) is

$$I_{\mathrm{h}}(t) = \bar{g}_{\mathrm{h}} r(t) \left(V_m(t) - E_{\mathrm{h}}\right) \tag{4.25}$$

where $\bar{g}_{\mathrm{h}}$ is the maximum conductance, r is the activating gating particle, and E_{h} is the reversal potential (see Table 4.1 on page 35). The activation particle r is described by first-order kinetics. The steady-state and time constant functions are

$$r_\infty(V_m) = \frac{1}{1+\exp\left(\left(V_m+76\right)/7\right)}, \tag{4.26}$$

$$\tau_r(V_m) = \frac{10^5}{237\cdot\exp\left(\left(V_m+60\right)/12\right)+17\cdot\exp\left(-\left(V_m+60\right)/14\right)}+25, \tag{4.27}$$

respectively (Rothman and Manis, 2003b), at 22°C.

The operating temperature is adjusted to 37°C by dividing the time constant function by k_r as determined by equation (4.18) (see Fig. 4.3). The $Q10_r$ value used in this model is 3.3, which produces a thermal coefficient constant value k_r of 5.99. This choice is prompted by (Rodrigues and Oertel, 2006) who suggested a value of 3.3 ± 0.3 for $Q10_r$. However, this value is somewhat different than that in Rothman and Manis (2003a) as they used a $Q10_r$ value of 3.0 resulting in 0.2 difference in k_r value. This difference is very small. The exact value of $Q10_r$ is speculative (Rothman and Manis, 2003b).

The same method used to compensate for membrane potential difference in I_{KLT} is used here. The modified versions of (4.26) and (4.27) in terms of relative membrane voltage at 37°C are

$$r_\infty(V) = \frac{1}{1+\exp\left(\left(V+V_{rest}^{RM}+76\right)/7\right)}, \tag{4.28}$$

$$\tau_r(V) = \left[\frac{10^5}{237\cdot\exp\left(\left(V+V_{rest}^{RM}+60\right)/12\right)+17\cdot\exp\left(-\left(V+V_{rest}^{RM}+60\right)/14\right)}+25\right]\Big/k_r, \tag{4.29}$$

respectively, and are shown in Fig. 4.2.

r can be in one of two states r_0 or r_1. The Markov representation for r kinetics is

$$r_0 \underset{\beta_r}{\overset{\alpha_r}{\rightleftharpoons}} r_1 , \tag{4.30}$$

where α_r and β_r are the transition rate constants, and are calculated from (4.12a) and (4.12b). The channel is open in state r_1. The equation for the I_h current therefore is

$$I_h(t) = \gamma_h N_{r_1}(t)\left[V(t)-(E_h-V_{rest})\right] \tag{4.31}$$

where γ_h and N_{r_1} are the single channel conductance and number of channels in state r_1, respectively (see Table 4.1 on page 35). Values of γ_h and N_h^{max} are totally speculative. Rothman and Manis (2003b) suggested that the maximum conductance value $\bar{g}_h$ for I_h is one-tenth that of I_{KLT} for VCN neurons. Thus, $\bar{g}_h$ could be between 0.83 and 1.66 nS (assuming that $\bar{g}_{KLT} = 50\,\text{pS} \times 166$ channels or $\times 333$ channels, respectively). Therefore, a value of 13 pS is assumed for γ_h and 100 channels for N_h^{max}, resulting in $\bar{g}_h = 1.3$ nS.

4.6 Modelling the I_{lk} Current

The leakage current $I_{lk}(t)$ is linearly dependent on the membrane voltage and is given by

$$I_{lk}(t) = \bar{g}_{lk}\left[V_m(t)-(E_{lk}-V_{rest})\right] \tag{4.32}$$

where $\bar{g}_{lk} = 1/R_m$ and R_m is the membrane resistance (Table 4.1 on page 35). The leakage reversal potential (E_{lk}) is set to maintain a constant resting membrane potential at -78 mV across the different versions of the model. This is achieved according to

$$\begin{aligned} E_{lk} = R_m\Big[&V_{rest}\left(\gamma_{Na}N_{Na}^{max}m_\infty^3 h_\infty+\gamma_K N_K^{max}n_\infty^4+\gamma_{KLT}N_{KLT}^{max}w_\infty^4 z_\infty+\gamma_h N_h^{max}r_\infty+\bar{g}_{lk}\right)\\ &-\left(\gamma_{Na}N_{Na}^{max}m_\infty^3 h_\infty E_{Na}+\gamma_K N_K^{max}n_\infty^4 E_K+\gamma_{KLT}N_{KLT}^{max}w_\infty^4 z_\infty E_{KLT}+\gamma_h N_h^{max}r_\infty E_h\right)\Big]. \end{aligned} \tag{4.33}$$

4.7 Simulation Algorithm of the Stochastic Model

4.7.1 Numerical Solution

The first-order differential equation (4.1), i.e, the membrane equation, is solved by applying Euler's integration method (Strogatz, 2000) which is defined as

$$\begin{aligned} \frac{\mathrm{d}x(t)}{\mathrm{d}t} &= f[x(t)] \\ x(t_{k+1}) &\approx x(t_k) + f[x(t_k)]\,\Delta t \qquad (k = 0,1,2,\ldots,n). \end{aligned} \tag{4.34}$$

Despite the simplicity and computation speed efficiency of Euler's method, it is always associated with a deviation error from the exact solution. This problem can be overcome by choosing a small time step Δt of 1 μs (Mino et al., 2002; Bruce, 2007). The discrete-time difference equation version of (4.1) is

$$V[k+1] = V[k] + \left(I_{\mathrm{inj}}[k] - I_{\mathrm{Na}}[k] - I_{\mathrm{K}}[k] - I_{\mathrm{KLT}}[k] - I_{\mathrm{h}}[k]\right)\Delta t / C_m \tag{4.35}$$

where $(k = 0,1,2,\ldots,n)$ is the number of iterations. The model simulation programs were written using Matlab® software (version 7.1) running on IBM BladeCenter computation servers.

4.7.2 The Stochastic Algorithm

A channel-number-tracking (CNT) algorithm has been developed to simulate the stochastic activity in ion channels of the ANF. The algorithm was utilized by Chow and White (1996) to model fluctuations in neuronal ion channels. Mino et al. (2002) compared Chow and White's CNT algorithm (CW) (illustrated in Fig. 4.4) with other three stochastic model algorithms used in modelling the neural membrane. They have shown that (CW) algorithm is the most accurate approach, making use of the memoryless and statistical independence of ion channels.

Recalling the Markov kinetic schemes (4.2), (4.7), (4.23), and (4.30) for channels $\mathrm{Na_v}$, Kv, KLT, and HCN, respectively, the lifetime of any channel to stay in a particular state at $t = t_0$ in multichannel systems has the probability density function (p.d.f.)

$$p(t) = \lambda(t)\exp\left[-\lambda(t)\cdot(t-t_0)\right], \quad t \geq t_0 \tag{4.36}$$

where $\lambda(t)$ is the effective transition rate and is expressed as

$$\lambda(t) = \sum_{i=0}^{3}\sum_{j=0}^{1} N_{m_i h_j}(t)\,\zeta_{ij}(t) + \sum_{k=0}^{4} N_{n_k}(t)\,\delta_k(t) + \sum_{p=0}^{4}\sum_{q=0}^{1} N_{w_p z_q}(t)\,\psi_{pq}(t) + \sum_{\kappa=0}^{1} N_{r_\kappa}(t)\,\varepsilon_\kappa(t) \tag{4.37}$$

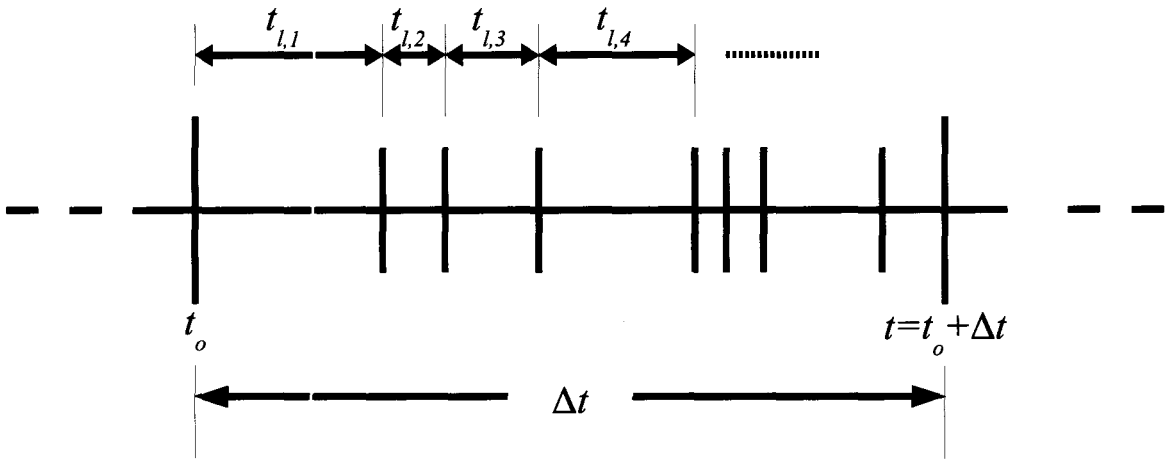

Figure 4.4: Chow and White (CW) CNT algorithm during one Euler time step Δt (indicated by the large vertical ticks). During a single time step, the number of channels in each state is continuously updated. The life time, $t_{l,i}$, (indicated by the smaller vertical ticks) of all channels to remain in their current states is determined by the value of a pseudorandom number, where $t_0 + t_{l,i} < t_0 + \Delta t$ and i is the recursion index. The number of channels in the current and next states is updated according to a second pseudorandom number after the time $t = t_0 + t_{l,i}$ has elapsed. The process continues and new life times and state transitions are generated until $t_0 + t_{l,i} > t_0 + \Delta t$ is reached.

where $N_{m_i h_j}$, N_{n_k}, $N_{w_p z_q}$, and N_{r_κ} are the numbers of I_{Na}, I_{K}, I_{KLT}, and I_{h} channels in states $m_i h_j$, n_k, $w_p z_q$, and r_κ, respectively. $\zeta_{ij}(t)$, $\delta_k(t)$, $\psi_{pq}(t)$, and $\varepsilon_\kappa(t)$ are the sums of transition rate constants associated with escapes from states $m_i h_j$, n_k, $w_p z_q$, and r_κ, respectively, and are given by

$$
\begin{cases}
\zeta_{00}(t) = 3\alpha_m + \alpha_h \\
\zeta_{10}(t) = \beta_m + \alpha_h + 2\alpha_m \\
\zeta_{20}(t) = 2\beta_m + \alpha_h + \alpha_m \\
\zeta_{30}(t) = 3\beta_m + \alpha_h \\
\zeta_{01}(t) = 3\alpha_m + \beta_h \\
\zeta_{11}(t) = \beta_m + \beta_h + 2\alpha_m \\
\zeta_{21}(t) = 2\beta_m + \beta_h + \alpha_m \\
\zeta_{31}(t) = 3\beta_m + \beta_h \\
\\
\delta_0(t) = 4\alpha_n \\
\delta_1(t) = 3\alpha_n + \beta_n \\
\delta_2(t) = 2\alpha_n + 2\beta_n \\
\delta_3(t) = \alpha_n + 3\beta_n \\
\delta_4(t) = 4\beta_n
\end{cases}
\qquad
\begin{cases}
\psi_{00}(t) = 4\alpha_w + \alpha_z \\
\psi_{10}(t) = \beta_w + \alpha_z + 3\alpha_w \\
\psi_{20}(t) = 2\beta_w + \alpha_z + 2\alpha_w \\
\psi_{30}(t) = 3\beta_w + \alpha_z + \alpha_w \\
\psi_{40}(t) = 4\beta_w + \alpha_z \\
\psi_{01}(t) = 4\alpha_w + \beta_z \\
\psi_{11}(t) = \beta_w + \beta_z + 3\alpha_w \\
\psi_{21}(t) = 2\beta_w + \beta_z + 2\alpha_w \\
\psi_{31}(t) = 3\beta_w + \beta_z + \alpha_w \\
\psi_{41}(t) = 4\beta_w + \beta_z \\
\\
\varepsilon_0(t) = \alpha_r \\
\varepsilon_1(t) = \beta_r
\end{cases}
\tag{4.38}
$$

The lifetime t_l for all channels to stay in their current state at $t = t_0$ before migrating to the next state at $t = t_0 + t_l$ is determined by drawing a pseudorandom number ρ_1 from the uniform distribution $[0,1]$, where

$$t_l = -\frac{\ln(\rho_1)}{\lambda(t)}. \tag{4.39}$$

After the time $t = t_0 + t_l$ has elapsed, the number of channels in one of the 56 transition states of the multichannel system is updated. The selection of the transition states is based on their probability of transition. The designated transition state is determined by generating a second pseudorandom number ρ_2 uniformly distributed within [0,1] and comparing it to the cumulative state transition probability ($P_i(t_0)$) at time t_0, where

$$P_i(t_0) = \sum_{j=0}^{i} \frac{\eta_j}{\lambda(t_0)} \qquad (i = 0,1,\ldots,56) \tag{4.40}$$

where η_j (given in (4.42) on page 49) is the state transition of channels in a particular state and $\frac{\eta_j}{\lambda(t_0)}$ is the state transition probability of that particular state. $P_i(t_0)$ is within [0,1].

If ρ_2 falls between $[P_{i-1}(t_0), P_i(t_0)]$ for $(i = 1,2,3,\ldots,56)$, then the ith state transition takes place. Therefore, the number of channels at time $t = t_0 + t_l$ is updated such that the number of channels in the current state decrements by one channel and the number of channels in the next state increments by one channel (i.e., assume a current state x_1 and a next state x_2, therefore, $N_{x_1} := N_{x_1} - 1$ and $N_{x_2} := N_{x_2} + 1$). The same procedure is repeated and a new lifetime is generated ($t = t_0 + t_{l,1} + t_{l,2} + t_{l,3} + \cdots$,—see Fig. 4.4) until $t > t_0 + \Delta t$. Hence, (4.35) integrates one step and proceeds to the next iteration.

The distribution of the number of channels among the states of gating particles is initialized before integrating (4.35). Channels are allowed to fluctuate for about 200 ms (1.5 times greater than the maximum time constant, τ_r). The number of channels in each state at the last 50 ms are averaged and used as an initial estimate feed for the number of channels in each state for the rest of the simulations. Fig. 4.5 shows kinetics as a function of time for the six gating particles $\hat{m}$, $\hat{h}$, $\hat{n}$, $\hat{w}$, $\hat{z}$, and $\hat{r}$. Values of stochastic gating particles are estimated using the empirical method suggested in Bruce (2007), where the fraction of a

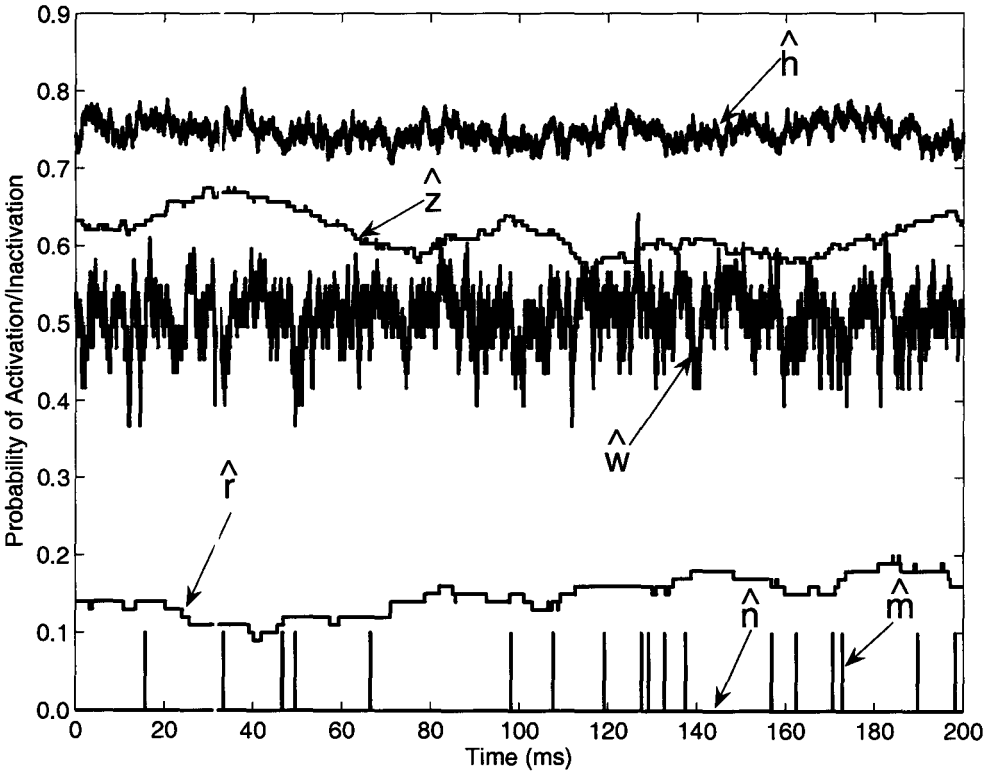

Figure 4.5: Stochastic steady-state kinetics, used in estimating the initial number of channels, as a function of time for the six gating particles $\hat{m}$, $\hat{h}$, $\hat{n}$, $\hat{w}$, $\hat{z}$, and $\hat{r}$. the last 50 ms of the channels ensemble are averaged and used as an initial estimate feed of the number of channels in each state for the rest of the simulations.

particular gating particle to be open is given by

$$\begin{aligned}
\hat{m} &= \left(\frac{N_{m_3h_0} + N_{m_3h_1}}{N_{\mathrm{Na}}^{\max}}\right)^{1/3} \\
\hat{h} &= \frac{N_{m_0h_1} + N_{m_1h_1} + N_{m_2h_1} + N_{m_3h_1}}{N_{\mathrm{Na}}^{\max}} \\
\hat{n} &= \left(\frac{N_{n_4}}{N_{\mathrm{K}}^{\max}}\right)^{1/4} \\
\hat{w} &= \left(\frac{N_{w_4z_0} + N_{w_4z_1}}{N_{\mathrm{KLT}}^{\max}}\right)^{1/4} \\
\hat{z} &= \frac{N_{w_0z_1} + N_{w_1z_1} + N_{w_2z_1} + N_{w_4z_1}}{N_{\mathrm{KLT}}^{\max}} \\
\hat{r} &= \frac{N_{r_1}}{N_{\mathrm{h}}^{\max}}
\end{aligned} \tag{4.41}$$

4.8 Summary

In this chapter, a computational stochastic model for a node of Ranvier of an ANF was implemented. Four stochastic voltage-gated ion channels currents were modelled, including I_{Na}, I_K, I_{KLT}, and I_h. The operating temperature was adjusted to mammalian body temperature (i.e., 37°C). Single channel conductances and number of channels for I_{KLT} and I_h were assumed based on the available data in the published literature. Channel-gating kinetics were expressed by a Markov jumping process. Channels conduct only at the state where all the gating particles are active. A channel-number-tracking (CNT) algorithm was used to imitate the randomness in gating fluctuations. Euler's method was utilized to integrate the first-order differential membrane equation using a relatively small time step. The initial number of channels in each simulation trial was estimated after allowing the channels in each state to fluctuate around their steady-state resting values.

$$
\begin{cases}
\eta_0 = 0 & & & \\
\eta_1 = 3\alpha_m N_{m_0h_0} & (m_0h_0 \rightarrow m_1h_0) & \eta_{29} = 4\alpha_w N_{w_0z_0} & (w_0z_0 \rightarrow w_1z_0) \\
\eta_2 = \beta_m N_{m_1h_0} & (m_1h_0 \rightarrow m_0h_0) & \eta_{30} = \beta_w N_{w_1z_0} & (w_1z_0 \rightarrow w_0z_0) \\
\eta_3 = 2\alpha_m N_{m_1h_0} & (m_1h_0 \rightarrow m_2h_0) & \eta_{31} = 3\alpha_w N_{w_1z_0} & (w_1z_0 \rightarrow w_2z_0) \\
\eta_4 = 2\beta_m N_{m_2h_0} & (m_2h_0 \rightarrow m_1h_0) & \eta_{32} = 2\beta_w N_{w_2z_0} & (w_2z_0 \rightarrow w_1z_0) \\
\eta_5 = \alpha_m N_{m_2h_0} & (m_2h_0 \rightarrow m_3h_0) & \eta_{33} = 2\alpha_w N_{w_2z_0} & (w_2z_0 \rightarrow w_3z_0) \\
\eta_6 = 3\beta_m N_{m_3h_0} & (m_3h_0 \rightarrow m_2h_0) & \eta_{34} = 3\beta_w N_{w_3z_0} & (w_3z_0 \rightarrow w_2z_0) \\
\eta_7 = \alpha_h N_{m_0h_0} & (m_0h_0 \rightarrow m_0h_1) & \eta_{35} = \alpha_w N_{w_3z_0} & (w_3z_0 \rightarrow w_4z_0) \\
\eta_8 = \beta_h N_{m_0h_1} & (m_0h_1 \rightarrow m_0h_0) & \eta_{36} = 4\beta_w N_{w_4z_0} & (w_4z_0 \rightarrow w_3z_0) \\
\eta_9 = \alpha_h N_{m_1h_0} & (m_1h_0 \rightarrow m_1h_1) & \eta_{37} = \alpha_z N_{w_0z_0} & (w_0z_0 \rightarrow w_0z_1) \\
\eta_{10} = \beta_h N_{m_1h_1} & (m_1h_1 \rightarrow m_1h_0) & \eta_{38} = \beta_z N_{w_0z_1} & (w_0z_1 \rightarrow w_0z_0) \\
\eta_{11} = \alpha_h N_{m_2h_0} & (m_2h_0 \rightarrow m_2h_1) & \eta_{39} = \alpha_z N_{w_1z_0} & (w_1z_0 \rightarrow w_1z_1) \\
\eta_{12} = \beta_h N_{m_2h_1} & (m_2h_1 \rightarrow m_2h_0) & \eta_{40} = \beta_z N_{w_1z_1} & (w_1z_1 \rightarrow w_1z_0) \\
\eta_{13} = \alpha_h N_{m_3h_0} & (m_3h_0 \rightarrow m_3h_1) & \eta_{41} = \alpha_z N_{w_2z_0} & (w_2z_0 \rightarrow w_2z_1) \\
\eta_{14} = \beta_h N_{m_3h_1} & (m_3h_1 \rightarrow m_3h_0) & \eta_{42} = \beta_z N_{w_2z_1} & (w_2z_1 \rightarrow w_2z_0) \\
\eta_{15} = 3\alpha_m N_{m_0h_1} & (m_0h_1 \rightarrow m_1h_1) & \eta_{43} = \alpha_z N_{w_3z_0} & (w_3z_0 \rightarrow w_3z_1) \\
\eta_{16} = \beta_m N_{m_1h_1} & (m_1h_1 \rightarrow m_0h_1) & \eta_{44} = \beta_z N_{w_3z_1} & (w_3z_1 \rightarrow w_3z_0) \\
\eta_{17} = 2\alpha_m N_{m_1h_1} & (m_1h_1 \rightarrow m_2h_1) & \eta_{45} = \alpha_z N_{w_4z_0} & (w_4z_0 \rightarrow w_4z_1) \\
\eta_{18} = 2\beta_m N_{m_2h_1} & (m_2h_1 \rightarrow m_1h_1) & \eta_{46} = \beta_z N_{w_4z_1} & (w_4z_1 \rightarrow w_4z_0) \\
\eta_{19} = \alpha_m N_{m_2h_1} & (m_2h_1 \rightarrow m_3h_1) & \eta_{47} = 4\alpha_w N_{w_0z_1} & (w_0z_1 \rightarrow w_1z_1) \\
\eta_{20} = 3\beta_m N_{m_3h_1} & (m_3h_1 \rightarrow m_2h_1) & \eta_{48} = \beta_w N_{w_1z_1} & (w_1z_1 \rightarrow w_0z_1) \\
\eta_{21} = 4\alpha_n N_{n_0} & (n_0 \rightarrow n_1) & \eta_{49} = 3\alpha_w N_{w_1z_1} & (w_1z_1 \rightarrow w_2z_1) \\
\eta_{22} = \beta_n N_{n_1} & (n_1 \rightarrow n_0) & \eta_{50} = 2\beta_w N_{w_2z_1} & (w_2z_1 \rightarrow w_1z_1) \\
\eta_{23} = 3\alpha_n N_{n_1} & (n_1 \rightarrow n_2) & \eta_{51} = 2\alpha_w N_{w_2z_1} & (w_2z_1 \rightarrow w_3z_1) \\
\eta_{24} = 2\beta_n N_{n_2} & (n_2 \rightarrow n_1) & \eta_{52} = 3\beta_w N_{w_3z_1} & (w_3z_1 \rightarrow w_2z_1) \\
\eta_{25} = 2\alpha_n N_{n_2} & (n_2 \rightarrow n_3) & \eta_{53} = \alpha_w N_{w_3z_1} & (w_3z_1 \rightarrow w_4z_1) \\
\eta_{26} = 3\beta_n N_{n_3} & (n_3 \rightarrow n_2) & \eta_{54} = 4\beta_w N_{w_4z_1} & (w_4z_1 \rightarrow w_3z_1) \\
\eta_{27} = \alpha_n N_{n_3} & (n_3 \rightarrow n_4) & \eta_{55} = \alpha_r N_{r_0} & (r_0 \rightarrow r_1) \\
\eta_{28} = 4\beta_n N_{n_4} & (n_4 \rightarrow n_3) & \eta_{56} = \beta_r N_{r_1} & (r_1 \rightarrow r_0)
\end{cases}
\tag{4.42}
$$

Chapter 5

Single-Pulse Response

5.1 Overview

In this chapter and the next, the proposed model is evaluated. Most clinical cochlear implants use trains of amplitude-modulated charge-balanced biphasic pulses to stimulate the AN (Loizou, 1998; Bruce et al., 1999c; Shepherd and Javel, 1999; Clark, 2003; Rubinstein, 2004; Sly et al., 2007; Macherey et al., 2008). This chapter concentrates on single-pulse responses while the next chapter deals with pulse train responses. The standard pulse applied in this analysis is a symmetric-biphasic current pulse. Both leading phase polarities are examined. Because many of the animals studies and computational models utilize monophasic stimulation (Miller et al., 1999b,c, 2001b; Matsuoka et al., 2001; Mino et al., 2002, 2004), the response to monophasic pulses is also investigated and compared to that of biphasic pulse. Comparing monophasic and biphasic pulse responses was carried out by many CI groups such as Shepherd and Javel (1999), Miller et al. (2001b), and Rattay et al. (2001b,a).

Hyperpolarization-activated cation channels and low threshold potassium channels, which control the passage of the I_h and I_{KLT} respectively, are added systematically to the standard Hodgkin-Huxley model. As a result, four models evolve as follows: i) standard Hodgkin-Huxley model, *Model-I*; ii) I_h only added to the standard model, *Model-II*; iii) I_{KLT} only added to the standard model, *Model-III*; and iv) both I_h and I_{KLT} added to the standard model, *Model-IV*. An intracellular-injected[1] charge-balanced biphasic pulse of both leading phase polarities, at different pulse-widths and interphase gaps, is applied to the four models. A depolarizing monophasic pulse is utilized in the monophasic analysis.

[1]Intracellular injection means that the electrode is inserted inside the cell and penetrating the cell membrane. However, most of the physiological experiments that involve cochlear implants stimulation stimulate the nerve extracellularly. Accordingly, the polarity of stimulation is switched, that is, an intracellular depolarizing pulse is an extracellular hyperpolarizing pulse and vice vera.

5.2 Basic Stimulus Response

The effect of adding I_h and/or I_{KLT} to the standard Hodgkin-Huxley model on the membrane response is investigated. Single biphasic pulses of both leading phase polarities are injected into each of the four model versions, as shown in Fig. 5.1 (depolarizing-phase leading–left panels; and hyperpolarizing-phase leading–right panels). Two stimulus currents at the subthreshold (FE=20%) and suprathreshold (FE=80%) levels are utilized (Figs. 5.1A & B; and C & D, respectively). The pulse-width is maintained at 100 μs/phase. Due to the stochastic nature of the model which increases the uncertainty in the response, each curve is produced by averaging the relative membrane potential of 1000 repetitions of Monte-Carlo simulation. Traces of membrane potential in the subthreshold cases are

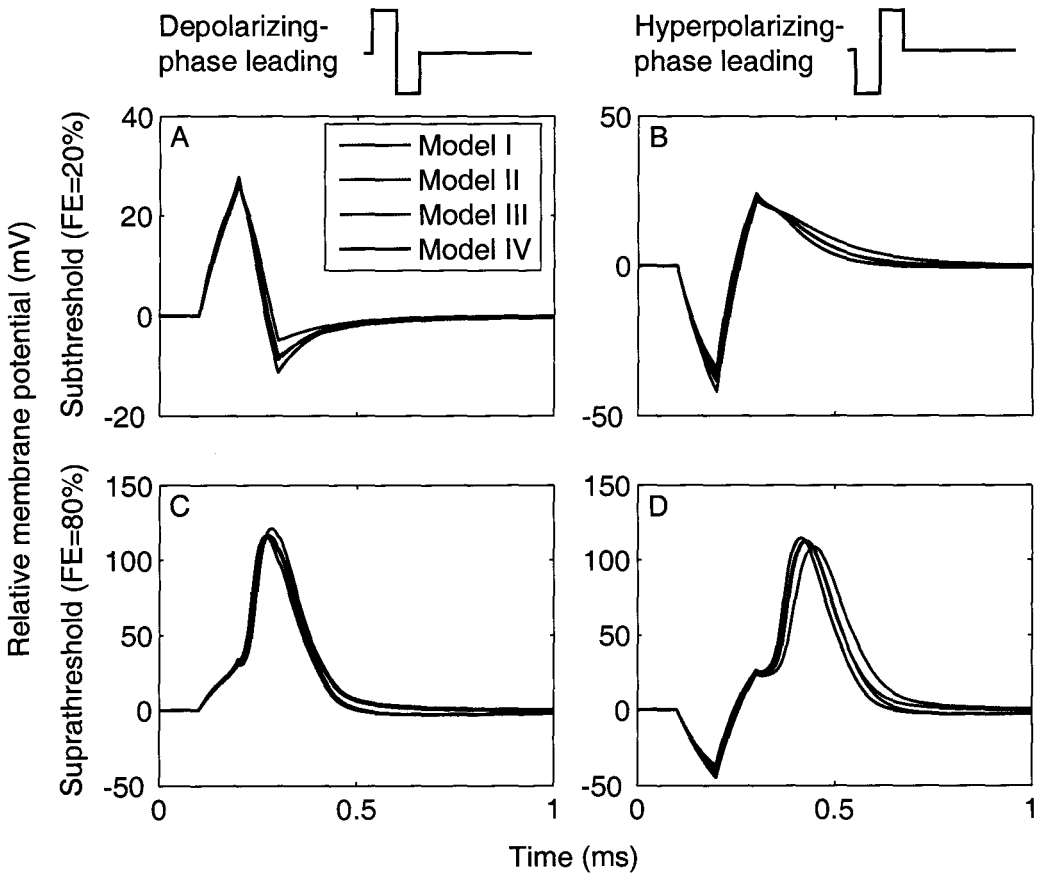

Figure 5.1: Responses of the four versions of the model to a single stimulus pulse (depolarizing-phase leading–left panels; and hyperpolarizing-phase leading–right panels). A and B shows the response to a subthreshold stimulus current (FE=20%). C and D shows the response to a suprathreshold stimulus current (FE=80%). Each curve is produced by averaging 1000 repetitions of Monte-Carlo simulation.

selected from trials in which no action potential occurs, while in the suprathreshold cases, only trials that elicit an action potential are selected.

In Fig. 5.1A, sodium channels are partially activated during the depolarizing phase, where their effect dominates causing the four versions to rise to almost the same level. During the hyperpolarizing phase, the membrane voltages of the four model versions show different hyperpolarizing levels before the end of the stimulating pulse, where Model-I has the lowest (−5.0 mV) while Model-IV has the highest (−11.4 mV). Because of the leading depolarization, the KLT channels have begun opening and the HCN channels have begun closing when the hyperpolarizing pulse arrives, producing an increased outward I_{KLT} and decreased inward I_h, respectively, both of which lead to a stronger hyperpolarization. The model is then injected by a hyperpolarizing-phase leading subthreshold stimulus, as shown in Fig. 5.1B. During the hyperpolarizing phase, Model-I produces the highest hyperpolarizing level (−41.94 mV). Model-II and Model-IV has lower hyperpolarizing levels (−36.22 mV and −34.03 mV, respectively) due to the activation of I_h and the deactivation of I_{KLT}, causing the membrane potential to sag back toward the resting potential.

The suprathreshold responses in Figs. 5.1C and D, Model-I has the longest latency at both leading phase polarities, whereas Model-IV exhibits the shortest latency. The membrane voltage during the hyperpolarizing-phase in Figs. 5.1B and D are similar. Model-III and Model-IV returns to the resting potential faster than the other two models because of the efflux of I_{KLT} and I_K that remain for some time after the removal of the stimulus.

Membrane potential waveforms of the four models in response to a single long anodic and cathodic monophasic current steps are shown in Figs. 5.2 and 5.3, respectively. In Fig. 5.2, a suprathreshold current at 33 pA and pulse-width of 150 ms is injected intracellularly. The standard Hodgkin-Huxley model, Model-I, (A) does not show the after-hyperpolarization phase of the action potential and sharply returns to zero relative membrane potential upon the termination of the stimulus current, (arrow head ▲). Although the original Hodgkin and Huxley (1952) equations successfully modelled the after-hyperpolarization phase, their model was based on an operating temperature of 6.3°C. Kinetics equations in this study are adjusted to 37.0°C. This huge increase in the operating temperature speeds up the gating kinetics substantially. Therefore, potassium channels return to rest very fast before the accumulation of the negative ions inside the membrane. B shows the addition of I_h only, Model-II. When the membrane is depolarized, the r gating particle shuts down, preventing the passage of the I_h. When the stimulus is removed, the membrane shows after-hyperpolarization (see arrow head ▲) as the r gates are still closed and take time to return to rest (see Fig. 4.2 on page 39), due to the slow kinetics of r. Hence, the membrane becomes more negative before it returns to the resting membrane potential.

Panel C of Fig. 5.2 shows the effect of adding I_{KLT} alone, Model-III. The effect of I_{KLT} is apparent in lowering the level at which the membrane potential is depolarized by the prolonged current pulse. This could be related to the rapid adaptation components, observed in murine spiral ganglion neurons (Mo et al., 2002). The small after-hyperpolarization (▲) is due to the slow inactivation z of I_{KLT}. Therefore, the I_{KLT} current continues to flow out

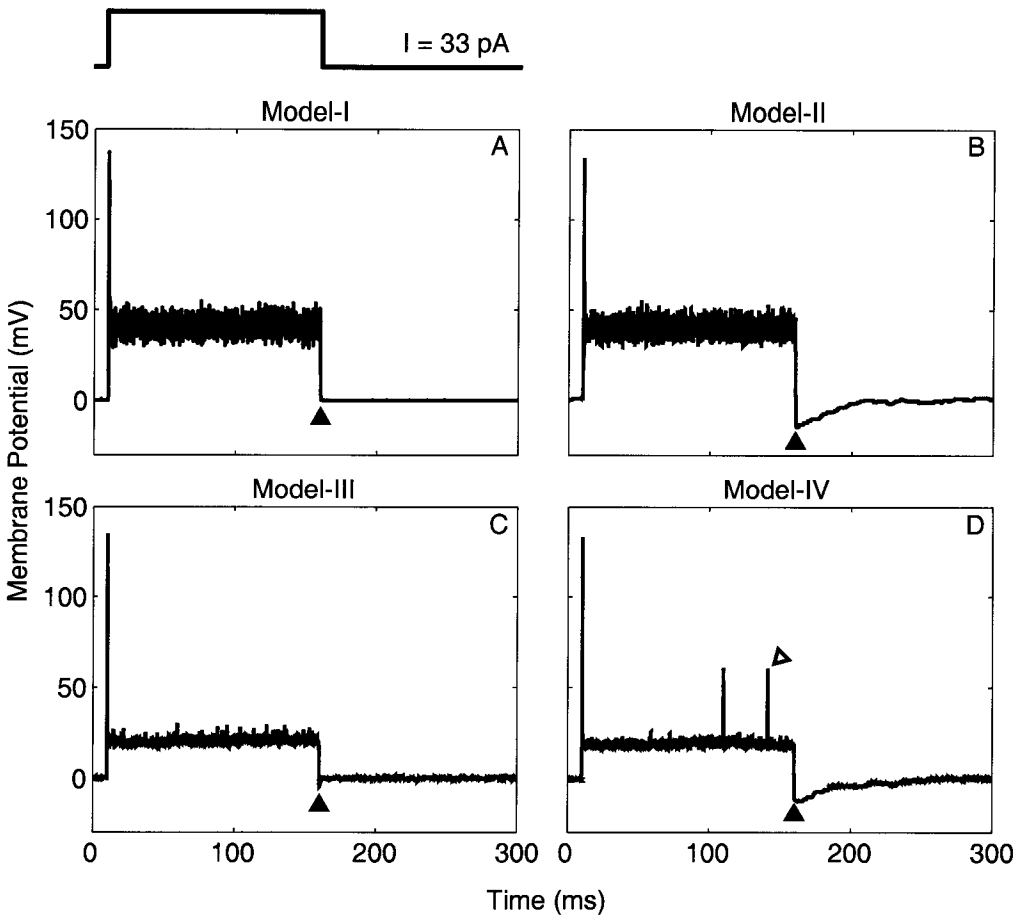

Figure 5.2: Examples of action potentials from different channel combination models in response to anodic monophasic current pulse. The standard Hodgkin-Huxley model, Model-II (A). Adding I_h alone, Model-I (B). Adding I_{KLT} alone, Model-III (C). Adding both, Model-IV (D). Pulse-width is 150 ms.

of the cell causing the membrane potential to be more negative (before the appearance of the effect of the inactivation component z). Finally, the action potential of the complete model that includes both I_h and I_{KLT}, Model-IV (D), has features that are seen in Model-II and Model-III such as the long after-hyperpolarization and lower sustained depolarized membrane potential, respectively. The two small spikes in D (arrow head $\triangle$) are not action potentials, but rather due to the stochastic activity of the sodium gating particles.

The models are then injected with a hyperpolarizing current pulse at -50 pA and pulse-width of 150 ms. Model-I and Model-III (Fig. 5.3 A and C, respectively) show similar responses. For these two models, all voltage-gated channels are closed and the displacement in the membrane voltage is only due to the injected and capacitance currents. On the other hand, when the I_h is included in Model-II (B) or Model-IV (D), a hyperpolarizing

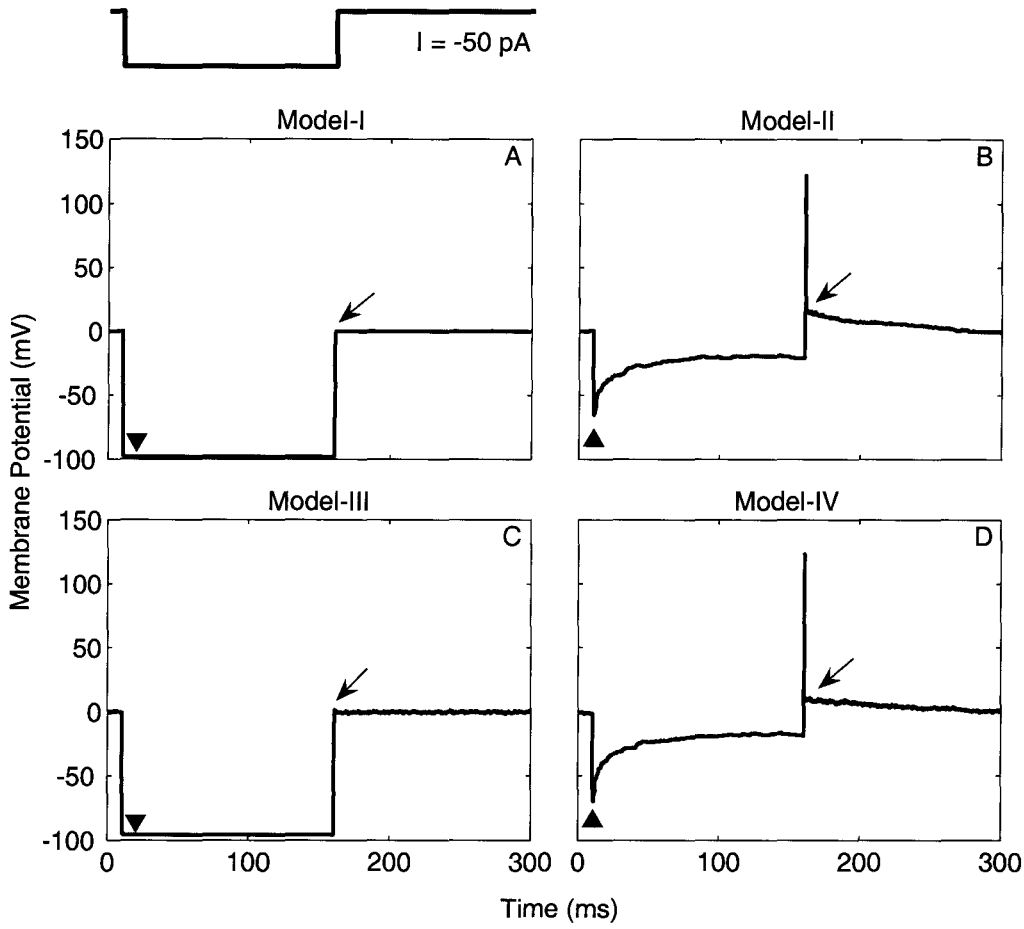

Figure 5.3: Examples of action potentials from different channel combination models in response to cathodic monophasic current pulse. The standard Hodgkin-Huxley model, Model-I (A). Adding I_h alone, Model-II (B). Adding I_{KLT} alone, Model-III (C). Adding both, Model-IV (D). Pulse-width is 150 ms.

current pulse causes the r particles to become fully open. Influx of positive ions force the membrane to depolarize faster resulting in a voltage sag (arrow head (▲), Fig. 5.3 B and D). Physiological studies have shown similar results (Chen, 1997; Mo and Davis, 1997b; Bal and Oertel, 2000; Rodrigues and Oertel, 2006). Moreover, upon the termination of the stimulus (↑), an action potential is generated in Model-II and Model-IV due to the presence of I_h, which is not the case for Model-I and Model-III. The long time required by this hyperpolarization-activated action potential to return to rest is due to the slow kinetics of the r particles which slow down the time required for the hyperpolarization-activated cation channels to return to its resting state.

5.3 Varying the Pulse-width

To evaluate the effect of varying the pulse-width of the stimulus pulse on the four models, each model is stimulated at pulse-widths of 100, 200, 300, 500 and 700 μs per phase. Three stimulation modes are used: i) depolarizing-phase leading biphasic pulse; ii) hyperpolarizing-phase leading biphasic pulse; and iii) anodic (depolarizing) monophasic pulse. Parameters such as firing efficiency, threshold, relative spread, mean latency, and jitter are measured. Threshold and relative spread were defined in § 3.2.1. The other parameters will be defined accordingly in the text. Simulation results values are listed in Appendix A.

The first parameter to investigate is the firing efficiency. *Firing efficiency* (FE) is defined as the probability of a nerve fiber to spike in response to a certain stimulus input. Verveen (1960) and Bruce et al. (1999c) showed that the relation governing the spiking probability and the stimulus level is well fit by an integrated-Gaussian function (sigmoidal function).

Fig. 5.4 shows FE as a function of stimulus current level, pulse-width (rows), and stimulation mode (columns). Each point is evaluated from 1000 repetitions of Monte-Carlo simulation (symbols). Data points are then fit by an integrated-Gaussian function (solid lines). The FE curves for the four models in all three stimulation cases shift to the left as pulse-width increases. This indicates a decrease in threshold level (threshold is the stimulus current level at 0.5 firing probability). The decrease in threshold is substantial when the pulse-width is changed from 100 μs to 200 μs per phase, whereas at longer pulse-widths the change is smaller.

Model-I and Model-IV have the lowest and highest thresholds, respectively, in all cases except at 100 μs per phase, biphasic, hyperpolarizing-phase leading stimulus (first row, middle panel), where the threshold of Model-I is higher than the other three models (see also Fig. 5.6A, filled symbols). In this particular case, the curves of Model-II, Model-III, and Model-IV overlap (i.e. they have equal thresholds). FE curves of the four models, when stimulated with the depolarizing-phase leading biphasic pulse (left column panels), show similar patterns to their corresponding responses of the anodic-monophasic pulse (right column panels), at the same pulse-width. For instance, Model-II has higher threshold than Model-III at shorter pulse-widths (left and right panels in the first and second rows), then thresholds of both models overlap at 500 μs per phase before the threshold of Model-III becomes higher at longer pulse-widthes. This observation is not seen in the case where the stimulus pulse is the hyperpolarizing-phase leading biphasic (bottom panel of middle column). A final remark about Fig. 5.4 is that the difference in threshold between Model-I and Model-IV is larger in the case of anodic-monophasic or depolarizing-phase leading biphasic stimulations than with hyperpolarizing-phase leading biphasic stimulation.

The relation between threshold and pulse-width is illustrated in Fig. 5.5A, B, and C for depolarizing-phase leading biphasic, hyperpolarizing-phase leading biphasic, and anodic-monophasic, respectively. Models I, II, III, and IV are represented by symbols $\circ, *, \times$, and $+$, respectively. Threshold decreases with increasing pulse-width, as noted

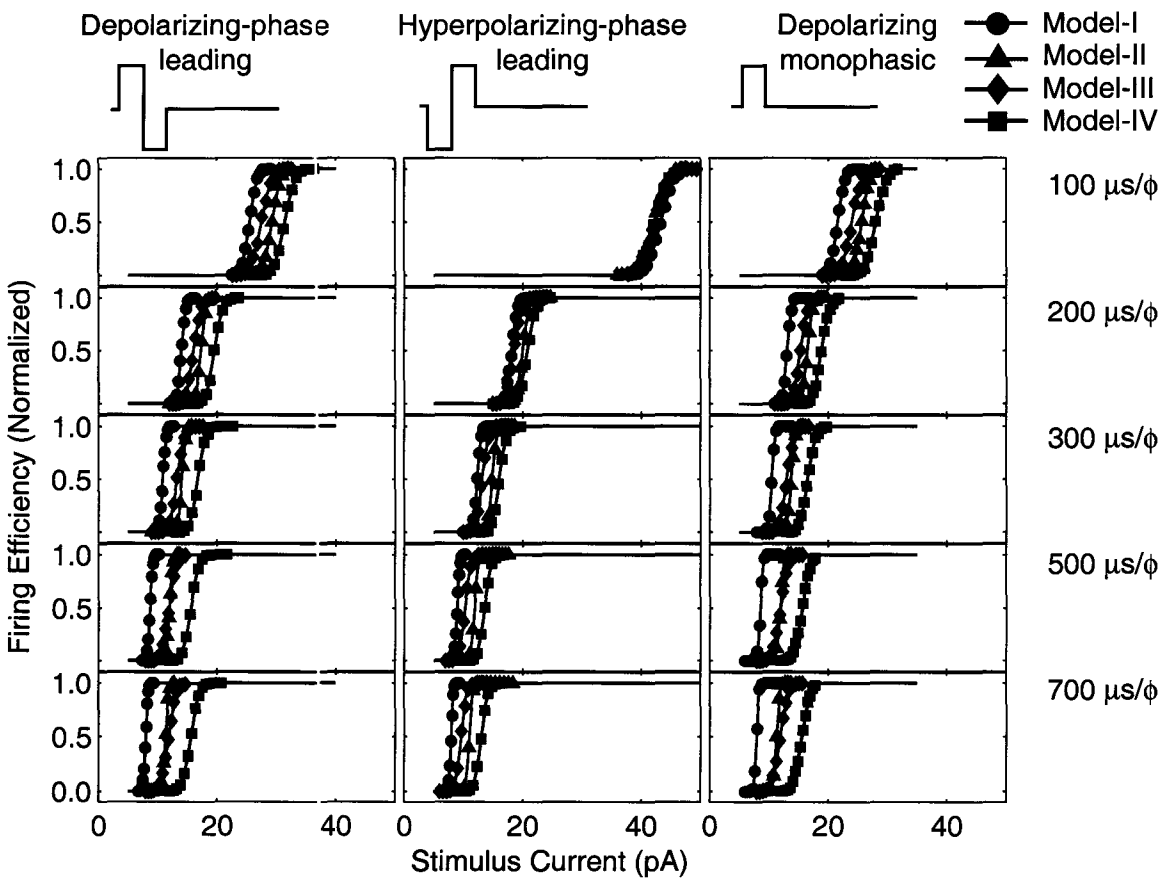

Figure 5.4: Firing efficiency curves as a function of stimulus currents pulses at different pulse-widths. Columns from left represent depolarizing-phase leading biphasic, hyperpolarizing-phase leading biphasic, and anodic monophasic stimulation modes. Rows from top show the response at different pulse-widths. Symbols •, ▲, ♦, and ■ represent Model-I, Model-II, Model-III, and Model-IV, respectively. Each point is obtained from 1000 repetitions of Monte-Carlo simulation. Solid lines are the integrated-Gaussian fits. Interphase gape for biphasic stimuli is zero μs.

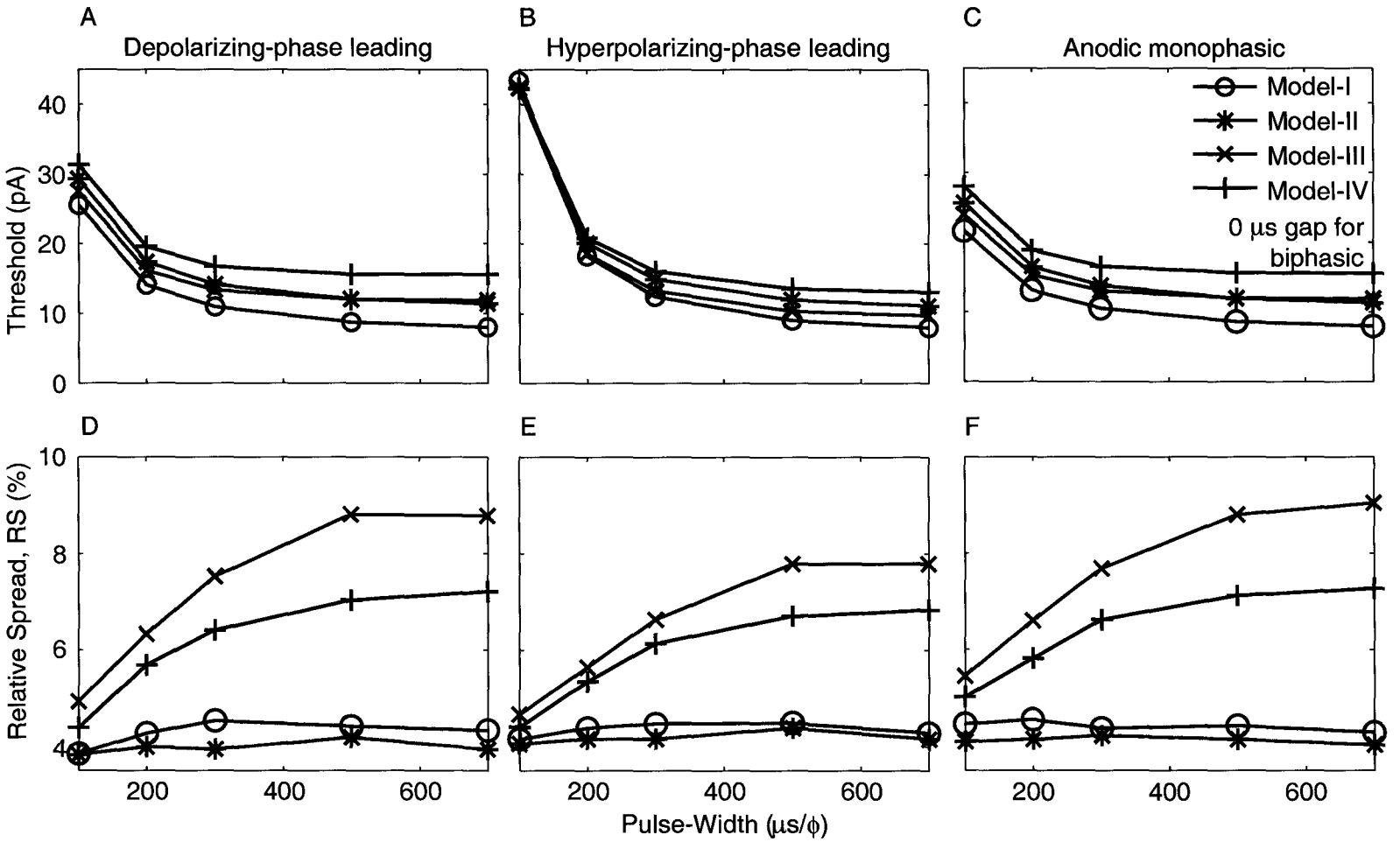

Figure 5.5: Threshold (upper row panels) and relative spread (lower row panels) as a function of pulse-width. Columns from left represent depolarizing-phase leading biphasic, hyperpolarizing-phase leading biphasic, and anodic monophasic stimulation modes. Symbols $\circ, *, \times$, and $+$ represent Model-I, Model-II, Model-III, and Model-IV, respectively. For biphasic stimulation, the interphase gap is zero μs.

above. However, threshold reaches an asymptotic value at longer pulse-widths. This is the minimum threshold that a model can reach regardless of the size of the stimulus pulse-width.

At shorter pulse-widths, depolarizing-phase leading biphasic stimulation has lower threshold than hyperpolarizing-phase leading biphasic stimulation (Fig.5.6A, filled symbols) but higher than threshold level of anodic-monophasic stimulation (Fig.5.7A, filled symbols). On the other hand, at longer pulse-widths, reversing the leading phase polarities or using an anodic monophasic pulse does not affect the threshold for each of the four models (i.e. each model exhibits similar thresholds regardless of the stimulation mode)—see Fig.5.6A, open symbols and Fig.5.7A, open symbols.

Relative spread (RS) as a function of pulse-width phase duration is shown in Fig. 5.5D, E, and F for depolarizing-phase leading biphasic, hyperpolarizing-phase leading biphasic, and anodic-monophasic, respectively. RS is the standard deviation of the integrated-Gaussian function normalized to threshold level and is used as a measure for the relative noise in threshold fluctuations. Model-I and Model-II exhibit no change in RS with pulse width. In contrast, in Model-III, the membrane noise increases substantially, especially with longer pulse-widths. The same effect is seen with Model-IV, however it is less than that of Model-III. The logarithmic increase in RS reaches an asymptotic value at longer pulse-widths. Reversing the leading phase polarities has minor effects on RS except for Model-III and Model-IV, where the RS in response to a depolarizing-phase leading becomes higher at longer pulse-widths (Fig. 5.6B). RS of anodic-monophasic stimulation is less than that of depolarizing-phase leading biphasic stimulation for shorter pulse-widths while RS is similar for longer pulse-widths(Fig. 5.7B).

The temporal properties of an action potential are quantified by the mean latency and jitter. Latency (LT) is the mean time for a spike to occur after applying a stimulus, while jitter (JT) is the standard deviation of spike occurrence times. Fig. 5.8A shows latency as a function of leading phase polarity. At 100 μs per phase pulse-width, the change in spike LT is very small between the different models (filled symbols), which is not the case for longer pulse-width (open symbols). Generally, Model-I has the longest LT while Model-IV has the shortest. Hyperpolarizing-phase leading-stimulation has longer LT than depolarizing-phase leading and anodic-monophasic. In Fig. 5.9A, LTs of depolarizing-phase leading biphasic and monophasic stimulation are compared, where not much difference in LT is observed (filled and open symbols).

Jitter of Model-II is higher than other models except for hyperpolarizing-phase leading and anodic-monophasic at 100 μs per phase where jitter of Model-I is higher (Fig. 5.8B and 5.9B). Depolarizing-phase leading JT is lower than anodic-monophasic and hyperpolarizing-phase leading biphasic JT for shorter pulse-widths but has close values at longer pulse-width.

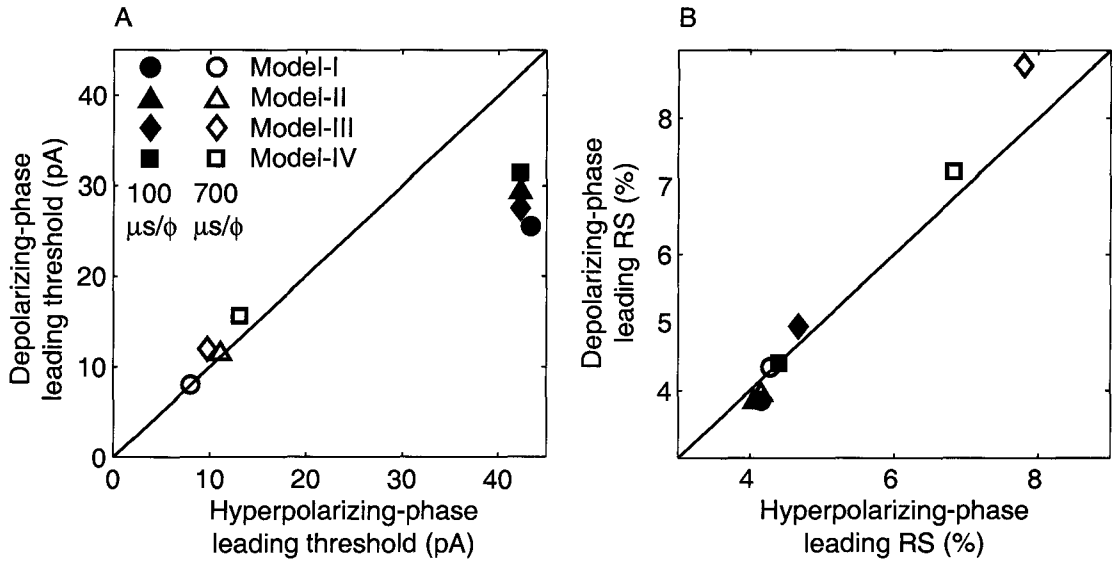

Figure 5.6: Summary plots showing threshold (A) and relative spread (B) as a function of leading phase polarities for four different channel combinations (see legend). Filled and open symbols represent pulse-widths at 100 μs and 700 μs per phase, respectively. Interphase gap is zero μs.

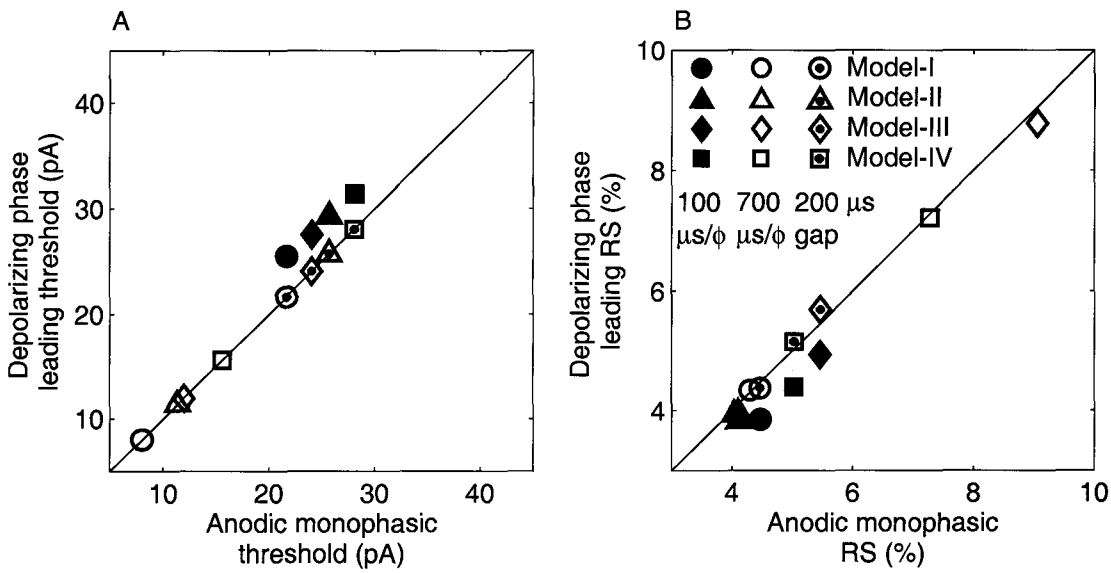

Figure 5.7: Summary plots showing threshold (A) and relative spread (B) as a function of depolarizing-phase leading biphasic and anodic monophasic current pulses for four different channel combinations (see legend). Filled and open symbols represent pulse-widths at 100 μs and 700 μs per phase, respectively, and interphase gap of zero μs for biphasic. Dotted open symbols represent depolarizing-phase leading and anodic monophasic pulse-width at 100 μs per phase and interphase gap at 200 μs for biphasic.

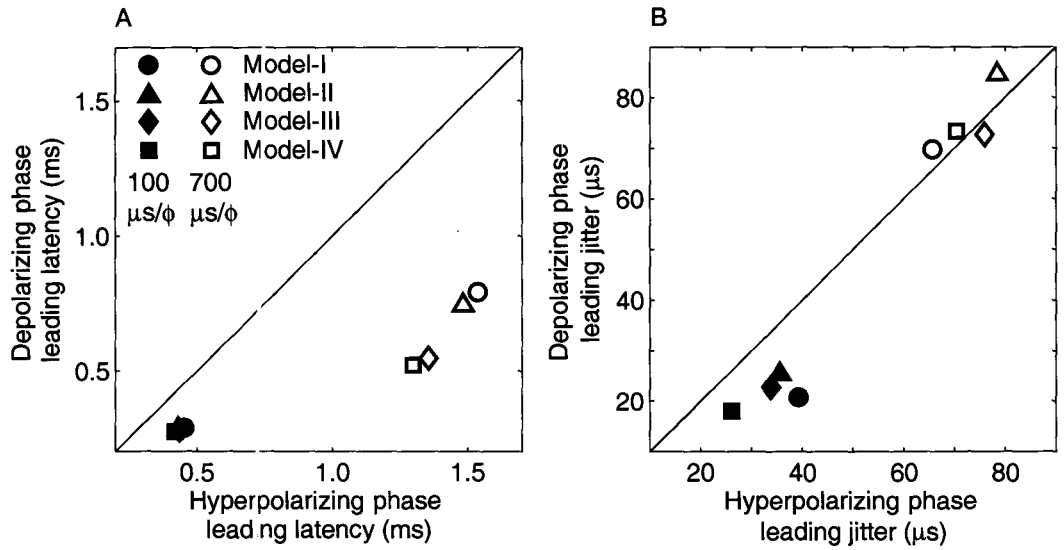

Figure 5.8: Summary plots showing latency (A) and jitter (B) at FE 50% as a function of leading phase polarities for four different channel combinations (see legend). Filled and open symbols represent pulse-widths at 100 µs and 700 µs per phase, respectively. Interphase gap is zero µs.

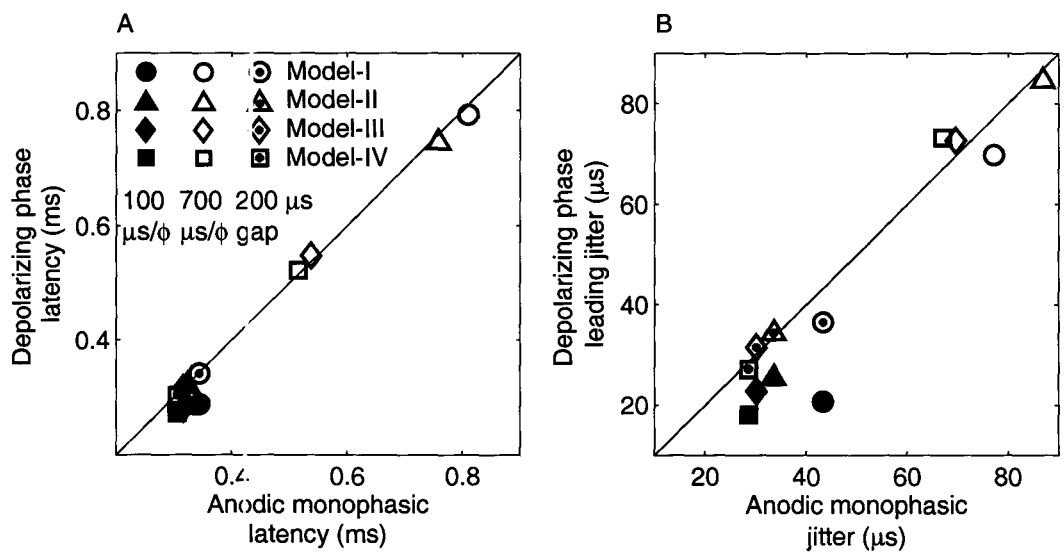

Figure 5.9: Summary plots showing latency (A) and jitter (B) at FE 50% as a function of depolarizing-phase leading biphasic and anodic monophasic current pulses for four different channel combinations (see legend). Filled and open symbols represent pulse-widths at 100 µs and 700 µs per phase, respectively, and interphase gap of zero µs for biphasic. Dotted open symbols represent depolarizing-phase leading and anodic monophasic pulse-widths at 100 µs per phase and interphase gap at 200 µs for biphasic.

5.4 Varying the Interphase Gap

Responses of the four models to interphase gaps of 0, 20, 40, 80, 130, and 200 μs are evaluated. Pulse-width is fixed at 100 μs per phase. Depolarizing- and hyperpolarizing-phase leading biphasic pulses are used. Simulation result values are listed in Appendix A.

Firing efficiency curves are shown in Fig. 5.10. Rows show the response at different interphase gaps. Left and right columns show the response to depolarizing-phase leading and hyperpolarizing-phase leading pulses, respectively. As in Fig. 5.4, each point is evaluated from 1000 repetitions of Monte-Carlo simulation (symbols). Data sets are fit by integrated-Gaussian function (solid lines).

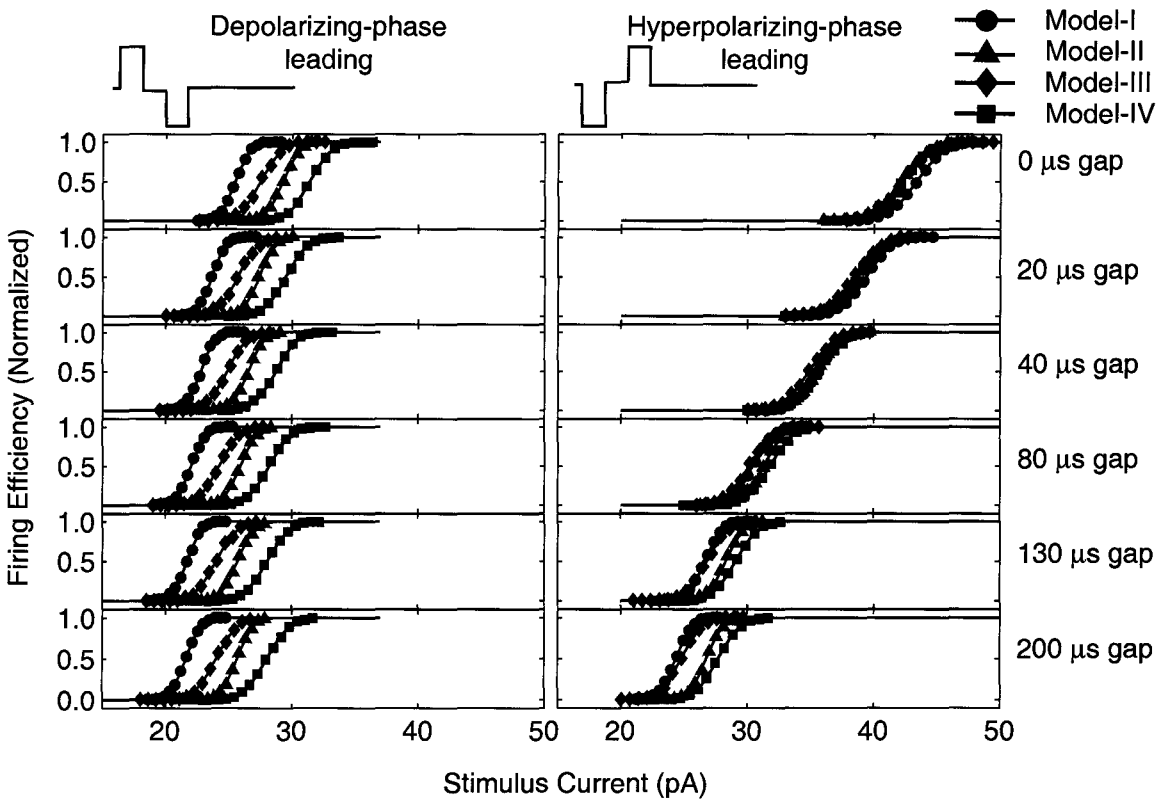

Figure 5.10: Firing efficiency curves as a function of stimulus currents pulses at different interphase gaps. Columns from left represent depolarizing-phase leading biphasic and hyperpolarizing-phase leading biphasic stimulation modes. Rows from top show the response at different interphase gaps. Symbols •, ▲, ♦, and ■ represent Model-I, Model-II, Model-III, and Model-IV, respectively. Each point is obtained from 1000 repetitions of Monte-Carlo simulation. Solid lines are the integrated-Gaussian fits.

Increasing the interphase gap with depolarizing-phase leading stimulation has minimum effect on the general shape of the FE curves (Fig. 5.10, left column), and the decrease in threshold is relatively small ($\backsimeq$ 3 pA)—see Fig.5.11A. However, Model-IV has the highest threshold level and Model-I has the lowest. In the case of hyperpolarizing-phase leading stimulation (Fig. 5.10, right column), the threshold level decreases substantially at longer interphase-gaps ($\backsimeq$ 18 pA decrease)—see Fig.5.11B. At 200 μs gap width, threshold levels of depolarizing-phase leading biphasic stimulation become similar to those of hyperpolarizing-phase leading biphasic (Fig. 5.12A, open symbols) and anodic-monophasic (Fig. 5.7A, dotted-open symbols) in most of the cases.

Model-III and Model-IV show an increase in RS when increasing the interphase gap (Fig.5.11C and D). However, this increase is less than when varying the pulse-width. RS of the depolarizing-phase leading stimulation is relatively equal to RS of the opposite polarity at longer interphase gaps (Fig.5.12B, open symbols). Moreover, depolarizing-phase leading RS is similar to that of anodic-monophasic (Fig. 5.7B, dotted-open symbols).

Latencies of depolarizing-phase leading stimuli are shorter than hyperpolarizing-phase leading stimuli at longer interphase gaps (Fig. 5.13A, open symbols). When compared to anodic-monophasic, mean LTs are similar (Fig. 5.9A, open dotted symbols). Furthermore, whether the stimulus is anodic-monophasic or depolarizing-phase leading biphasic, the change in LT value is small, regardless of the size of the gap. Model-II, Model-III, and Model-IV have depolarizing-phase leading JTs equal to anodic-monophasic JTs (Fig. 5.9B, open dotted symbols).

5.5 Discussion

In this chapter, results of single pulse response were presented. Both I_h and I_{KLT} do have effects on action potential generation. I_h is an hyperpolarization-activated cation inward current which tends to depolarize the membrane when the membrane is below resting potential. On the other hand, I_{KLT} is activated when the membrane is depolarized, forming an outward current which speeds up the membrane repolarization after an action potential. The standard Hodgkin-Huxley model used in this study was limited in describing some of the firing properties observed during the ANFs stimulation. These properties include after-hyperpolarization phase of AP, anode-break excitation, and inward rectification that follows a hyperpolarizing stimulus. Although, the original Hodgkin-Huxley equations can model the first two phenomena, yet they are absent in the Hodgkin-Huxley model used here. One possibility could be due to the very fast kinetics of Na^+ and K^+ gates at mammalian body temperature. When I_h or/and I_{KLT} was added to the standard Hodgkin-Huxley model, the after-hyperpolarization appeared. I_h also showed a 'sag' in membrane voltage when the membrane was injected with a hyperpolarizing current pulse consistent with physiological data in Mo and Davis (1997b) and Chen (1997). Furthermore, I_{KLT} lowers the sustained depolarized level of the action potential when injected with a depolarizing current which

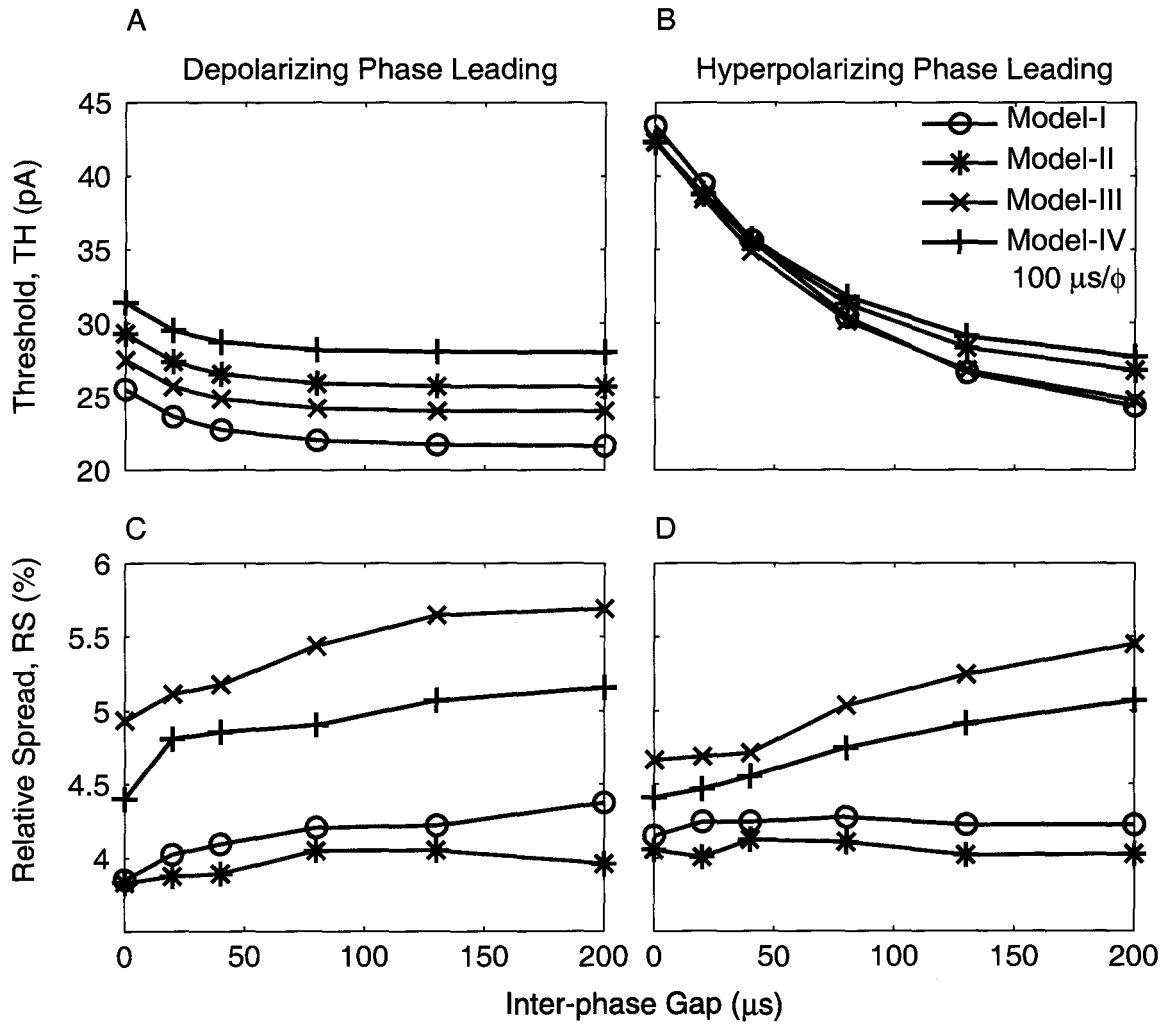

Figure 5.11: Threshold (upper row panels) and relative spread (lower row panels) as a function of interphase gap. Columns from left represent depolarizing-phase leading biphasic and hyperpolarizing-phase leading biphasic stimulation modes. Symbols $\circ, *, \times$, and $+$ represent Model-I, Model-II, Model-III, and Model-IV, respectively. The pulse-width is 100 μs.

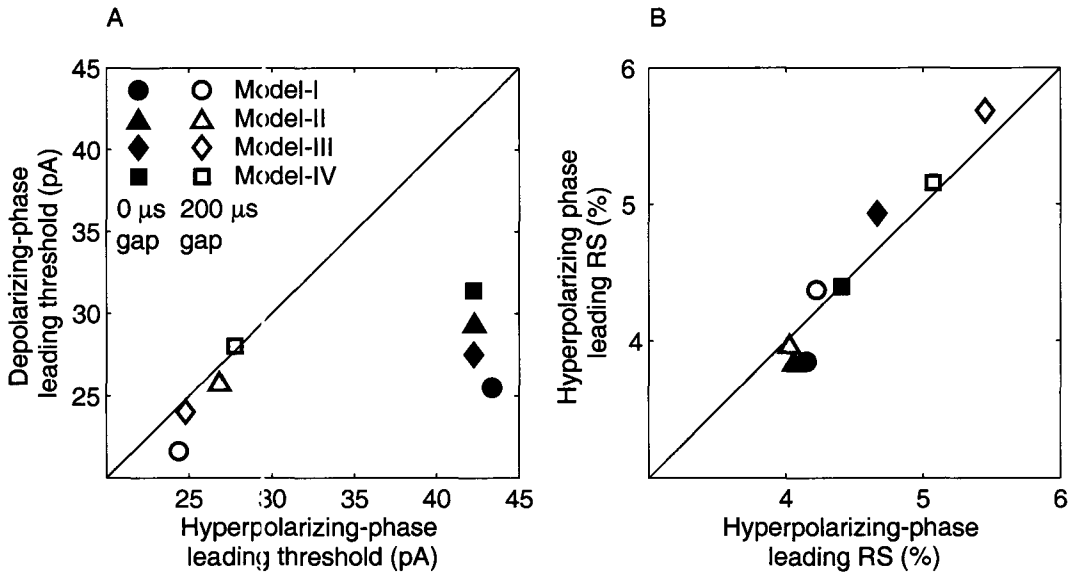

Figure 5.12: Summary plots showing threshold (A) and relative spread (B) as a function of leading phase polarities for four different channel combinations (see legend). Filled and open symbols represent interphase gaps at zero µs and 200 µs, respectively. For all stimulations, pulse-width is 100 µs per phase.

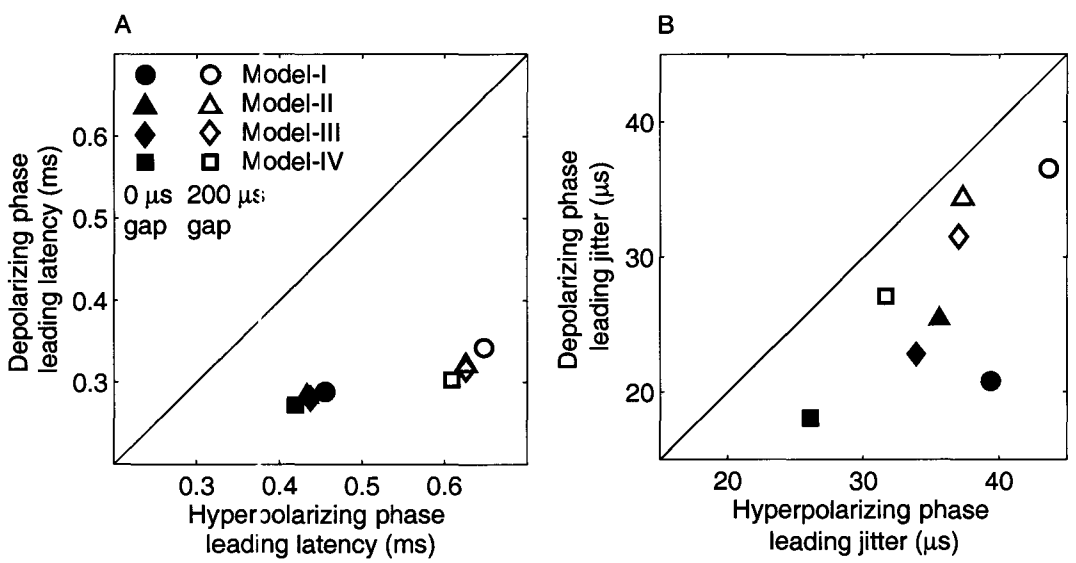

Figure 5.13: Summary plots showing latency (A) and jitter (B) at FE 50% as a function of leading phase polarities for four different channel combinations (see legend). Filled and open symbols represent interphase gaps at zero µs and 200 µs, respectively. For all stimulations, pulse-width is 100 µs per phase.

could be a sign of rapid adaptation seen in spiral ganglion neurons (Mo et al., 2002).

It is noteworthy to mention that the very slow kinetics of I_h makes the transition of the gating particles from one state to another unlikely when a single short stimulating pulse is used. Therefore, I_h tends to be stationary around its resting value for short pulse-widths. However, at resting membrane potential the gating particles are partially active and an inward current is formed. The relatively fast-activation particles w and very-slow-incomplete inactivation gating particles z helps I_{KLT} to be fully active when stimulated with short stimulus pulses.

Adding both currents to the standard Hodgkin-Huxley model elevated the threshold level more than that of the Hodgkin-Huxley model alone. Including either I_h or I_{KLT} increased the threshold too in most cases, but less than when both currents were included simultaneously. Thus, the effects of I_h and I_{KLT} on threshold are additive. Threshold is inversely proportional to pulse-width duration. All four current combinations showed higher thresholds for biphasic stimulation than with monophasic stimulation, consistent with Shepherd et al. (1999) and Miller et al. (2001b). Threshold with depolarizing-phase leading stimulus is lower than with hyperpolarizing-phase leading.

When adding I_{KLT} alone or with I_h, relative spread showed an increase with increasing the pulse-width (a relation which is absent in the standard Hodgkin-Huxley model alone). This result is consistent with physiological data of Bruce et al. (1999c), in which cat ANFs stimulated by a cochlear implant were found to have an increasing RS with increasing pulse-width. I_{KLT} appears to be responsible for adding membrane noise to the threshold fluctuations that are primarily due to stochastic Na^+, channel activation.

Latency produced by hyperpolarizing-phase leading pulses was longer than depolarizing-phase leading pulses. However, physiological data have shown an opposite result, which is more likely attributed to the change in site of initiation of action potential (Shepherd et al., 1999). This discrepancy may be due to limitations of the model used here as the model only simulates responses at a single node of Ranvier and ignores neighboring regions, forcing the model to be sensitive to the depolarizing-phases only. Extending the model to an axonal model (having several nodes of Ranvier) is necessary to describe spatial effects.

When the interphase gap is increased, the properties of the biphasic stimulations approach those of monophasic, similar to the results of Shepherd et al. (1999).

Chapter 6

Pulse-Train Response

6.1 Overview

Single-pulse analysis described in chapter 5 is extended further to evaluate responses to pulse trains. Clinical cochlear implants use amplitude-modulated biphasic pulse trains to stimulate the auditory nerve. Litvak et al. (2001), Zhang et al. (2007), and Miller et al. (2008), have shown that spike rate adaptation is positively correlated to pulse rate. Also, it has been suggested that increasing the stimulus pulse rate may improve the temporal response of ANF to electrical stimulation by desynchronizing the nerve response, imitating the randomness observed in the response of normal ears (Rubinstein et al., 1999; Litvak et al., 2001; Zhang et al., 2007; Miller et al., 2008).

The main objective of this chapter is assess the validity of adding I_{h} and/or I_{KLT} to the standard Hodgkin-Huxley model to explain spike rate adaptation observed in CI stimulation experiments. To do so, the four ANF models (Model-I, Model-II, Model-III, Model-IV; — defined in § 5.1) are stimulated using pulse trains of depolarizing-phase leading biphasic stimuli at rates (200, 800, and 2000 pulse/s) similar to those used in clinical cochlear implants (Zhang et al., 2007). Stimulus levels are expressed in terms of firing efficiency to the first pulse. For every pulse rate at each stimulus level, poststimulus time (PSTH) and interspike-interval (ISI) histograms are measured. Spike rate adaptation effects are evaluated using methods described in Zhang et al. (2007).

6.2 Poststimulus-Time Histogram

Poststimulus-time histograms (PSTHs) of pulse-train responses are shown in Fig. 6.1 on page 70 and 71. Simulated PSTHs (Figs. 6.1B, 6.1C, and 6.1D) are compared to PSTHs of a cat ANFs stimulations (Fig. 6.1A) described in Zhang et al. (2007). To facilitate comparison, the method defined in Zhang et al. (2007) to quantify for adaptation is followed. Two categories of bin widths are utilized: i) a "narrow-bin" width of 1 ms (vertical bars);

and ii) a group of eight non-overlapping "wide-bin" windows. These windows are 0-4, 4-12, 12-24, 24-36, 36-48, 48-100, 100-200, and 200-300 ms after pulse-train onset and are specified by their midpoints (unfilled symbols). The reason for choosing two bin sizes is that the narrow-bin may not accurately differentiate between adaptation and desynchronization that may occur in the nerve response, while the wide-bins can show the trend of spike rate behavior over a long period of time.

Figs. 6.1B, 6.1C, and 6.1D display PSTHs at three different current levels denoted in terms of firing efficiency to the first pulse (FE 0.2, 0.5, and 0.8, respectively). Histograms calculations are based on 100 Monte-Carlo simulation trials. In all three figures, responses to stimulus pulse rates of 200, 800, and 2000 pulse/s are explored (columns) for each individual model type (rows, from top: Model-I, Model-II, Model-III, and Model-IV). Fig. 6.1A from Zhang et al. (2007) shows the responses to stimulus pulse rates at 250, 1000, 5000, and 10000 pulse/s (columns) for three stimulus levels (rows). The stimulus levels used in Zhang et al. (2007) span a range that produces low firing probability (20-40%) to the first pulse to a maximal response rate over the final 100 ms (Zhang et al., 2007).

In ANFs of cats, spike rate adaptation increases with pulse rate (Litvak et al., 2001; Zhang et al., 2007) as shown in Fig. 6.1A. Care should be taken while interpreting this figure, as adaptation, refractoriness, and the low firing probabilities have combined effects in suppressing the spike rate (Miller et al., 2008). Increasing the stimulus level will increase the firing probability and may overcome the refractory effect, which is apparent in the second and third rows in Fig. 6.1A, leading to a dominant adaptation effect. In their analysis, Zhang et al. (2007) quantified two adaptation components based on the time constants of the wide-bin histograms: i) rapid, which appears directly after the onset of the stimulus (0-12 ms); and ii) short-term components, which may last for several milliseconds after pulse train onset. Each row in Fig. 6.1A is compared to its nearest corresponding stimulus level in Figs. 6.1B, 6.1C, and 6.1D.

Model-I across all stimulus levels and pulse rates does not show any signs of adaptation. This is emphasized by the nearly flat wide-bin curves (in contrast to the exponential decay seen in Fig. 6.1A). The drop in spike rate seen directly after the onset during the 2000 pulse/s may mistakenly be interpreted as adaptation. However, this drop is due to refractoriness rather than spike rate adaptation. Looking at the three stimulus level cases of Model-I at 2000 pulse/s, the spike rate increases with increasing stimulus level (i.e., the spike rate is dependent on the stimulus level) which indicates reduction in refractory effects and increase in firing probability.

In contrast to Model-I, Model-II shows strong rapid and short-term adaptations in all cases. Even at the lower stimulus rate (200 pulse/s), adaptation is evident, especially at higher stimulus levels (left panels, second row of Figs. 6.1C, and 6.1D). One more evidence of adaptation in Model-II is the decrease in the wide-bin exponential decay time constants with stimulus rate, which is similar to Fig. 6.1A).

Model-III shows rapid adaptation rather than short-term adaptation as indicated by the drop in spike rate directly after stimulus onset. This effect gets more apparent at higher

pulse rates. Mo et al. (2002) have shown in an earlier study that low-threshold potassium channels may be responsible for rapid adaptation. Again, refractory effects can not be avoided, however, the drop in response rate is somewhat independent of stimulus level. Not surprisingly, Model-IV has a combined behavior of Model-II and Model-III. Adaptation effects in Model-IV are qualitatively close to physiological data.

6.3 Inter-spike Intervals Histogram

Inter-spike interval (ISI) histograms (Fig. 6.2 on page 72 and 73) are evaluated to asses the variations in the temporal responses. Fig. 6.2A shows ISI histograms obtained from cats ANF stimulation experiments, carried out by Miller et al. (2008). The analyses conducted in Miller et al. (2008) were based on the data obtained from Zhang et al. (2007). Similar to Fig. 6.1A, Fig. 6.2A shows ISI histograms from one fiber stimulated at 250, 1000, and 5000 pulse/s pulse trains (columns) and at four different stimulus levels (rows). Stimulus levels span a range that produced low firing probability (20-40%) to the first pulse to maximal (saturated) response rate over the final 100 ms epoch of the stimulus train (Miller et al., 2008). For each stimulation condition (pulse rate and stimulus level), the histograms are divided into three analysis time windows (0-12, 4-50, 200-300 ms). ISI within each window are computed separately to avoid biasing towards low values (Miller et al., 2008). Simulation results reported here are investigated using the same analysis methodology described in Miller et al. (2008) to facilitate comparison. Each column in Figs. 6.2 B, 6.2 C, and 6.2D represents the responses to 200, 800, and 2000 pulse/s stimulus rates (left, middle, and right, respectively). Figs. 6.2B, 6.2C, and 6.2D show the responses to stimulus levels producing FEs of 0.2, 0.5, and 0.8 to the first pulse, respectively.

Consistent with Fig. 6.2A, the centroids of the ISI histograms in Figs. 6.2B, 6.2C, and 6.2D shift toward shorter intervals with increasing stimulus level. In most cases, Model-I shows substantial increase in the number of intervals, specially in the 200-300 ms epoch ("steady-state" as defined in Miller et al. (2008)), with respect to the other models. This may indicate the lack of short-term adaptation. At the 200 pulse/s pulse rate, the ISI are locked at the pulse period (5 ms) and its multiples, where the effect of refractoriness is minimum. On the other hand, the 800 and 2000 pulse/s pulse rate responses are affected by the refractory periods (0.5-1 ms). In Fig. 6.2D, ISIs of Models-II, III, and IV exhibit more spread than that in Model-I at higher pulse rates, which is comparable to Fig. 6.2A.

Figure 6.1: PSTH from the response of Models-I,II,III, and IV (rows) at stimulus pulse rates of 200, 800, and 2000 pulse/s (columns). B, C, and D represent stimulus levels at 0.2, 0.5, and 0.8 firing probability to the first pulse. Thin vertical bars represent histograms based on 1 ms bins, while open symbols represents wider bins. Histograms are obtained from 100 simulation trials. A is obtained from Zhang et al. (2007, Fig. 2, p. 360). (continued on page 70 and 71 ↪)

Figure 6.0: Continued

A Zhang et al. (2007, Fig. 2, p. 360)

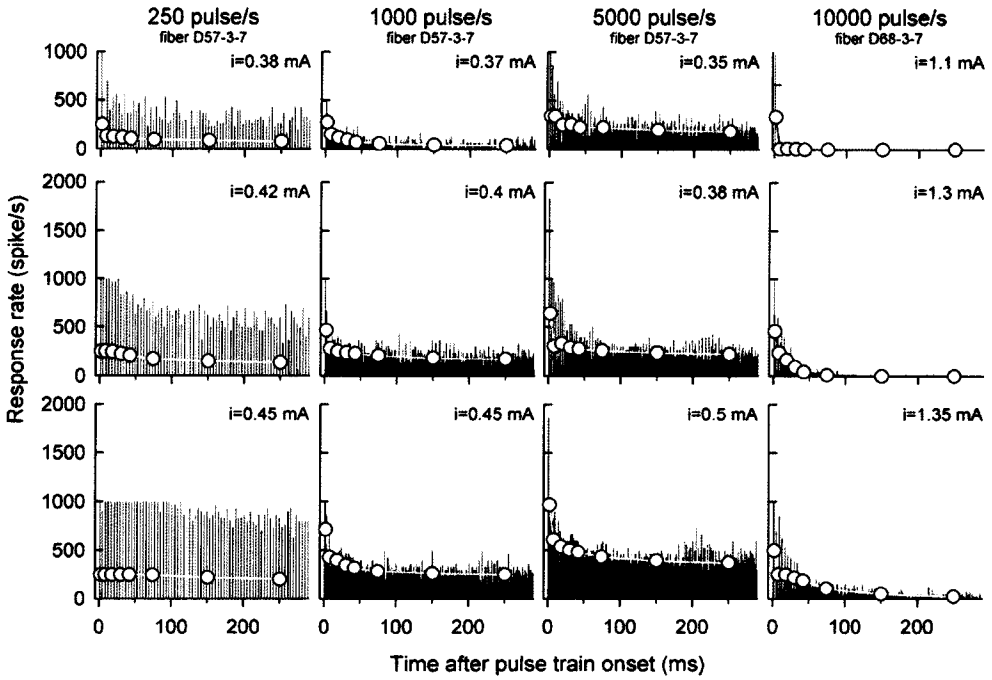

B

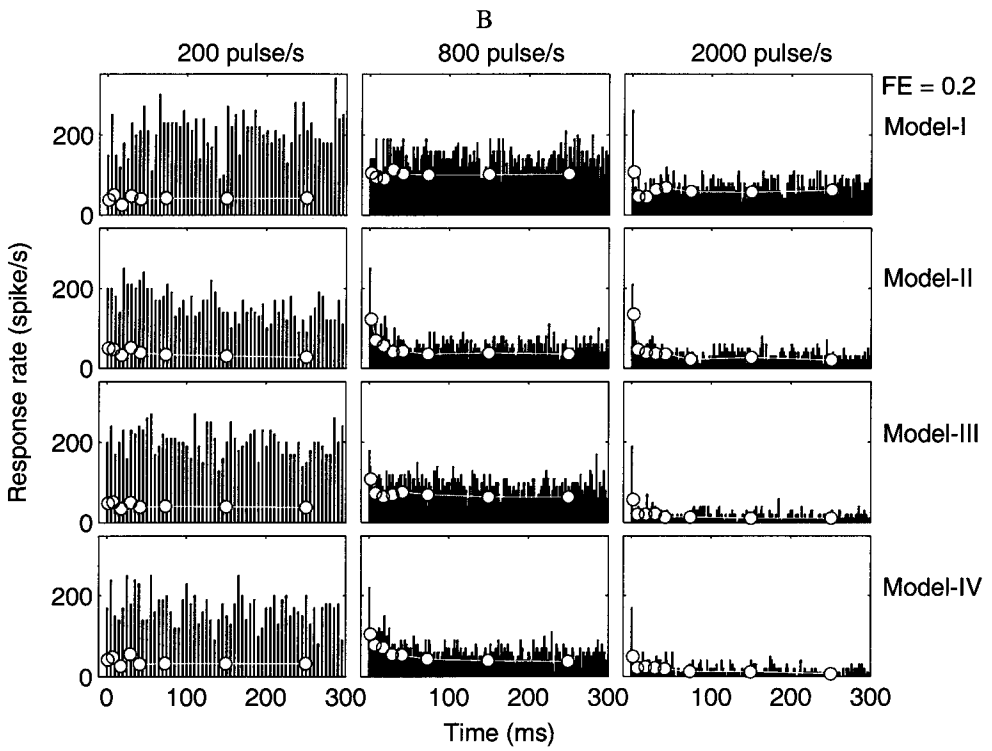

Figure 6.0: Continued

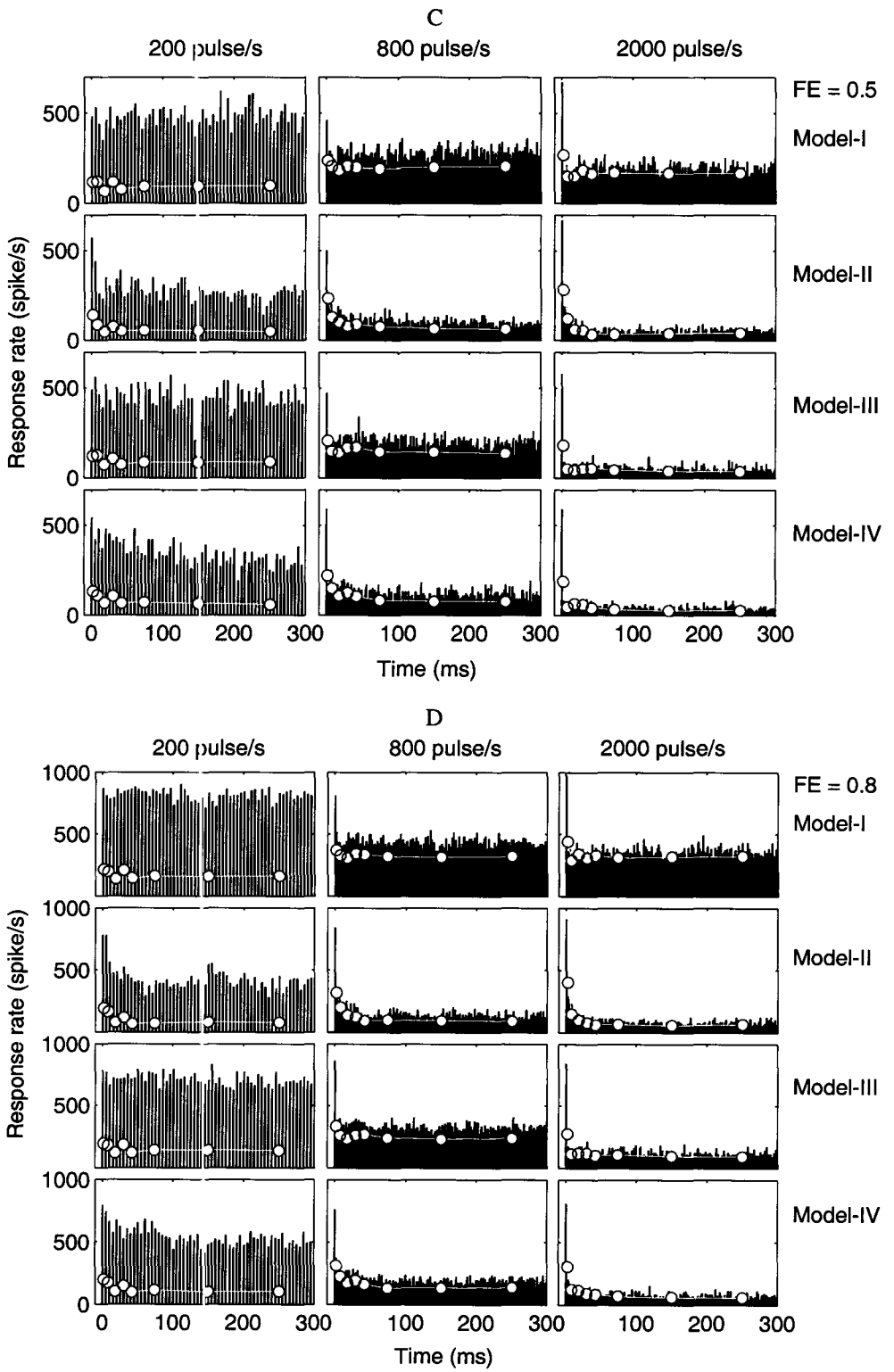

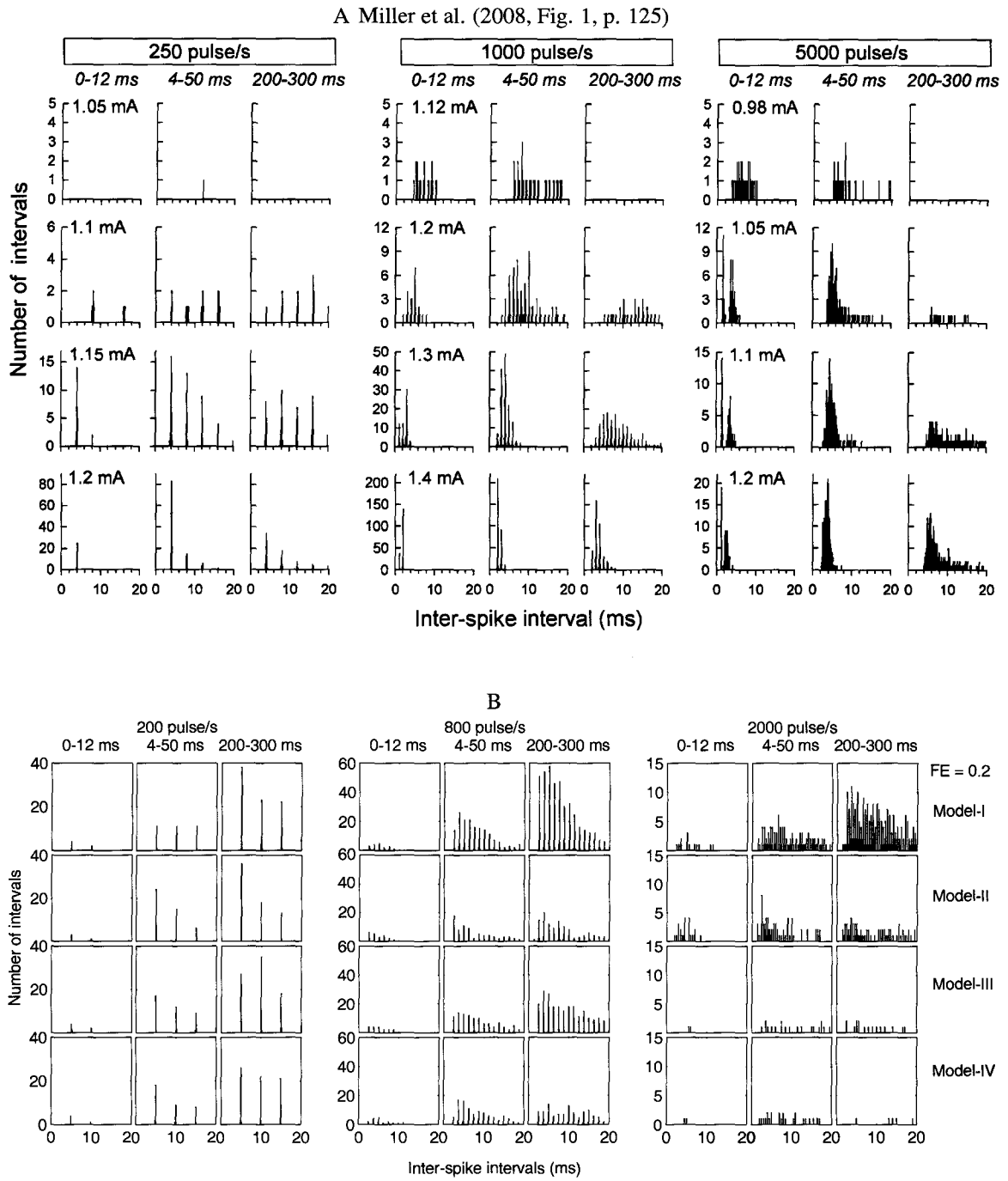

Figure 6.2: ISI from the response of Models-I, II, III, and IV (rows) at stimulus pulse rates of 200, 800, and 2000 pulse/s (columns). B, C, and D represent stimulus levels at 0.2, 0.5, and 0.8 firing probability to the first pulse. A is obtained from Miller et al. (2008, Fig. 1, p. 125). The bin width is unit50μs.

Figure 6.2: Continued

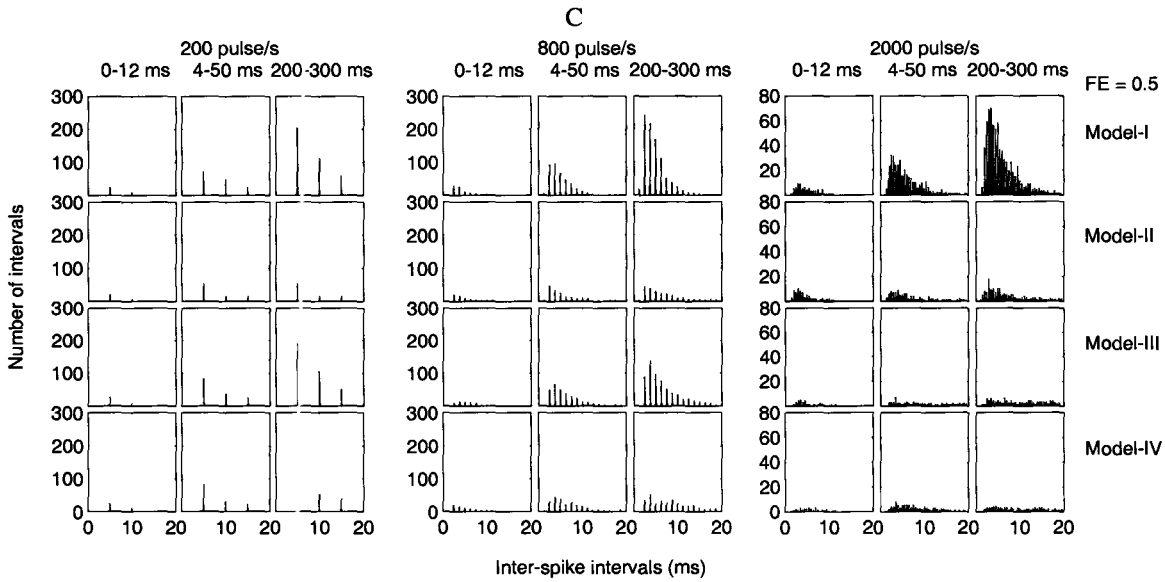

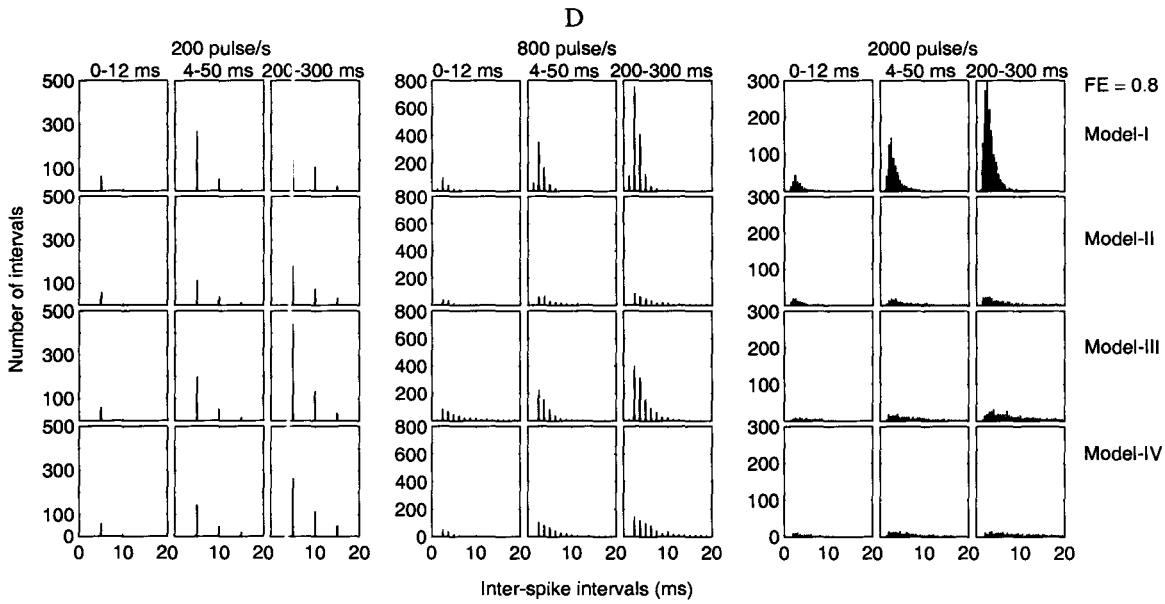

6.4 Response Rate Adaptation Analysis

6.4.1 Rate-Level Function

Response rates of Models-I, II, III, and IV are plotted in Fig. 6.3 as a function of stimulus current levels[1] and pulse rates (—, - - -, and ··· representing 200, 800, and 2000 pulse/s, respectively). Spike rates are calculated during two different onset epochs (0-4 ms and 0-12 ms—Figs. 6.3A and 6.3B, respectively).

In spite of the limited number of data points used to plot each curve (only three points each), yet there is useful information that can be extracted. During the very early onset in Fig. 6.3A, refractoriness dominates, limiting spike rates from reaching their saturation values at higher pulse rates. Interestingly, Model-III in Figs. 6.3A and 6.3B, and Model-IV in Fig. 6.3B, show lower spike rates at the 2000 pulse/s stimulus rate, in contrast to Model-I and Model-II in both panels. This pattern could support that I_{KLT} is responsible for rapid adaptation, as suggested by Mo et al. (2002). Zhang et al. (2007) have observed lower threshold levels at higher stimulus pulse rates within the first 12 ms after stimulus onset (Zhang et al., 2007, c.f. Fig. 3, p. 361). Model-II in Fig. 6.3B shows the closest results to Zhang and colleague's. However, re-plotting Fig. 6.3 with more sufficient data points would yield more accurate comparison.

6.4.2 Effects of Adaptation

To asses the effects of adaptation, rate-level functions (Zhang et al., 2007) for the four model versions, stimulated at a pulse rate of 2000 pulse/s, are illustrated in Fig. 6.4. Three different response epochs are specified. These epochs are denoted as in Zhang et al. (2007): "onset" (0-1 ms); "rapid" (0-12 ms); and "short-term" or "steady-state" (200-300 ms). The onset response is influenced by refractory effects. Model-III and Model-IV show lower response rates at the onset and rapid epochs than Models-I and II, when comparing response rates at the same firing efficiency to the first pulse. This could be an indication of rapid adaptation. Model-II and Model-IV have shallower slopes than Model-I and III for the steady-state epoch. As expected, Model-I shows no difference in response rate between the rapid and short-term epochs. These results suggest that I_h is responsible for short-term adaptation. Results from Fig. 6.4 are comparable to Zhang et al. (2007, c.f. Fig. 4, p. 361), where the "rapid" and "steady-state" epochs responses are apart, with the "steady-state" response being the lowest. It is noteworthy that the stimulus pulse rate in Zhang and colleague's figure is 5000 pulse/s.

[1]Most of the analysis in this subsection and the two subsequent subsections are built on the methods described in Zhang et al. (2007) for comparison purposes.

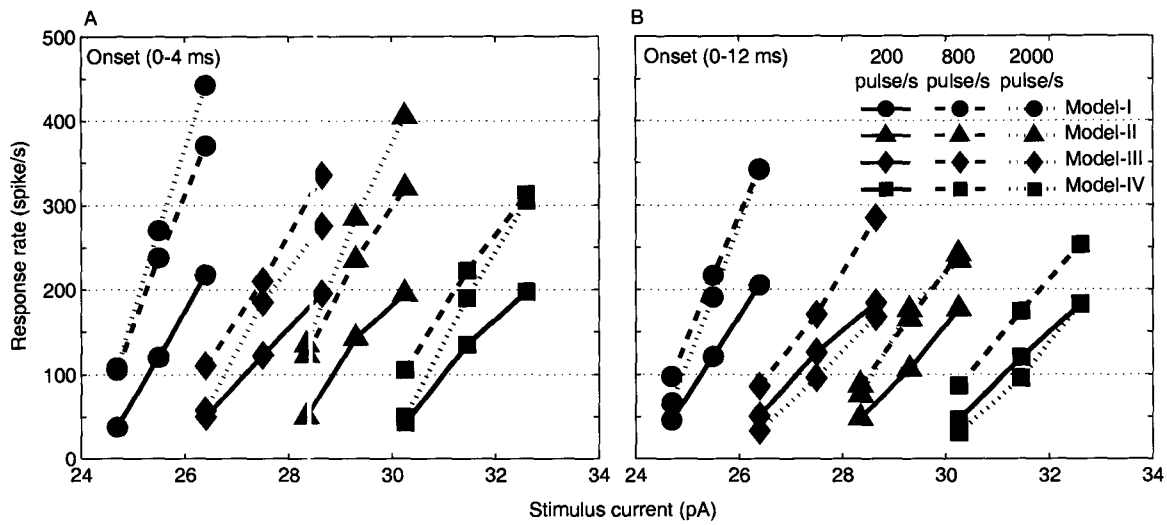

Figure 6.3: Rate-level functions of the four models at multiple pulse rates for two onset epochs. A shows the response rate at the early 4 ms after onset (0-4 ms epoch), while B shows the response during a longer epoch (0-12 ms epoch). Models-I, II, II, III, and IV are represented by filled symbols. Solid, dashed, and dotted curves represent pulse rates at 200, 800, and 2000 pulse/s, respectively.

6.4.3 Spike-Rate Adaptation

To investigate the effect of pulse rate on short-term spike-rate adaptation, two variables are defined (Zhang et al., 2007): rate decrement, which is calculated by subtracting the spike rate in the steady-state epoch (200-300 ms) from that in the onset window (0-12 ms); and the normalized rate decrement, which is computed by dividing the rate decrement by the onset response. Fig. 6.5 illustrates spike rate decrement (left column) and normalized spike rate decrement (right column) as a function of onset response rate (0-12 ms), for three stimulus pulse rates: 200, 800, and 2000 pulse/s (Fig. 6.5A & Fig. 6.5B; Fig. 6.5C & Fig. 6.5D; and Fig. 6.5E & Fig. 6.5F, respectively). Two regions of adaptation are defined: "strong" (in gray) and "weak". The strong adaptation areas in each panel are bounded by arbitrarily defined slope values between 0.75 and 1.0. It is worth noting that these strong adaptation boundaries are somewhat different than those defined in Zhang et al. (2007), where they chose an area between 0.9 and 1.0.

In all pulse rate cases, Model-I shows almost zero rate decrement, which can be interpreted as weak or no adaptation. Model-II on the other hand shows strong adaptation, which gets stronger at higher pulse rates. Model-IV tends toward stronger adaptation however slightly less than Model-II. Model-III exhibits stronger adaptation than Model-I, yet weaker than Model-II and Model-IV. These results are consistent with Zhang et al. (2007, c.f. Fig. 5, p. 363) where spike rate decrements become equal to onset response rate when the stimulus pulse rate is increased. Looking at panels B, D, and F, the normalized rate

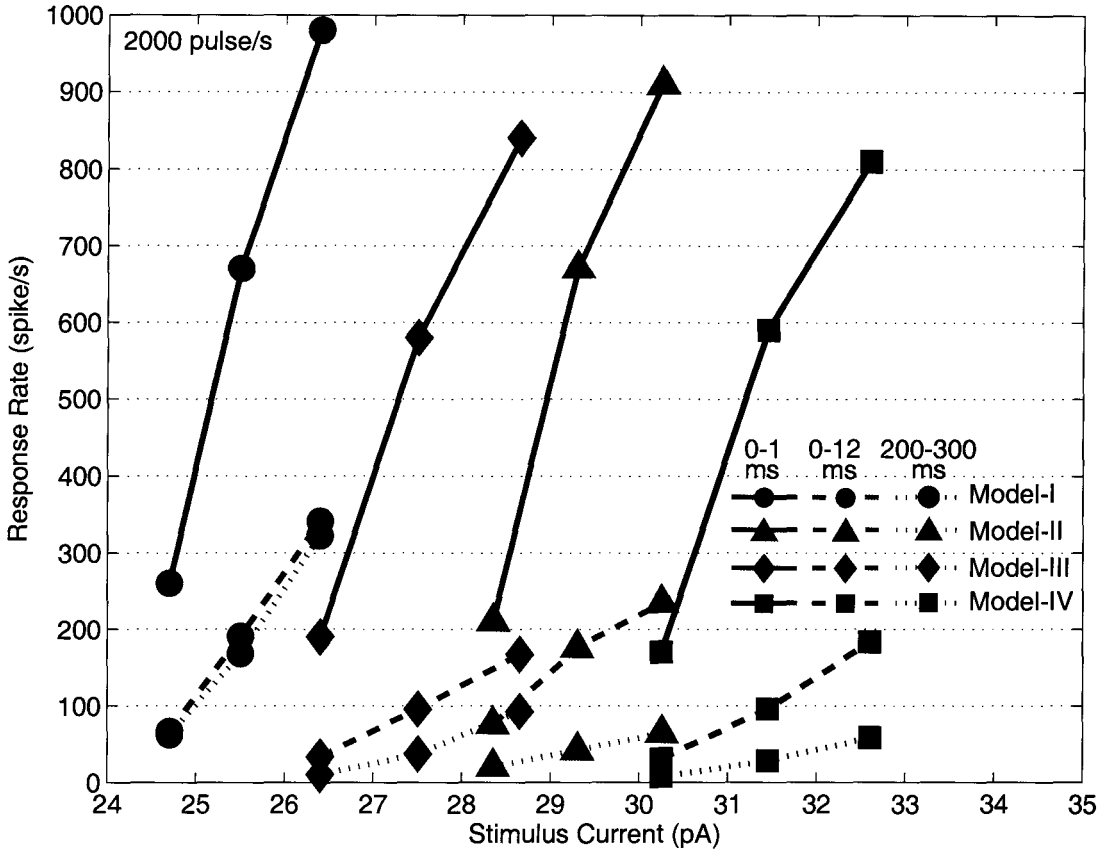

Figure 6.4: Effects of adaptation on rate-level functions at three different epochs. Analysis windows are 0-1 ms (—), 0-12 ms (- - -), and 200-300 ms (· · ·), after stimulus onset. Stimulus rate is 2000 pulse/s. Different model versions are represented by symbols.

decrements become smaller at higher onset spike rates that are greater than 200 spike/s, consistent with Zhang et al. (2007) who suggested that this effect may result from greater stimulus levels that can partially overcome adaptation.

6.4.4 Sources of Adaptation

In the aforementioned subsections, it has been suggested that I_h is probably responsible for short-term adaptation and I_{KLT} is responsible for rapid adaptation. This hypothesis is investigated in more detail below.

A novel analysis method is used to account for sources of adaptation in ANF membranes. The membrane voltage[2] at the inter-pulse gaps is averaged. One reason to do so, is because tracking membrane potential on point by point basis is impractical and time

[2]The terms membrane potential and membrane voltage are used interchangeably.

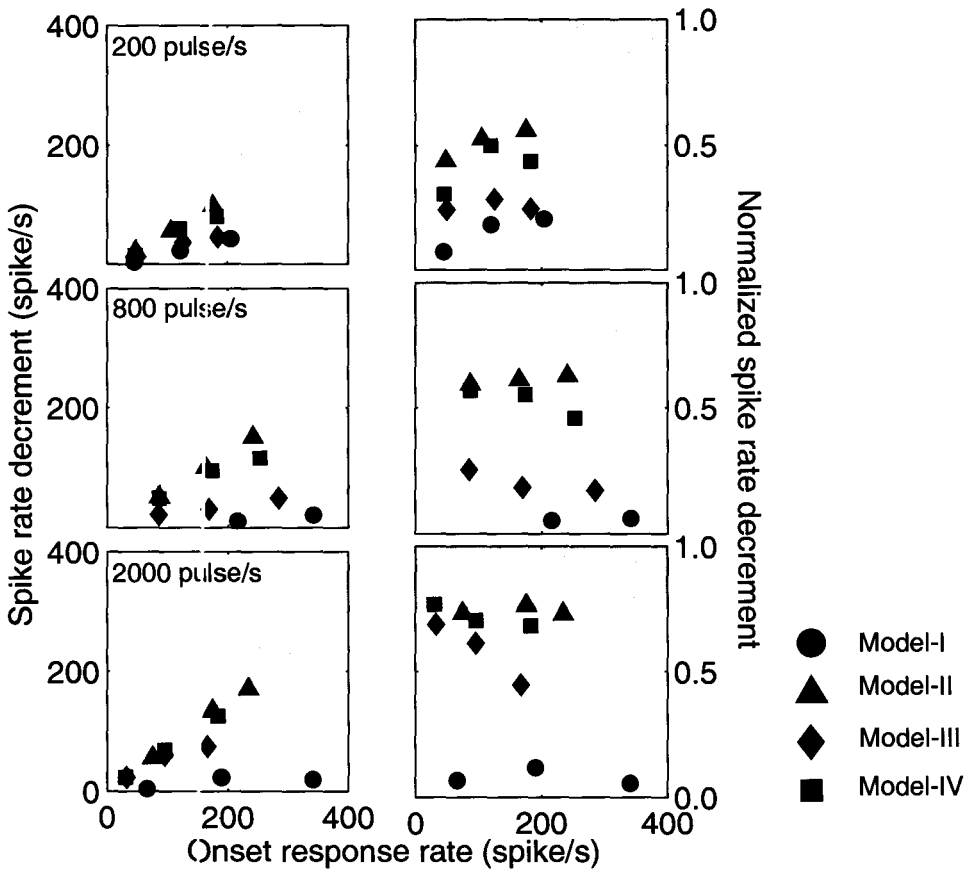

Figure 6.5: Spike rate decrement (left column) and normalized spike rate decrement (right column) as a function of onset response rate, for three stimulus pulse rates 200, 800, and 2000 pulse/s (A & B; C & D; and E & F, respectively). The gray region indicates "strong adaptation" (as defined in Zhang et al. (2007)) and is arbitrarily chosen to be $\geq$ 0.75 of the normalized rate decrement. Symbols represent the four model versions.

consuming, due to the long simulation period and high pulse rate. In Fig. 6.6, the four model versions are stimulated by pulse trains at 2000 pulse/s for a duration of 20 ms ($\equiv$ 39 pulses). The relatively short simulation duration (compared to the PSTH and ISI simulations, which lasted for 300 ms) is because short-term adaptation in this model appears at about 15 ms after stimulus onset. This value is obtained after tracking traces of membrane potentials over long periods of time at 2000 pulse/s. For each pulse, the membrane voltage is averaged over the last 100 µs of the inter-pulse gap, i.e., before the subsequent pulse. Each point in Fig. 6.6 is computed by calculating the mean of the averaged voltage for 50 Monte-Carlo simulation (filled circles). Error bars represent the mean $\pm$ one standard deviation. Five restricted spiking conditions are defined: i) "zero-current" (A); ii) "no-spike" (B); iii) "first-spike" (C); iv) "middle-spike" (D); and v) "suprathreshold" (E), which will

be explained below. Figs. 6.6B, C, and D are stimulated at subthreshold stimulus level of 0.2 firing probability to the first pulse. Fig. 6.6A is stimulated using zero current injection. Fig. 6.6E is stimulated at suprathreshold stimulus level of 0.999 firing probability to the first pulse. Models-I, II, III, and IV, are represented in blue, red, green, and black, respectively.

In the "zero-current" case (Fig. 6.6A), the inter-pulse membrane potential of Model-I is at rest (zero relative membrane potential) with almost no deviations. Model-II and Model-IV show insignificant deviations from the nominal resting potential [3]($P > 0.05$). Model-III exhibits significant fluctuations around the nominal resting membrane potential ($P < 0.01$).

In the "no-spike" case (Fig. 6.6B), membrane potential traces are taken only from trials in which no action potential was elicited. The inter-pulse membrane voltage of Model-I fluctuates around -1.2 mV. The membrane does not have enough time to recover from the hyperpolarizing phase and return to resting potential (zero relative membrane voltage) due to the high pulse rate. Model-II starts at the same values of Model-I and decreases linearly with time ($P < 0.001$) with a slope of -0.0518 mV/pulse. One possibility could be due to the closing of the I_h gating particle r during the depolarizing phase (see Fig. 4.2 on page 39). When the membrane becomes more positive, the r kinetics speed up. As a result, the time in which the r particle remains in closing state is more than the time when it is in the opening state. Therefore, the inward positive I_h current is reduced and the membrane becomes successively more negative between each pulse. This shift in membrane voltage widens the gap between the membrane potential and the threshold potential. Thus, the spike rate is reduced. This appears to be the origin of short-term adaptation. In Model-III, the membrane voltage drops at the early pulses to -2 mV and remain around this value. Looking at the kinetics of I_{KLT} (Fig. 4.2 on page 39), the activation particle w becomes activated during the depolarization phase and the kinetics speed up 10-fold. Due to the relatively fast kinetics of w ($\tau_w \simeq 100$ µs at 30 mV relative membrane potential), I_{KLT} tends to hyperpolarize the membrane (the membrane becomes more negative due to the efflux of positive charges of potassium) at the early few milliseconds. The very slow inactivating particle z is half inactivated at positive voltages and opposes the activation of w. Model-IV has a combined behavior between that of Model-II and Model-III. It starts at lower value than Model-II but higher than Model-III, then decreases linearly down to the asymptotic values of Model-III but not as low as Model-II.

In the "first-spike" case (Fig. 6.6C), the membrane potential is analyzed for trials in which an action potential at the occurrence of the first pulse only is generated. The spike due to the first pulse elevates the membrane potential of Model-I to higher levels ($\simeq$6 mV), where the membrane does not have sufficient time to return to nominal rest before the arrival of the subsequent pulse. The membrane voltage drops to -2 mV in the following two pulses before it reaches a steady-state value, as in the "no-spike" case (-1 mV). Model-II exhibits a smaller refractory period (as evidenced by the lower averaged membrane voltage

[3]Significance level P is calculated from a paired Student's t-test.

$\simeq$3.8 mV, which indicates that the membrane returns to nominal rest faster) than in Model-I. The positive elevation in the membrane potential deactivates the r particle and therefore I_h is reduced. In the following pulse, the membrane potential drops to -2 mV, similar to Model-I. However, Model-II membrane potential continues to drop until it reaches a steady-state value as in the "no-spike" case. On the other hand, Model-III and Model-IV show very short refractory period compared to Models-I and II (the membrane voltages between the first and second pulse are -0.5 and -1.5 mV, respectively). This is due to the relatively fast kinetics of w, which becomes fully activated during an action potential. The membrane potentials for both models then drop temporarily before elevating again. Model-III settles at the steady-state level as in "no-spike" while Model-IV drops again to values similar to Model-II.

In the "middle-spike" case (Fig. 6.6D), trials are taken for cases where an action potential is generated in response to the 20th pulse. The behavior noticed here is somewhat a combination between the "no-spike" and the "first-spike" cases. That is, the model behaves like the former at the beginning of the pulse sequence. Then, the membrane voltage resets and behaves like the latter case.

Finally, the "suprathreshold" case (Fig. 6.6E), in which the models are stimulated with suprathreshold current that produces 0.999 firing probability to the first pulse. The four models show first pulse response similar to that in Fig. 6.6C. Thereafter, the membrane voltage drops with subsequent pulses, with the time-course differing between models. Model-I fires continuously, as determined by the fairly constant positive relative membrane voltage. The Model-II membrane voltage decreases linearly until it reaches -5 mV. The decrease here is stronger than the one in Fig. 6.6C, because the continuous generation of action potential tends to fully deactivate the r particle, therefore, closing of r gating particle and the reduction of I_h. During later pulses, the chances for getting action potentials are lower. The Model-III membrane voltage drops rapidly to a more negative value and remains there ($\simeq -3$ mV), due to the continuous activation of w. The Model-IV membrane voltage has similar response to Model-III at the beginning of the pulse sequence, then it drops linearly until it reaches asymptotic values similar to Model-II.

To get more insight about the effects of the different stimulation conditions on the behavior of Model-II, the inter-pulse interval membrane potential and the r gating particle values of Model-II are displayed in Figs. 6.7A and 6.7B on page 83, respectively. As shown in Fig. 6.7, I_h has strong influence on the membrane potential. The continuous depolarization of the membrane during an action potential tends to deactivate r and shut down I_h. This is emphasized by the linear reduction in the relative membrane potential in the subthreshold stimulating cases ("no-spike", "first-spike", and "middle-spike"). In the "suprathreshold" case, the negative slope becomes steeper, showing more reduction than in the other cases. This is due to the continuous firing of the membrane that shifts the membrane potential to more positive values (at the peak of the AP). Therefore, the r gating particle values tend to deactivate and the I_h is reduced. The fairly shallow slopes of the membrane potentials is due to the slow kinetics of I_h.

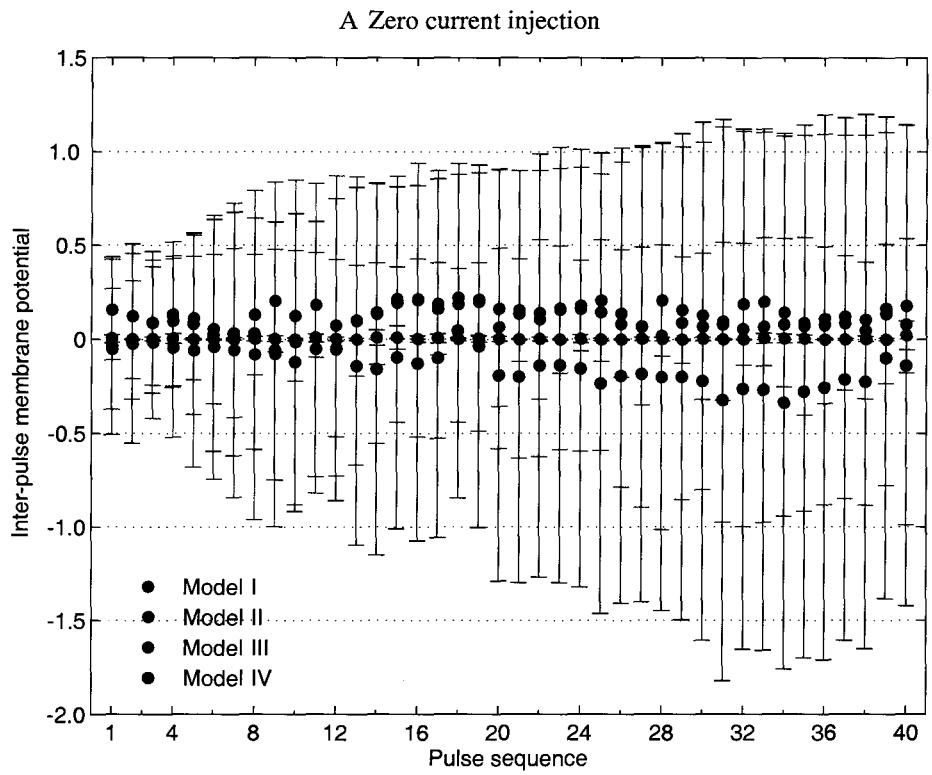

Figure 6.6: Averaged inter-pulse membrane potential as a function in pulse sequence for Models-I (blue), II (red), III (green), and IV (black). Pulse rate is 2000 pulse/s. Each point is computed by averaging the last 100 ms of the inter-pulse gap before the arrival of the subsequent pulse, then calculating the mean (filled circles) $\pm$ one standard deviation (error bars) from 50 Monte-Carlo simulations. Five stimulation conditions are defined: A is the "zero-current" injection (zero firing probability); B is "no-spike"; C is "first-spike" in response to the first pulse only; D is the "middle-spike" in response to the 20th pulse only; and E is the "suprathreshold" stimulation. Stimulus levels for B, C, and D are at 0.2 firing probability to the first pulse while the stimulus level for E is 0.999 firing probability to the first pulse. (continued on page 81 and 82 $\hookrightarrow$)

Figure 6.6: Continued

B No-spike occurrence

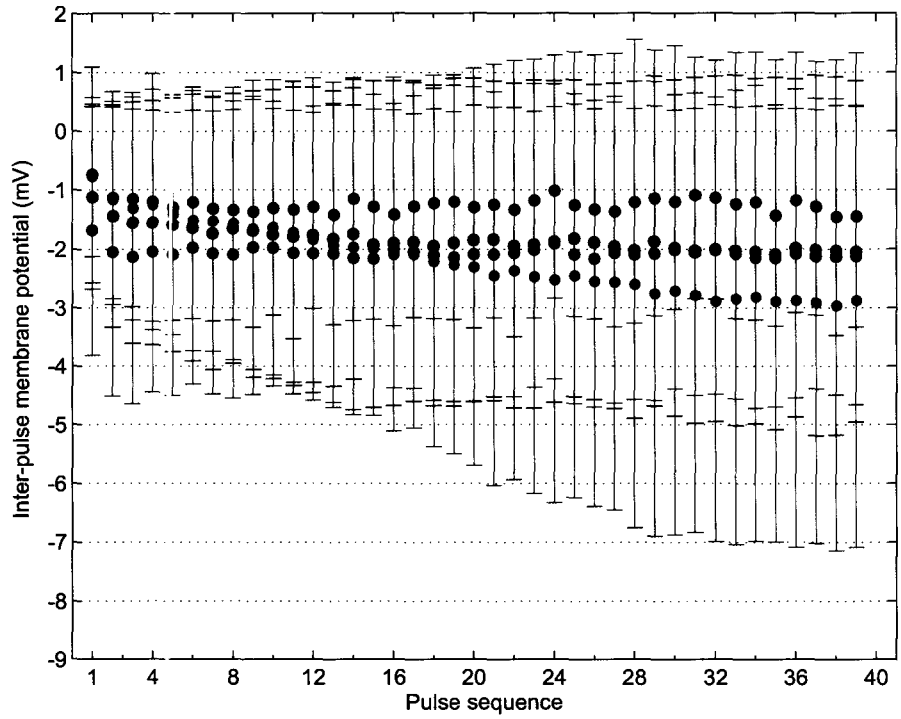

C First-spike occurrence only

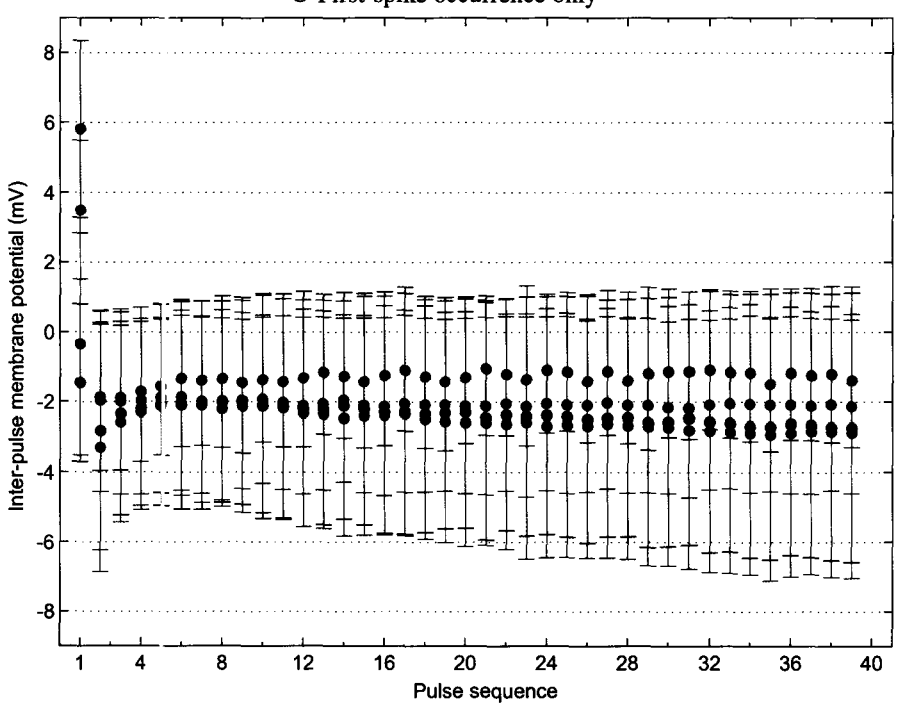

Figure 6.6: Continued

D Middle-spike occurrence only

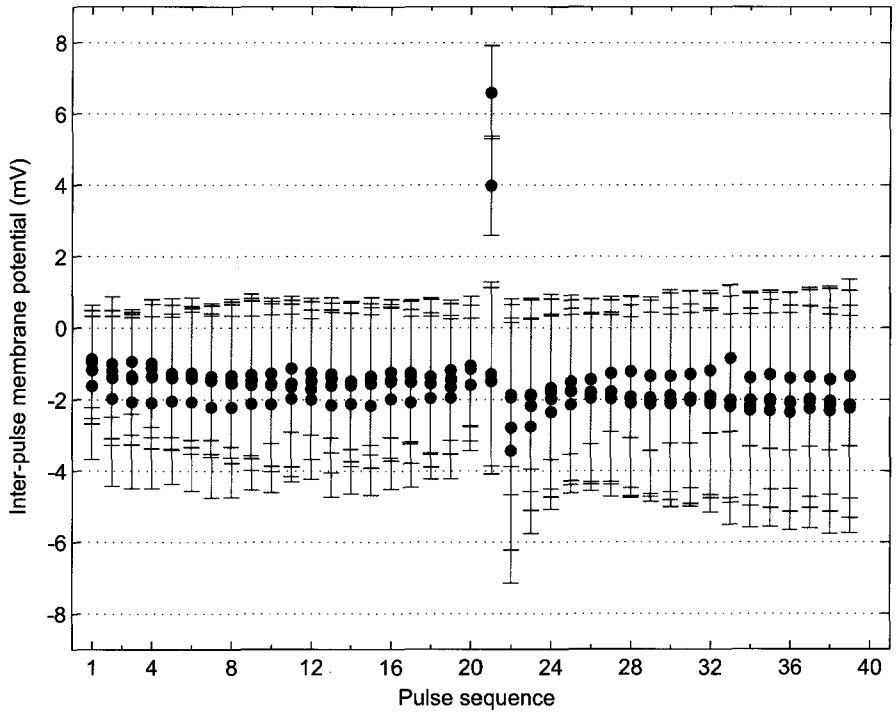

E Suprathershold

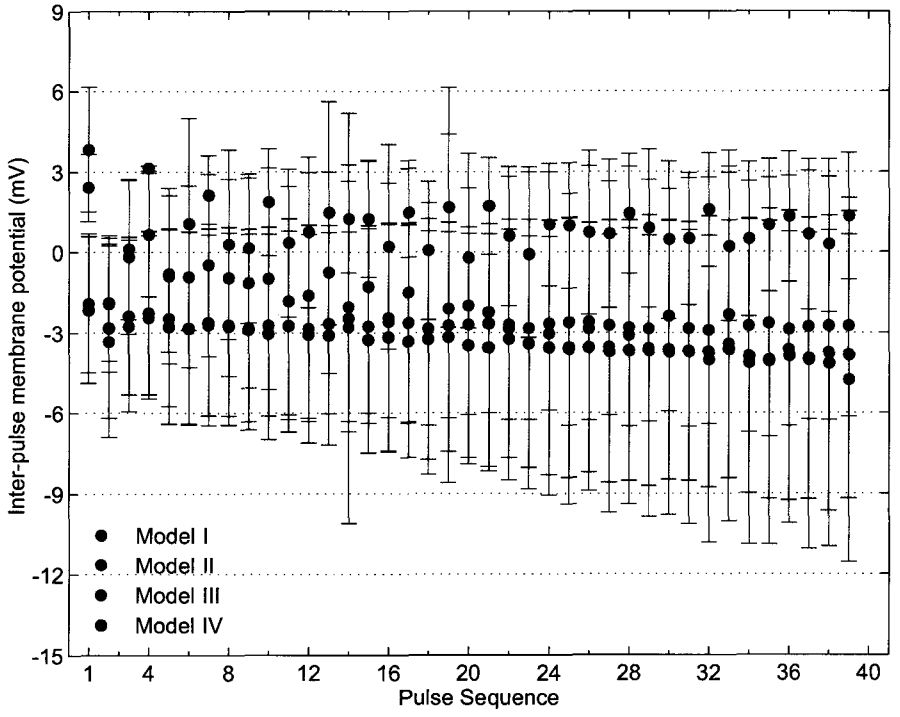

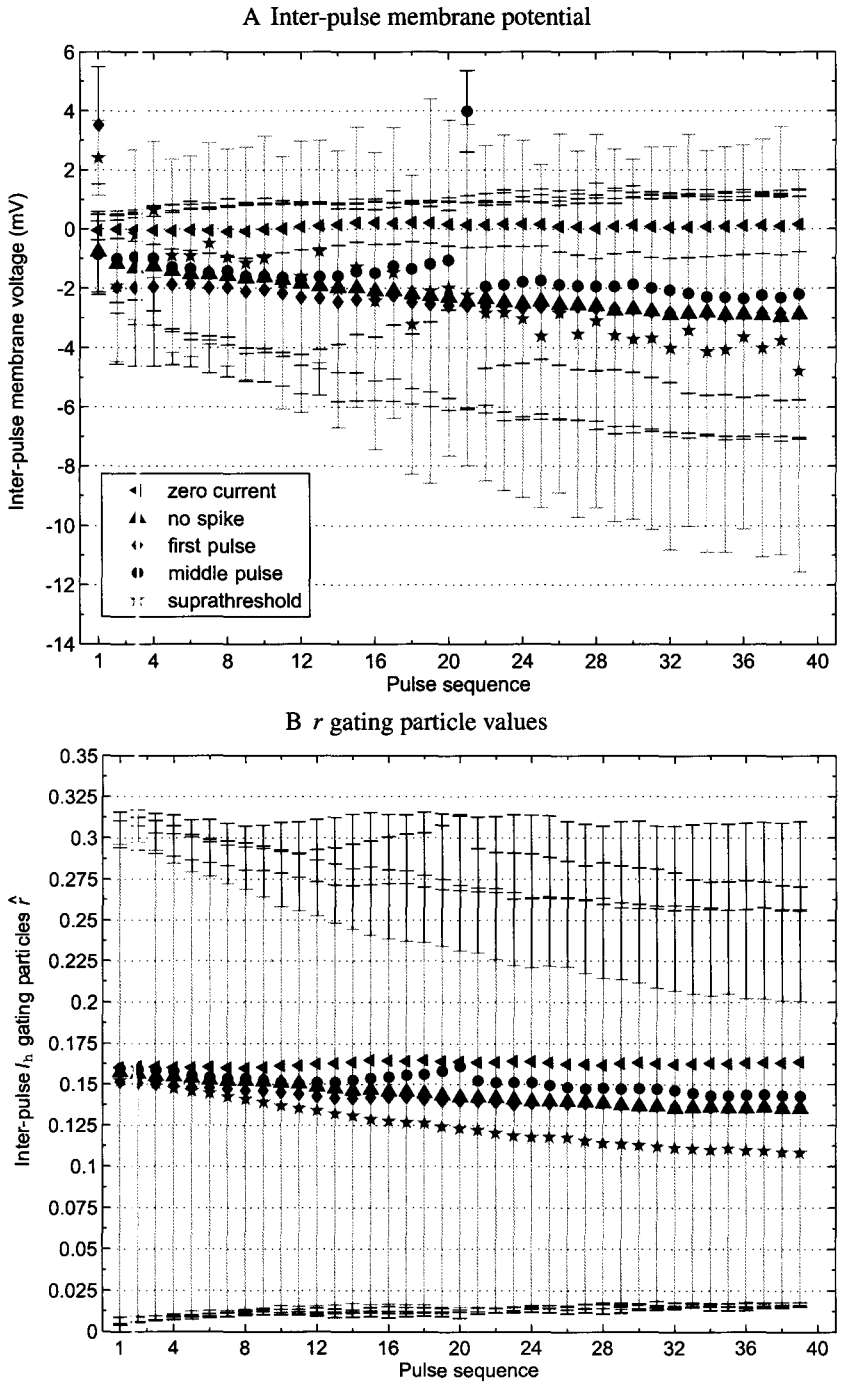

Figure 6.7: Comparison between the five stimulating cases for Model-II. A shows the inter-pulse intervals membrane potential. B shows r gating particle values.

6.5 Discussion

Clinical CIs use high rate stimulus pulses to stimulate the AN. Rubinstein et al. (1999) suggested that higher pulse rates desynchronize the ANF response, which may improve neural representation and reduce the differences between acoustic and electric stimulation. Litvak et al. (2001) investigated Rubinstein and colleagues' study and reported a reduction in spike rate in the AN with increasing pulse rate associated with electrical stimulation, which they attributed to adaptation rather than refractoriness.

Adaptation was observed during early acoustic stimulation studies of AN fibers (Kiang et al., 1965), and was attributed to the depletion of neurotransmitters at the hair cell synapse (Westermann and Smith, 1984; Smith and Brachman, 1982; Javel, 1996) . Three types of adaptation were reported: i) rapid; ii) short-term; iii) long-term. Javel (1996) reported a fourth type, that is very-long-term adaptation. Nonetheless, studies have shown that hair cells are not the only source of adaptation. Adaptation may results also from intrinsic membrane properties (Mo and Davis, 1997b; Mo et al., 2002; Nourski et al., 2006; Zhang et al., 2007). Zhang et al. (2007) and Miller et al. (2008) built their work on Litvak and colleagues, and compared between electrical and acoustic stimulations. They concluded that electrical stimulation response shows rapid- and short-terms adaptation time constants that are similar to those observed during acoustic stimulation (Zhang et al., 2007; Miller et al., 2008). Adaptation in spike rate reported in Zhang et al. (2007) was totaly electrical as the sensory organs of the ears were chemically deafened. This should resemble the case when nearly all the hair cells are completely damaged during clinically implanted CIs stimulation.

The analysis conducted in this chapter was to build an accurate Hodgkin-Huxley based model that may better explain adaptation in ANFs in response to electric stimulation. Results of pulse-train response were presented. Responses from Models-II, III, and IV (Hodgkin-Huxley model with I_h, Hodgkin-Huxley model with I_{KLT}, and Hodgkin-Huxley model with bothI_h and I_{KLT}, respectively) were compared to the response of Model-I (standard Hodgkin-Huxley model), and to physiological data from Zhang et al. (2007) and Miller et al. (2008). The standard Hodgkin-Huxley model in this report did not show any signs of spike rate adaptation. Only, spike reduction due to refractoriness was observed.

Mo et al. (2002) stimulated the spiral ganglion neurons of a mouse and concluded that low-threshold potassium is responsible in maintaining rapid adaptation. Adding I_{KLT} to Hodgkin-Huxley model reduces spike rate due to the activation of w, which influences the membrane to be more negative. This reduction more likely explains rapid adaptation, consistent with Mo et al. (2002). One can argue that the reduction is due to refractoriness and/or the low firing probability. However, the presence of I_{KLT} shortens the refractory period as reported in Rothman and Manis (2003c). The simulations show similar results, where the model with the I_{KLT} has shorter refractory period than the standard Hodgkin-Huxley model (Fig. 6.6).

Adding I_h to the standard Hodgkin-Huxley model showed strong short-term adaptation

effects that increases with pulse rate. Adaptation observed in the simulation results were very close to physiological results (Zhang et al., 2007). When the membrane is depolarized, the r gating particle kinetics become faster than at rest. Consequently, I_h gets fully deactivated, and, the membrane potential becomes more negative between pulses. As a result, the current required to reach threshold increases and the spike rate is reduced for a constant current pulse train. These results are matched to physiological data, as Mo and Davis (1997b), Bal and Oertel (2000), and Rodrigues and Oertel (2006) have shown that I_h regulates excitability in neurons and maintain resting potential. Long-term adaptation was not considered in this study.

Adding both I_h and I_{KLT} to the standard Hodgkin-Huxley model show combined characteristics of I_{KLT} and I_h alone, that is, rapid and short-term adaptation, and short refractory period. It should be noted that adaptation and refractoriness have combined effects on the spike reduction. Refractoriness limits the maximum spike rate, while adaptation reduces the spike rate across the stimulation period cumulatively (Miller et al., 2008).

In summary, I_h is responsible for short-term adaptation and I_{KLT} is responsible for rapid adaptation. The proposed model shows more accurate simulation results than the standard Hodgkin-Huxley model.

Chapter 7

Conclusions and Future Work

7.1 Summary of Conclusions

This thesis describes a computational model for a node of Ranvier in auditory nerve fibers. The model is based on a stochastic Hodgkin-Huxley model adjusted to mammalian body temperature. The standard Hodgkin-Huxley model includes the fast sodium and the delayed rectifier potassium currents. The standard Hodgkin-Huxley model is modified to include: i) hyperpolarization activated cation currents and ii) the low threshold potassium currents. Results are computed from the response to single-pulse and pulse-train currents. Stimulation pulses are similar to those used in clinical cochlear implants. The proposed model presented here is an attempt to improve modelling of ANFs in response to CI stimulation and describe more accurately phenomena not fully explained in previous models. This model may help in improving CI functionality by designing new signal processing strategies that take into account adaptation in spike rate that results from high stimulus pulse rates (Litvak et al., 2001; Javel and Shepherd, 2000; Zhang et al., 2007).

Adding I_{KLT} to an Hodgkin-Huxley model improves the response of the model by showing some of the membrane temporal properties that are not described by the Hodgkin-Huxley model alone. Simulation results show a positive correlation between random threshold fluctuations and pulse width. This is consistent with physiological data from cat ANFs (Bruce et al., 2000b; Ferguson et al., 2003). Adding I_{KLT} also acts to reduce the refractory period. Rothman and Manis (2003c) reported similar result in VCN neurons. Rapid adaptation explained in Mo and Davis (1997b), Mo et al. (2002), and Zhang et al. (2007) is demonstrated in the pulse-train simulations.

When I_h is included, the model exhibits the short-term adaptation explained in Zhang et al. (2007) and Miller et al. (2008). Simulation results show that the reduction in spike rate is attributed to cumulative decrease in the membrane potential, therefore acts on reducing the discharge probability. The decrease in membrane potential is also observed even when no action potential (spike) is elicited. This would suggests that spike rate adaptation is stimulus dependent rather than spike dependent. This argument is supported by Mo and

Davis (1997a), Bal and Oertel (2000), and Rodrigues and Oertel (2006) who showed that I_h maintains resting potential and controls excitability.

Finally, the model shows combined properties of I_h and I_{KLT} when both currents are added simultaneously.

7.2 Limitations of the Model and Future Developments

Although, the model presented in this study accounts for many of the membrane properties observed in the physiological data and not considered in the standard Hodgkin-Huxley model, a number of issues remain unresolved. A series of approximations for the membrane characteristics are assumed to facilitate in the implementation of the model, thereby, limiting the accuracy of the model:

1. Activation/inactivation curves for w, z, and r are expressed in terms of relative membrane potential rather than their absolute values to accommodate for the differences in resting membrane potential values between different models on which the channel equations were based.

2. Values for single channel conductances for I_h and I_{KLT} (γ_h and γ_{KLT}, respectively) and the number of channels need further investigation. The criteria used in their selection in this study is somewhat speculative. Physiological studies have shown that there are variations in the maximum conductance of I_h ($\bar{g}_h$) values along different regions in the auditory system (Mo and Davis, 1997a; Bal and Oertel, 2000). The number of channels at the nodes of Ranvier is calculated from channel densities. Channel densities also are non-uniformly distributed along a single axon, which implies that the number of channels varies as well (Bruce et al., 1999c).

3. The leakage reversal potential E_{lk} is kept variable to maintain a fixed resting membrane potential regardless of the channel-type combination used (Rothman and Manis, 2003b). An alternative approach could be to keep E_{lk} fixed and vary the leakage resistance. However, in this case large changes in the leakage resistance would be required if the value E_{lk} were close to the combined reversal potential of the other channels.

4. Switching between model versions with and without the KLT channel type is achieved by turning the conductance γ_{KLT} "on" and "off" without changing the number of delayed-rectifier potassium channels. An alternative approach could be adjusting the distribution of delayed-rectifier potassium channels to keep a fixed number of potassium channels for the different versions of the model.

5. The thermal coefficient factors $Q10$ for I_h and I_{KLT} are still speculative (Rothman and Manis, 2003b; Rodrigues and Oertel, 2006).

6. The time course of I_h single channel kinetics is described in this model by a single exponential function (Fu et al., 1997; Rothman and Manis, 2003b). However, more than one study has shown that I_h kinetics can best be fit to a double exponential function (Chen, 1997; Bal and Oertel, 2000; Rodrigues and Oertel, 2006). Bal and Oertel (2000) went further by fitting the I_h deactivation time course to a single exponential function whereas the activation time course was fit to a double exponential function.

7. The model is limited to a single node of Ranvier, which ignores the spatial aspect of the ANFs. Hence, the model should be extended into an axonal model which consists of several nodes of Ranvier and possibly the soma. This could be beneficial when studying the interaction between nodes during action potential generation. The intracellular current injection should be replaced with an extracellular electrode model to resemble CI stimulation and account for nodes interaction.

8. The model does not clearly differentiate between auditory nerve fibers in healthy or deafened ears. However, CI users suffer mainly from sensorineural hearing loss, which is associated with substantial changes in the nerve morphology (Shepherd and Javel, 1997). Such changes may include: extensive loss of the peripheral dendrites, demyelinization of spiral ganglion neurons, and change in sites of spike initiation during short-term deafness, and severe loss in the population of spiral ganglion neurons during long-term deafness. Shepherd and Javel (1997) have shown that these pathological changes affect the nerve response. Cochlear pathologies should be taken into consideration in future models.

9. The model only addresses four types of voltage-gated ion channels (fast Na^+, delayed rectifier K^+, KLT and HCN). However there are other types of channels, such as the voltage-gated Ca^{2+}, calcium activated K^+, and transient K^+ (Mo and Davis, 1997a,b; Hille, 2001; Adamson et al., 2002; Rothman and Manis, 2003a), not considered in this model, that may play a role in shaping the action potential and the membrane properties. Adding these channels to the model should improve its accuracy.

10. From the above observations, it is clear that further physiological studies for more accurate estimates of membrane parameters would be beneficial.

Appendix A

Simulation Results of Chapter 5

Table A.1: 100 µs/ϕ— 0 µs gap

	anodic				cathodic				
	I	II	III	IV	I	II	III	IV	
TH	25.50	29.27	27.49	31.40	43.35	42.28	42.24	42.24	pA
RS	3.85	3.83	4.93	4.40	4.14	4.05	4.66	4.40	%
LT	0.288	0.282	0.280	0.272	0.455	0.432	0.437	0.418	ms
JT	20.80	25.4	22.8	18.1	39.36	35.57	33.87	26.05	µs
Amp	130.30	126.90	126.60	123.50	134.41	131.46	131.45	128.84	mV

Table A.2: 700 µs/ϕ— 0 µs gap

	anodic				cathodic				
	I	II	III	IV	I	II	III	IV	
TH	8.01	11.38	11.90	15.60	7.97	11.07	9.67	13.06	pA
RS	4.33	3.93	8.77	7.21	4.28	4.15	7.79	6.68	%
LT	0.79	0.745	0.548	0.52	1.53	1.48	1.35	1.29	ms
JT	69.86	84.63	72.71	73.23	65.74	78.47	75.92	70.32	µs
Amp	127.13	123.84	124.74	122.04	131.15	128.24	129.47	127.38	mV

Table A.3: Monophasic

	anodic, 100 µs				anodic, 700 µs				
	I	II	III	IV	I	II	III	IV	
TH	21.62	25.67	24.01	28.06	7.97	11.33	11.93	15.55	pA
RS	4.46	4.10	5.45	5.02	4.29	4.03	9.04	7.27	%
LT	0.34	0.32	0.31	0.30	0.81	0.75	0.53	0.51	ms
JT	43.39	33.64	30.25	28.57	77.21	86.91	69.70	67.01	µs
Amp	131.78	129.09	128.26	125.73	127.17	123.90	125.16	122.62	mV

Table A.4: 100 µs/ϕ— 200 µs gap

	anodic				cathodic				
	I	II	III	IV	I	II	III	IV	
TH	21.63	25.69	24.03	28.03	24.37	26.78	24.79	27.73	pA
RS	4.37	3.95	5.68	5.15	4.22	4.02	5.45	5.06	%
LT	0.34	0.32	0.31	0.30	0.64	0.62	0.62	0.60	ms
JT	36.54	34.38	31.50	27.12	43.64	37.29	36.98	31.63	µs
Amp	131.64	129.00	128.28	125.65	133.76	130.98	130.83	128.24	mV

Bibliography

C. L. Adamson, M. A. Reid, Z. L. Mo, J. Bowne-English, and R. L. Davis. Firing features and potassium channel content of murine spiral ganglion neurons vary with cochlear location. *J. Comp. Neurol.*, 447(4):331–350, 2002.

R. Bal and D. Oertel. Hyperpolarization-Activated, Mixed-Cation Current (Ih) in Octopus Cells of the Mammalian Cochlear Nucleus. *J. Neurophysiol.*, 84(2):806–817, 2000.

I. C. Bruce. Implementation issues in approximate methods for stochastic Hodgkin–Huxley models. *Ann. Biomed. Eng.*, 35(2):315–318, 2007.

I. C. Bruce, L. S. Irlicht, M. W. White, S. J. O'Leary, S. Dynes, E. Javel, and G. M. Clark. A stochastic model of the electrically stimulated auditory nerve: Pulse-train response. *IEEE Trans. Biomed. Eng.*, 46(6):630–637, 1999a.

I. C. Bruce, M. W. White, L. S. Irlicht, S. J. O'Leary, and G. M. Clark. The effects of stochastic neural activity in a model predicting intensity perception with cochlear implants: Low-rate stimulation. *IEEE Trans. Biomed. Eng.*, 46(12):1393–1404, 1999b.

I. C. Bruce, M. W. White, L. S. Irlicht, S. J. O'Leary, S. Dynes, E. Javel, and G. M. Clark. A stochastic model of the electrically stimulated auditory nerve: Single-pulse response. *IEEE Trans. Biomed. Eng.*, 46(6):617–629, 1999c.

I. C. Bruce, L. S. Irlicht, M. W. White, S. J. O'Leary, and G. M. Clark. Renewal-process approximation of a stochastic threshold model for electrical neural stimulation. *J. Comput. Neurosci.*, 9(2):119–132, 2000a.

I. C. Bruce, E. D. Young, and M. B. Sachs. Physiological modeling for hearing aid design. In *Abstracts of the IHCON 2000 International Hearing Aid Research Conference*, 2000b.

L. A. Cartee. Evaluation of a model of the cochlear neural membrane. II: Comparison of model and physiological measures of membrane properties measured in response to intrameatal electrical stimulation. *Hear. Res.*, 146(1-2):153–166, 2000.

L. A. Cartee, C. van den Honert, C. C. Finley, and R. L. Miller. Evaluation of a model of the cochlear neural membrane. I: Physiological measurement of membrane characteristics in response to intrameatal electrical stimulation. *Hear. Res.*, 146(1-2):143–152, 2000.

C. Chen. Hyperpolarization-activated current (ih) in primary auditory neurons. *Hear. Res.*, 110(1–2):179–90, 1997.

W. C. Chen and R. L. Davis. Voltage-gated and two-pore-domain potassium channels in murine spiral ganglion neurons. *Hear. Res.*, 222(1-2):89–99, 2006.

C. C. Chow and J. A. White. Spontaneous action potentials due to channel fluctuations. *Biophys. J.*, 71:3013–3021, 1996.

G. Clark. *Cochlear Implants: Fundamentals and Applications*. Springer, 2003.

W. D. Ferguson, L. M. Collins, and D. W. Smith. Psychophysical threshold variability in cochlear implant subjects. *Hear. Res.*, 180(1–2):101–113, 2003.

R. F. Fox. Stochastic versions of the Hodgkin–Huxley equations. *Biophys. J.*, 72(5):2068–2074, May 1997.

X. W. Fu, B. L. Brezden, and S. H. Wu. Hyperpolarization-Activated Inward Current in Neurons of the Rat's Dorsal Nucleus of the Lateral Lemniscus In Vitro. *J. Neurophysiol.*, 78(5):2235–2245, 1997.

N. L. Golding, M. J. Ferragamo, and D. Oertel. Role of intrinsic conductances underlying responses to transients in octopus cells of the cochlear nucleus. *J. Neurosci.*, 19(8): 2897–2905, 1999.

H. Gray and Inc NetLibrary. *Anatomy, descriptive and surgical.* Running Press Book Publishers, 1974. URL `http://libaccess.mcmaster.ca/login?url=http://www.netLibrary.com/urlapi.asp?action=summary&v=1&bookid=33051`.

J. J. Grigg, H. M. Brew, and B. L. Tempel. Differential expression of voltage-gated potassium channel genes in auditory nuclei of the mouse brainstem. *Hear. Res.*, 140(1-2): 77–90, 2000.

A. C. Guyton. *Textbook of Medical Physiology*. WB Saunders, 10th edition, 2000.

B. Hille. *Ion channels of excitable membranes*. Sinauer Sunderland, Mass, 3rd edition, 2001.

A. Hodgkin and A. Huxley. A quantitative description of membrane current and its application to conduction and excitation in nerve. *J. Physiol.*, 117:500–44, 1952.

J. R. Huguenard and D. A. McCormick. Simulation of the currents involved in rhythmic oscillations in thalamic relay neurons. *J. Neurophysiol.*, 68(4):1373–1383, 1992.

E. Javel. Long-term adaptation in cat auditory-nerve fiber responses. *J. Acoust. Soc. Am.*, 99:1040, 1996.

E. Javel and R. K. Shepherd. Electrical stimulation of the auditory nerve. III. Response initiation sites and temporal fine structure. *Hear. Res.*, 140(1-2):45–76, February 2000.

N. Y. S. Kiang, T. Watanabe, E. C. Thomas, and L. F. Clark. Discharge patterns of single fibers in the cat's auditory nerve. Res. Monogr. nr. 35, M.I.T. Press, Cambridge, MA, 1965.

C. Koch. *Biophysics of computation: information processing in single neurons.* Oxford University Press, New York, 1999.

L. Litvak, B. Delgutte, and D. Eddington. Auditory nerve fiber responses to electric stimulation: Modulated and unmodulated pulse trains. *J. Acoust. Soc. Am.*, 110:368, 2001.

P. C. Loizou. Mimicking the human ear. *IEEE. Sig. Proces. Magaz.*, 15(5):101–130, 1998.

O. Macherey, R. P. Carlyon, A. van Wieringen, J. M. Deeks, and J. Wouters. Higher Sensitivity of Human Auditory Nerve Fibers to Positive Electrical Currents. *J. Assoc. Res. Otolaryngol.*, 2008.

P. B. Manis and S. O. Marx. Outward currents in isolated ventral cochlear nucleus neurons. *J. Neurosci.*, 11(9):2865–2880, 1991.

A. J. Matsuoka, J. T. Rubinstein, P. J. Abbas, and C. A. Miller. The effects of interpulse interval on stochastic properties of electrical stimulation: Models and measurements. *IEEE Trans. Biomed. Eng.*, 48(4):416–424, 2001.

C. A. Miller, P. J. Abbas, and J. T. Rubinstein. An empirically based model of the electrically evoked compound action potential. *Hear. Res.*, 135(1–2):1–18, 1999a.

C. A. Miller, P. J. Abbas, and B. K. Robinson. Response Properties of the Refractory Auditory Nerve Fiber. *J. Assoc. Res. Otolaryngol.*, 2(3):216–232, 2001a.

C. A. Miller, B. K. Robinson, J. T. Rubinstein, P. J. Abbas, and C. L. Runge-Samuelson. Auditory nerve responses to monophasic and biphasic electric stimuli. *Hear. Res.*, 151 (1-2):79–94, 2001b.

C.A. Miller, N. Hu, F. Zhang, B.K. Robinson, and P.J. Abbas. Changes Across Time in the Temporal Responses of Auditory Nerve Fibers Stimulated by Electric Pulse Trains. *J. Assoc. Res. Otolaryngol.*, 9(1):122–137, 2008.

R. L. Miller, B. M. Calhoun, and E. D. Young. Discriminability of vowel representations in cat auditory-nerve fibers after acoustic trauma. *J. Acoust. Soc. Am.*, 105(1):311–325, 1999b.

R. L. Miller, B. M. Calhoun, and E. D. Young. Contrast enhancement improves the representation of /ɛ/-like vowels in the hearing-impaired auditory nerve. *J. Acoust. Soc. Am.*, 106(5):2693–2708, 1999c.

H. Mino and J. T. Rubinstein. Effects of neural refractoriness on spatio-temporal variability in spike initiations with electrical stimulation. *IEEE Trans. Neural Syst. Rehabil. Eng.*, 14(3):273–280, 2006.

H. Mino, J. T. Rubinstein, and J. A. White. Comparison of algorithms for the simulation of action potentials with stochastic sodium channels. *Ann. Biomed. Eng.*, 30(4):578–587, April 2002.

H. Mino, J. T. Rubinstein, C. A. Miller, and P. J. Abbas. Effects of electrode-to-fiber distance on temporal neural response with electrical stimulation. *IEEE Trans. Biomed. Eng.*, 51(1):13–20, 2004.

Z. L. Mo and R. L. Davis. Heterogeneous voltage dependence of inward rectifier currents in spiral ganglion neurons. *J. Neurophysiol.*, 78(6):3019–27, 1997a.

Z. L. Mo and R. L. Davis. Endogenous firing patterns of murine spiral ganglion neurons. *J. Neurophysiol.*, 77(3):1294–1305, 1997b.

Z. L. Mo, C. L. Adamson, and R. L. Davis. Dendrotoxin-sensitive k currents contribute to accommodation in murine spiral ganglion neurons. *J. Neurophysiol.*, 542(3):763–778, 2002.

E. Neher and B. Sakmann. Single-channel currents recorded from membrane of denervated frog muscle fibers. *Nature*, 260(5554):799–802, 1976.

K. V. Nourski, P. J. Abbas, and C. A. Miller. Effects of Remaining Hair Cells on Cochlear Implant Function, 15th Quarterly Progress Report. *NIH Contract*, 1:2–1005, 2006.

T. M. Perney and L. K. Kaczmarek. Localization of a High Threshold Potassium Channel in the Rat Cochlear Nucleus. *J. Comp. Neurol.*, 386:178–202, 1997.

T. M. Perney, J. Marshall, K. A. Martin, S. Hockfield, and L. K. Kaczmarek. Expression of the mRNAs for the Kv3. 1 potassium channel gene in the adult and developing rat brain. *J. Neurophysiol.*, 68(3):756–766, 1992.

J. O. Pickles. *An Introduction to the Physiology of Hearing*. Academic Press Inc. Ltd, London, 1982.

F. Rattay, R. N. Leao, and H. Felix. A model of the electrically excited human cochlear neuron. II. Influence of the three-dimensional cochlear structure on neural excitability. *Hear. Res.*, 153(1–2):64–79, 2001a.

F. Rattay, P. Lutter, and H. Felix. A model of the electrically excited human cochlear neuron. I. Contribution of neural substructures to the generation and propagation of spikes. *Hear. Res.*, 153(1–2):43–63, 2001b.

A. R. A. Rodrigues and D. Oertel. Hyperpolarization-Activated Currents Regulate Excitability in Stellate Cells of the Mammalian Ventral Cochlear Nucleus. *J. Neurophysiol.*, 95(1):76–87, 2006.

J. S. Rothman and P. B. Manis. Differential expression of three distinct potassium currents in the ventral cochlear nucleus. *J. Neurophysiol.*, 89(6):3070–3082, 2003a.

J. S. Rothman and P. B. Manis. The Roles Potassium Currents Play in Regulating the Electrical Activity of Ventral Cochlear Nucleus Neurons. *J. Neurophysiol.*, 89(6):3097–3113, 2003b.

J. S. Rothman and P. B. Manis. Kinetic analyses of three distinct potassium conductances in ventral cochlear nucleus neurons. *J. Neurophysiol.*, 89(6):3083–3096, 2003c.

J. T. Rubinstein. Threshold fluctuations in an N sodium channel model of the node of Ranvier. *Biophysical Journal*, 68:779–785, 1995.

J. T. Rubinstein, B. S. Wilson, C. C. Finley, and P. J Abbas. Pseudospontaneous activity: Stochastic independence of auditory nerve fibers with electrical stimulation. *Hear. Res.*, 127:108–118, 1999.

J.T. Rubinstein. How cochlear implants encode speech. *Curr. Opin. Otolaryngol. & Head Neck Surg.*, 12(5):444, 2004.

M. B. Sachs, I. C. Bruce, R. L. Miller, and E. D. Young. Biological basis of hearing-aid design. *Ann. Biomed. Eng.*, 30(2):157–168, 2002.

D. W. F. Schwarz and R. W. Ward Tomlinson. A complex tone code in the auditory cortex. *The Journal of Otolaryngology*, 16(5):316–321, 1987.

R. K. Shepherd and E. Javel. Electrical stimulation of the auditory nerve: I. Correlation of physiological responses with cochlear status. *Hear. Res.*, 108:112–144, 1997.

R. K. Shepherd and E. Javel. Electrical stimulation of the auditory nerve: II. Effect of stimulus waveshape of single fibre response properties. *Hear. Res.*, 130:171–188, 1999.

R. K. Shepherd, J. H. Baxi, and N. A. Hardie. Response of inferior colliculus neurons to electrical stimulation of the auditory nerve in neonatally deafened cats. *J. Neurophysiol.*, 82(3):1363–1380, 1999.

D. J. Sly, L. F. Heffer, M. W. White, R. K. Shepherd, M. G. J. Birch, R. L. Minter, N. E. Nelson, A. K. Wise, and S. J. O'Leary. Deafness alters auditory nerve fibre responses to cochlear implant stimulation. *Europ. J. Neurosci.*, 26(2):510–522, 2007.

R. L. Smith and M. L. Brachman. Adaptation in auditory-nerve fibers: A revised model. *Biol. Cybern.*, 44(2):107–120, 1982.

A. F. Strassberg and L. J. DeFelice. Limitations of the Hodgkin–Huxley formalism: effects of single channel kinetics on transmembrane voltage dynamics. *Neural Comput.*, 5(6): 843–855, 1993.

S. H. Strogatz. *Nonlinear Dynamics and Chaos: With Applications to Physics, Biology, Chemistry, and Engineering*. Perseus Books Group, 2000.

G. J. Tortora and B. Derrickson. *Principles of anatomy and physiology, l0th edn.* John Wiley & Sons Inc., New York, 2003.

A. A. Verveen. On the fluctuation of threshold of the nerve fibre. In D. B. Tower and J. P. Schadé, editors, *Structure and Function of The Cerebral Cortex*, pages 282–288, Amsterdam, The Netherlands, 1960. Elsevier.

A. A. Verveen. Axon diameter and fluctuation in excitability. *Acta morph. neerl.-scand.*, 5:79–85, 1962.

A. A. Verveen and H. E. Derksen. Fluctuation phenomena in nerve membrane. *Proc. IEEE*, 56(6):906–916, 1968.

L. A. Westermann and R. L. Smith. Rapid and short-term adaptation in auditory nerve response. *Hear. Res.*, 15:249–260, 1984.

F. Zhang, C. A. Miller, B. K. Robinson, P. J. Abbas, and N. Hu. Changes Across Time in Spike Rate and Spike Amplitude of Auditory Nerve Fibers Stimulated by Electric Pulse Trains. *J. Assoc. Res. Otolaryngol.*, 8(3):356–372, 2007.